

CHARACTERIZATION OF NEAR-SURFACE TURBULENT BOUNDARY LAYER
FLOWS FOR WIND LOAD ANALYSIS AND OPTIMIZATION OF LARGE FRAME
STRUCTURES UNDER WIND ACTION

By

PEDRO LUIS FERNÁNDEZ CABÁN

A DISSERTATION PRESENTED TO THE GRADUATE SCHOOL
OF THE UNIVERSITY OF FLORIDA IN PARTIAL FULFILLMENT
OF THE REQUIREMENTS FOR THE DEGREE OF
DOCTOR OF PHILOSOPHY

UNIVERSITY OF FLORIDA

2017

© 2017 Pedro Luis Fernández Cabán

To my parents, Delia Iraida Cabán Dávila and Pedro Carlos Fernández Torres

ACKNOWLEDGMENTS

I am deeply grateful for the unconditional support and guidance of Dr. Forrest Masters, and for the trust that he had in me throughout the development of this work. His mentoring has proven indispensable in my growth as an academic researcher and, most importantly, as a person. I would like to recognize my committee members, Dr. Jennifer Rice, Dr. Gary Consolazio, and Dr. Raphael Haftka for their assistance and contribution to this dissertation. Dr. Luis Aponte and Ryan Catarelli also deserves my gratitude. Finally, I would like to thank and acknowledge the staff of the Powell Structures and Materials Laboratory for their passionate involvement and support in field measurements and wind tunnel testing.

TABLE OF CONTENTS

	<u>page</u>
ACKNOWLEDGMENTS.....	4
LIST OF TABLES.....	8
LIST OF FIGURES.....	10
ABSTRACT	14
CHAPTER	
1 INTRODUCTION	16
Objectives and Motivation.....	16
Organization	18
2 CHARACTERIZATION OF NEAR-SURFACE HURRICANE WINDS IN BUILT- UP TERRAIN.....	20
Background.....	20
Methodology	21
Field Experiments of Land Falling Tropical Cyclones.....	21
Data Processing.....	22
Conditional Analysis of the Reynolds Stress	24
Boundary Layer Wind Tunnel Measurements	26
Results.....	28
Higher Order Central Moments	28
Reynolds Stress Fractions.....	29
Relation of Stress Fraction Difference and Skewness.....	30
Discussion	31
Summary	33
3 WIND SIMULATION IN A LARGE BOUNDARY LAYER WIND TUNNEL.....	48
Background.....	48
Approach to Modeling.....	49
ESDU Model.....	49
Morphologic Models for Roughness Length Estimates	50
Methodology	51
Wind Tunnel	51
Roughness Element Grid and Vortex Generators	52
Flow Measurements	52
Experimental Design	53
Results and Discussion.....	53
Mean Velocity Profiles.....	53

	Turbulence intensity Profiles	54
	Summary	55
4	SURFACE PRESSURES ON LOW-RISE BUILDINGS	65
	Background.....	65
	Simulation of Approach Flow	67
	Low-Rise Building Models.....	68
	Pressure Measurements.....	68
	Instrumentation.....	68
	Pressure Coefficients	69
	Peak Pressures	70
	Experimental Design.....	71
	Results and Discussion.....	72
	Validation of Pressure Measurements.....	72
	Spatial Distribution of Surface Pressures	74
	Characterizing Upwind Terrain and Model Scale Comparison	76
	Summary	77
5	WIND LOAD DESIGN OPTIMIZATION OF STEEL FRAMES	96
	Background.....	96
	Discrete Optimization of Multi-Story Frame Structures	99
	Proposed ETE Algorithm	102
	Particle Swarm Optimization (PSO)	102
	ETE Algorithm	103
	Linearly Varying Control Parameter	104
	Discrete Stochastic (Exploitation) Scheme	105
	Results.....	106
	24 Story Three-Bay frame	106
	60 Story Seven-Bay Frame	108
	Summary	111
6	CONCLUSIONS AND FUTURE WORK	126
	Field Measurements of Hurricane Winds	126
	Surface Pressures on Low-Rise Buildings	126
	Design Optimization of Large Civil Structures Subject to Wind Loads.....	127
APPENDIX		
A	UWO PRESSURE TAP LAYOUT AND TESTING PARAMETERS	129
B	UFL WERFL MODELS	132
C	GEOMETRY OF WERFL MODELS (UFL).....	136
	LIST OF REFERENCES	145

BIOGRAPHICAL SKETCH..... 153

LIST OF TABLES

<u>Table</u>	<u>page</u>
2-1 FCMP datasets included in this study in addition to those analyzed in Balderrama et al. (2012).....	35
2-2 Total number of 15-min records ($z = 10$ m) stratified into mean wind speed and roughness length based on ASCE 7-10 exposure categories.	35
2-3 Mean roughness lengths stratified into mean wind speed and roughness length ($z = 10$ m) based on ASCE 7-10 exposure categories.....	35
2-4 Quadrants of events contributing to the total mean Reynold stress.....	36
2-5 Equivalent full-scale roughness lengths obtained from suburban terrain BLWT simulation.	36
2-6 Statistics of 15-min records stratified into mean wind speed and roughness length based on ASCE 7-10 exposure categories.	36
2-7 Mean stress fraction difference between sweep and ejection stratified into mean wind speed and roughness length.....	37
2-8 Proposed exposure coefficient values obtained from non-Gaussian peak factor model.....	37
3-1 BLWT aerodynamic parameters.....	56
4-1 WERFL testing parameters	78
5-1 Summary of statistics for optimum design of 24 story three-bay frame (100 Runs).....	112
5-2 Percent difference relative to best run for 24 story three-bay frame (100 Runs).....	112
5-3 Comparison of best designs for 24 story three-bay frame.	113
5-4 Location of structural members in the 60-story frame.....	114
5-5 Summary of statistics for optimum design of 60 story seven-bay frame (Independent Runs = 15).....	114
5-6 Percent difference relative to best run for 60 story seven-bay frame (Independent Runs = 15).....	114
5-7 Optimum design comparison for the 60 story planar frame.	115

C-1	WERFL model tap coordinates (1:20)	137
C-2	Vertices of WERFL building model (1:20).....	144

LIST OF FIGURES

<u>Figure</u>	<u>page</u>
2-1 Plan view of the BLWT at the University of Florida.....	38
2-2 Spatially averaged mean velocity profiles of six independent BLWT simulations measured at location $x = 29.5$ m	39
2-3 Longitudinal turbulence spectra of six independent BLWT simulations, measured at location $x = 29.5$ m	40
2-4 Observed mean (longitudinal) skewness values stratified into mean wind speed and terrain roughness.....	41
2-5 Observed mean (longitudinal) kurtosis values stratified into mean wind speed and terrain roughness.....	41
2-6 Mean Reynolds stress fractions for mean wind speed values stratified into mean wind speed and terrain roughness for the field observations.....	42
2-7 Spatially averaged Reynolds stress fractions of six independent BLWT simulations measured at location $x = 29.5$ m.	43
2-8 Theoretical and measured stress fraction difference between sweep and ejection quadrants	44
2-9 Measured stress fraction difference versus longitudinal skewness	45
2-10 Measured stress fraction difference versus vertical skewness	46
2-11 Proposed non-Gaussian exposure coefficient versus elevation above ground. .	47
3-1 Boundary layer wind tunnel at the University of Florida.....	57
3-2 Set of screens and honeycomb system downwind of the fan bank	57
3-3 Pitot tube mounted to the wall of the tunnel.....	58
3-4 Freestream reference anemometry	58
3-5 Meteorological weather station located adjacent to the exit of the BLWT.....	59
3-6 Irwin spires located downwind of the screens and honeycomb	59
3-7 Longitudinal mean velocity profiles for a narrow edge windward element orientation.....	60

3-8	Longitudinal Mean velocity profiles for a wide edge windward element orientation.....	60
3-9	Semi-logarithmic mean velocity profiles for the narrow edge windward element orientation.	61
3-10	Semi-logarithmic mean velocity profiles for the wide edge windward element orientation.....	61
3-11	Longitudinal turbulence intensity profiles for a narrow edge windward element orientation.	62
3-12	Longitudinal turbulence intensity profiles for a wide edge windward element orientation.....	62
3-13	Lateral turbulence intensity profiles for a narrow edge windward element orientation.....	63
3-14	Lateral turbulence intensity profiles for a wide edge windward element orientation.....	63
3-15	Vertical turbulence intensity profiles for a narrow edge windward element orientation.....	64
3-16	Vertical turbulence intensity profiles for a wide edge windward element orientation.....	64
4-1	Pressure tap layout for 1:20, 1:30, and 1:50 WERFL building models.	79
4-2	Measured and fitted response amplitudes up to a frequency of 600 Hz.	80
4-3	Schematic diagram of BLWT physical arrangement near the test section for pressure tests.	80
4-4	Aerodynamic test of 1:30 WERFL building model at UF's BLWT.	81
4-5	Comparison of mean pressure coefficients for Narrow edge, $h = 150$ mm, and $\alpha = 90^\circ$	82
4-6	Comparison of peak pressure coefficients for Wide edge, $h = 80$ mm, and $\alpha = 90^\circ$	83
4-7	Pressure spectra comparison of Tap 216 for the 1:20 WERFL model.....	84
4-8	Distribution of mean pressure coefficients for the 1:20 WERFL model for Wide edge and $\alpha = 0^\circ$	85
4-9	Distribution of RMS pressure coefficients for the 1:50 WERFL model for Wide edge and $\alpha = 90^\circ$	86

4-10	Distribution of peak pressure coefficients for the 1:30 WERFL model for Wide edge and $\alpha = 45^\circ$	87
4-11	Distribution of mean pressures along a line of taps parallel to the long building dimension for the 1:20 WERFL model (Wide edge, $\alpha = 0^\circ$).....	88
4-12	Distribution of mean pressures along a line of taps parallel to the long building dimension for the 1:30 WERFL model (Wide edge, $\alpha = 0^\circ$).....	88
4-13	Distribution of mean pressures along a line of taps parallel to the long building dimension for the 1:50 WERFL model (Wide edge, $\alpha = 0^\circ$).....	89
4-14	Distribution of mean pressures along a line of taps perpendicular to the long building dimension for the 1:20 WERFL model (Wide edge, $\alpha = 90^\circ$).....	89
4-15	Distribution of mean pressures along a line of taps perpendicular to the long building dimension for the 1:30 WERFL model (Wide edge, $\alpha = 90^\circ$).....	90
4-16	Distribution of mean pressures along a line of taps perpendicular to the long building dimension for the 1:50 WERFL model (Wide edge, $\alpha = 90^\circ$).....	90
4-17	Distribution of peak pressures along a line of taps parallel to the long building dimension for the 1:20 WERFL model (Wide edge, $\alpha = 0^\circ$).....	91
4-18	Distribution of peak pressures along a line of taps parallel to the long building dimension for the 1:30 WERFL model (Wide edge, $\alpha = 0^\circ$).....	91
4-19	Distribution of peak pressures along a line of taps parallel to the long building dimension for the 1:50 WERFL model (Wide edge, $\alpha = 0^\circ$).....	92
4-20	Peak pressures on all 266 taps for open country terrain simulation	93
4-21	Peak pressures on all 266 taps for suburban terrain simulation.	94
4-22	Peak pressures on all 266 taps for open country terrain simulation with narrow and wide edge windward element orientation.....	95
5-1	Linear variation of θk during the optimization process.....	116
5-2	Conditional subroutine for determining d_i	116
5-3	Flowchart of ETE for discrete sizing design optimization of framed structures.	117
5-4	Topology and loading condition for the 24 story three-bay planar frame.....	118
5-5	ETE mean optimization history for the 24 story three-bay frame.....	119
5-6	Member sizing, inter-story drift, and load-capacity ratios for the 24 story three-bay frame obtained using ETE for Case 1.....	120

5-7	Member sizing, inter-story drift, and load-capacity ratios for the 24 story three-bay frame obtained using ETE for Case 3.....	121
5-8	Topology and loading condition for the 60 story seven-bay planar frame.....	122
5-9	ETE mean optimization history for the 60-story seven-bay frame	123
5-10	Member sizing, inter-story drift, and load-capacity ratios for the 60 story seven-bay frame obtained using ETE for Case 2	124
5-11	Member sizing, inter-story drift, and load-capacity ratios for the 60 story seven-bay frame obtained using ETE for Case 3	125
A-1	UWO pressure tap layout for 1:100 WERFL model.	130
A-2	UWO test parameters for 1:100 WERFL model.....	131
B-1	1:20 UFL-WERFL model for Narrow edge, $h = 20$ mm, and $\alpha = 0^\circ$	133
B-2	1:20 UFL-WERFL model for Narrow edge, $h = 80$ mm, and $\alpha = 45^\circ$	133
B-3	1:20 UFL-WERFL model for Narrow edge, $h = 160$ mm, and $\alpha = 90^\circ$	134
B-4	1:20 UFL-WERFL model for Wide edge, $h = 80$ mm, and $\alpha = 0^\circ$	134
B-5	1:20 UFL-WERFL model for Wide edge, $h = 20$ mm, and $\alpha = 45^\circ$	135
B-6	1:20 UFL-WERFL model for Wide edge, $h = 160$ mm, and $\alpha = 90^\circ$	135

Abstract of Dissertation Presented to the Graduate School
of the University of Florida in Partial Fulfillment of the
Requirements for the Degree of Doctor of Philosophy

CHARACTERIZATION OF NEAR-SURFACE TURBULENT BOUNDARY LAYER
FLOWS FOR WIND LOAD ANALYSIS AND OPTIMIZATION OF LARGE FRAME
STRUCTURES UNDER WIND ACTION

By

Pedro Luis Fernández Cabán

August 2017

Chair: Forrest J. Masters
Major: Civil Engineering

This dissertation presents three interrelated studies of importance to the quantification of boundary layer wind loads on civil infrastructure.

The first study refutes the longstanding assumption that near surface wind velocity exhibits Gaussian behavior irrespective of the aerodynamic roughness length of the upwind fetch. Analysis of a large database comprising ground-level anemometric observations during land falling hurricanes, and a series of boundary layer wind tunnel (BLWT) experiments suggest that the longitudinal component of the wind velocity positively skews in more built-up terrain conditions during strong wind events. Quadrant analysis of the Reynolds stress revealed the strong linkage between non-Gaussian observations and sweep events—high-velocity air masses moving towards the surface. The study demonstrates and discusses possible implications of observed non-Gaussian trends on peak loads on buildings.

The second study leverages a comprehensive series of experiments in a large boundary layer wind tunnel to investigate the variation of external pressure coefficients with increasing surface roughness on low-rise buildings. BLWT modeling was carried

out on three rigid building models of the Wind Engineering Research Field Laboratory (WERFL) experimental building with geometric scales of 1:20, 1:30, and 1:50. A total of 33 upwind terrain configurations were explored for each model scale. BLWT pressure tests were also compared to aerodynamic experiments of a 1:100 model of the WERFL building conducted at University of Western Ontario (UWO). The findings revealed the dependency of extreme pressure coefficients with increasing surface roughness. Peak pressures near the leading edge of the roof appeared to vary linearly with increasing turbulence levels at eave height. Only slight variations in the mean pressures were observed with increasing turbulence levels.

The third study addresses the optimization of large frame structures subjected to wind action. It presents a new metaheuristic technique to minimize the weight of the structure while satisfying strength and serviceability requirements. The algorithm transitions from the global examination of the design domain, to the restricted investigation around promising regions (subdomains). The latter is performed through a discrete stochastic search scheme, which conducts an exhaustive search near the global optimum during late stages of the optimization process (exploitation).

CHAPTER 1 INTRODUCTION

Despite recent advancements in computational wind engineering in the past few decades (e.g., Blocken, 2014; Troldborg et al., 2014), accurately modeling peak wind loads on civil structures through purely numerical techniques remains elusive. Therefore, physical measurements are obtained in boundary layer wind tunnel (BLWT). The research herein seeks to advance our understanding of turbulent wind loading and the associated structural response. It addresses basic assumptions about simulated approach flow conditions in the BLWT, including the experimental limitations imposed by model scale, and presents a new method to optimization large frame structures under wind action.

Objectives and Motivation

The purpose of this dissertation was three fold. The first objective was to evaluate how the near surface (<20 m) wind field evolves as the aerodynamic roughness increases. Analysis of field and BLWT three-dimensional velocity records found that the surface wind field trends to non-Gaussian behavior as the upwind terrain becomes more built up. The cause is attributed to the linkage between the longitudinal skewness and downward transfers of momentum (sweep events) in strong winds. The implication is significant for commissioning of wind tunnel experiments. Current standards omit any reference to this phenomenon.

The second objective was to examine how the magnitude and spatial distribution of aerodynamic loads on low-rise buildings change with terrain, angle of attack, and model-scale. Pressure coefficients on models of the Texas Tech University Wind Engineering Research Field Laboratory (WERFL) experimental building with geometric

scales of 1:20, 1:30, and 1:50 were immersed in a wide range of turbulent boundary layer flows using precise adjustment of a computer control terrain generator called the Terraformer. The series of experiments will serve as a testbed for exploring more complex upwind terrains, such as heterogeneous roughness element fields, to simulate more realistic topographic conditions and the adverse wind-induced effects on low-rise buildings. A large database will be stored on the Natural Hazards Engineering Research Infrastructure (NHERI) Cyberinfrastructure node at the University of Texas at Austin, which can be accessed by researchers worldwide.

The third objective was to create a structural design framework suitable for sizing optimization of large-scale civil structures subject to wind loads. A hybrid metaheuristic search algorithm was developed for cost optimization of steel frames subject to code-based strength and serviceability requirements. This work adds to the knowledge base for the automation of the structural design process of civil structures, which is expected to grow significantly in the coming decades. Efforts for the development of frameworks, such as Performance Based Design (PBD), for the analysis and design of buildings subject to wind loads are ongoing (e.g., Spence and Giofrè, 2012; Spence and Kareem, 2013). This PBD philosophy has been successfully applied in the field of seismic engineering. The wind engineering community is progressively adapting PBD strategies to obtain optimum and cost-effective solutions in the design of civil structures exposed to extreme wind events. However, direct transfer of the PBD concepts from seismic to wind is not conceivable due to the complex mechanism such as with complex dimensional turbulence and vortex shedding on a structure. Although there has been significant progress in the computational modelling of these multifaceted wind

phenomena—the use computational fluid dynamics (CFD) and large eddy simulation (LES)—their practical application to design optimization problems of civil structures is not well yet established. Consequently, researchers have relied on large databases of detailed aerodynamic and climatologic information from boundary layer wind tunnel (BLWT) tests and full-scale field measurements in the design optimization of buildings (Spence and Kareem, 2013).

Organization

The current dissertation is organized into six chapters that present three manuscripts out of which one is accepted and the other two will soon be submitted to peer-reviewed journals.

Chapter 2 discusses results from a large database of field experiments to examine non-Gaussian wind behavior in suburban terrains, and probable implications to peak loads on low-rise structures. This chapter was recently accepted by the Journal of Wind Engineering and Industrial Aerodynamics.

Chapters 3 and 4 will later be combined to produce a single journal article, and will be submitted to the Journal of Wind Engineering and Industrial Aerodynamics. Chapter 3 describes the components of a large boundary layer wind tunnel (BLWT) located at the University of Florida. The chapter discusses methods applied for the validation of an automated terrain generator (i.e., the Terraformer). Chapter 4 outlines findings from a comprehensive series of aerodynamic tests on low-rise structures in the BLWT to examine the effects of small perturbations in upwind terrain conditions on peak loads.

Chapter 5 presents a hybrid metaheuristic search algorithm for discrete sizing optimization of large steel frames subject to wind loads. This chapter will be submitted to the Journal of Computers and Structures.

Chapter 6 (Conclusions and Future Work) summarizes general findings, limitations, and recommendations resulting from this dissertation.

CHAPTER 2 CHARACTERIZATION OF NEAR-SURFACE HURRICANE WINDS IN BUILT-UP TERRAIN

This chapter presents analysis of anemometric observations collected during the 1999-2016 Atlantic hurricane seasons and boundary layer wind tunnel (BLWT) measurements indicate that the near surface wind behavior deviates from Gaussian as surface roughness increases. Quadrant analysis of the Reynolds stress clearly demonstrates the linkage between the longitudinal skewness and downward transfers of momentum (sweep events) in strong winds, which previous studies have also observed. Modern wind load provisioning and BLWT similarity requirements do not explicitly account for this effect, although the experimental configuration of typical wind tunnel development sections may correctly simulate the phenomena. Here we quantify how the observed positive skewness affects the terrain exposure coefficient profile for ASCE 7. The results demonstrate the need to update peak factor calculations to accurately predict extreme winds acting on low-rise buildings in built-up terrain.

Background

The dominant assumption in wind engineering is that the surface (< 25 m) wind field exhibits Gaussian behavior over all terrain types. Results from 17 years of anemometric observations in tropical cyclones and recent boundary layer wind tunnel (BLWT) experiments indicate that the skewness (γ_{3u}) of the longitudinal velocity component increases with aerodynamic roughness length (z_0)—a phenomena not currently addressed by exposure conversion factors in wind load provisioning nor in standards to commission facilities for BLWT modeling, e.g. ASCE/SEI 49-12 and AWES-QAM-1-2001. The cause is attributed to the prevalence of sweeps, i.e. downward and forward departures from the mean longitudinal flow, which positively

skew the velocity. This mechanism, in part, also explains why field studies (e.g., Baldocchi and Hutchison 1987; Baldocchi and Meyers, 1988; Maitani and Shaw, 1990) have observed variations in high order moments near the canopy of suburban regions. Our observations strongly corroborate with previous findings originating from field measurements (e.g., Chen, 1990; Rotach, 1995; Rotach et al., 2005; Shaw et al., 1983) and the BLWT (e.g., Finnigan, 2000; Zhu et al., 2007; Raupach, 1981; Böhm et al., 2013), which have documented the dominance of large coherent structures within and just above the canopy of the turbulent boundary layer, and the correlation of these structures to the third moment of the longitudinal and vertical velocity components.

The chapter extends the work of Balderrama et al. (2012), expanding its dataset to include targeted field measurements in suburban terrain and ultrasonic anemometer measurements at five levels spanning 5 to 15 m. It also incorporates new approach flow data collected in a novel BLWT that can rapidly reconfigure the roughness element grid to achieve a user-specified z_0 for a user-specified geometric scale. The results suggest the standards should be conservatively updated to incorporate a linear change in γ_3 from [0.46, 0.0] over [4.4, 24.6] m, holding $\gamma_3 = 0.46$ below this extent. Applying the non-Gaussian up-crossing rate defined in Kareem and Zhou (1994) to the wind speed (pressure) conversion described in Masters et. al. (2010), we find up to a 14% increase in the pressure loading on suburban low-rise structures (ASCE 7-10, 2010).

Methodology

Field Experiments of Land Falling Tropical Cyclones

The study's field data originate from near-surface wind field observations collected during 1999-2016 Atlantic tropical cyclones by the Florida Coastal Monitoring Program (FCMP), a multi-institution consortium that includes the University of Florida,

Clemson University, Florida International University, and the Insurance Institute for Business & Home Safety. Balderrama et al. (2011, 2012) describe the program in detail.

The dataset includes records from 86 deployments of portable weather stations in 25 named storms. The current study incorporates 13 new field experiments that deployed upgraded 15 m portable weather stations (Table 2-1), with suburban terrain being the primary study target. The original 10 m FCMP weather stations are equipped with anemometers at 5, and 10 m. Two custom arrays of three fixed axis anemometers (RM Young Model Number 27106R) collect wind velocity observations (3D wind speed and direction) at the 5 and 10 m levels. Dynamic characteristics of the anemometer's four-blade polypropylene helicoid propellers (Model Number 08234) include a 2.7 m, 63% recovery distance constant and a damped natural wavelength of 7.4 m. A wind monitor (RM Young Model Number 05103V) installed at the 10 m level serves as a redundant anemometer system to monitor the horizontal component of the wind. The wind monitor 50% recovery vane delay distance is 1.3 m and it is rated for a 100 m/s gust survival. In 2010, two weather stations were upgraded with high-resolution ultrasonic anemometers (WindMaster Pro Model 1561-PK-020) installed at 5, 7.5, 10, 12.5, and 15 m above ground level. The units have a wind speed range of 0-65 m/s with a resolution of 0.01 m/s, and measure instantaneous u , v , and w wind components with a maximum sampling rate of 32 Hz. In this study, data were sampled at or resampled to 10 Hz.

Data Processing

Data were segmented into continuous non-overlapping 15-min time histories. Quality control included comparing the propeller measurements at an elevation of 10 m to the redundant wind monitor measurements at the same elevation to detect

anomalies. Data segments with mean wind velocities below 5 m/s were removed to eliminate any effects from convection. The tower tilt correction described in Foken and Nappo (2008) was performed to align the anemometer coordinate system into the streamlines and towards the mean flow coordinate system. Negligible mean vertical and lateral wind components were verified to satisfy the requirements of an eddy-covariance method of analysis. Linear trend removal methods were performed on all 15-min records to remove first order non-stationarities.

Shear (friction) velocities for each data segment were calculated directly from the three measured orthogonal velocity components following Weber (1999):

$$u_* = \left(\overline{u'w'^2} + \overline{v'w'^2} \right)^{\frac{1}{4}} \quad (2-1)$$

The logarithmic mean velocity profile was then used to estimate the roughness length z_0 :

$$z_0 = (z - d) \exp \left[-\frac{U(z)\kappa}{u_*} \right] \quad (2-2)$$

where $U(z)$ is the mean wind speed at elevation z , $\kappa = 0.4$ is von Karman's constant., and d is the zero-plane displacement height. Measurements were obtained at 2-5 levels, preventing direct estimation of d . Thus the heuristic method of Jackson (1981) was applied:

$$d = \overline{H} - 2.5z_0 \quad (2-3)$$

where \bar{H} is the average roughness element height, nominally assumed to be 5 m, which is representative of locations surrounded by clusters of single family dwellings.

Displacement height was assumed to be effectively zero for records with $z_0 < 0.15$ m.

For quality assurance, an independent procedure was performed to calculate z_0 . A bounded nonlinear function minimization was applied to satisfy the logarithmic formulation of the mean velocity profile and the modified Harris and Deaves (1980) variance model described in Vickery and Skerjil (2005). Percent differences between the two procedures were in the range of 2-6% for records corresponding to suburban terrain ($0.15 \text{ m} > z_0 \geq 0.7 \text{ m}$).

Data records were stratified by surface roughness (exposure) categories defined in ASCE 7-10 (2010), i.e. B (suburban), C (open), and D (marine). Table 2-2 lists the number of 15-min records stratified by surface roughness and the mean wind speed at 10 m. Table 2-3 lists the corresponding mean roughness length estimates, which were obtained from Equation 2-2 for $U(z = 10 \text{ m})$.

Conditional Analysis of the Reynolds Stress

Conditional (also known as quadrant) analysis of the Reynolds stress is useful to quantify the turbulent mechanisms of organized structures in the inertial sublayer and the roughness sublayer (RS), i.e. the region below the inertial sublayer affected by the coherent motions spawned by buildings, trees, etc. upwind (Lu et al., 1973). It applies conditional statistical averaging to partition the contribution of the mean Reynolds stress into four quadrants based on the sign of the (mean-removed) longitudinal (u') and vertical (w') wind velocity components as shown in Table 2-4. Sweep and ejection events (quadrants two and four) make positive contributions to the Reynolds stress, with

the former associated with downward motion and forward velocity greater than the mean. Quadrants one and three correspond to inward and outward interaction events and contribute negatively to the shear stress.

The contribution of the total Reynolds stress from quadrant i is

$$\langle u'w' \rangle_{i,H} = \lim_{T \rightarrow \infty} \frac{1}{T} \int_0^T u'(t)w'(t)I_{i,H}[u'(t), w'(t)] dt \quad (2-4)$$

where T is the averaging time and $I_{i,H}$ is the indicator function. $I_{i,H}$ takes a value of one if $|u'w'| \geq H|\overline{u'w'}|$, otherwise, $I_{i,H} = 0$. Increasing the hyperbolic “hole size” H allows examination of large-scale and sparse structures (i.e., coherent motions) by eliminating small and frequent contributions. The fraction of the shear stress transported is obtained from normalizing Equation 2-4 by the mean Reynolds stress $\overline{u'w'}$.

$$S_{i,H} = \frac{\langle u'w' \rangle_{i,H}}{\overline{u'w'}} \quad (2-5)$$

The difference in stress fraction between quadrants two and four

$$\Delta S_H = S_{4,H} - S_{2,H} \quad (2-6)$$

expresses the imbalance of sweep and ejection events (> 0 = sweep dominance).

Raupach (1981) established a relation between $\Delta S_{H=0}$ and the third moments (skewness) of the fluctuations in the velocity components u' and w' , which can be derived by a cumulant-discard method (Antonia and Atkinson, 1973; Nakagawa and Nezu, 1977). For $H = 0$, the theoretical difference in all stress contributions in the sweep and ejection quadrants ΔS_0 ($\Delta S_0 = S_{4,0} - S_{2,0}$) can be expressed as

$$\Delta S_0 = \frac{1 + \rho}{\rho\sqrt{2\pi}} \left[\frac{2C_1}{(1 + \rho)^2} + \frac{C_2}{1 + \rho} \right] \quad (2-7)$$

where,

$$C_1 = (1 + \rho) \left[\frac{1}{6}(M_{03} - M_{30}) + \frac{1}{2}(M_{21} - M_{12}) \right] \quad (2-8)$$

$$C_2 = - \left[\frac{1}{6}(2 - \rho)(M_{03} - M_{30}) + \frac{1}{2}(M_{21} - M_{12}) \right] \quad (2-9)$$

In Equations 2-8 and 2-9, $\rho = \overline{u'w'}/\sigma_u\sigma_w$ is the correlation coefficient and M represent the third moments ($M_{03} = \overline{w'w'w'}$, $M_{30} = \overline{u'u'u'}$, $M_{12} = \overline{u'w'w'}$, $M_{21} = \overline{u'u'w'}$).

Boundary Layer Wind Tunnel Measurements

FCMP field observations were compared against flow measurements in the University of Florida's BLWT, which is a low-speed open circuit tunnel with dimensions of 6 m W x 3 m H x 38 m L. Comparison of field and wind tunnel observations was conducted during a validation study of the Terraformer, which is an automated roughness element grid that rapidly reconfigures the height and orientation of 1116 roughness elements in a 62 X 18 grid to achieve desired upwind terrain conditions. The grid extends nominally 18.3 m along the length of the tunnel (Figure 2-1). Dimensions of the elements are 5 cm by 10 cm, and they are spaced 30 cm apart in a staggered pattern. Height and orientation can be varied from 0-160 mm and 0-360 degrees, respectively. Two orientations were applied. The narrow and wide edge cases refer to the 5 cm and 10 cm face perpendicular to the flow, respectively.

Spatially averaged semi-logarithmic mean velocity profiles are shown in Figures 2-2. The profiles were measured over the last row of the roughness elements closest to the test section, at location $x = 29.5$ m (Figure 2-1), using an automated gantry system

instrumented with four Turbulent Flow Instrumentation Cobra pressure probes that measure u , v , and w velocity components and static pressure within a $\pm 45^\circ$ acceptance cone. Response characteristics include a maximum frequency response of 2 kHz and a 2-100 m/s sensing range. Three vertical traverses were taken across the width of the tunnel—at the centerline and ± 500 mm off the centerline of the tunnel. Aerodynamic parameters z_0 and u_* values (Table 2-5) were estimated from a non-linear least squares fit of the log law to the mean velocity profile in the inertial-sublayer (ISL) region ($z \sim 150$ -900 mm), following the curve-fitting method in Karimpour et al. (2012). Zero-plane displacement height estimates were based on the geometric arrangement of the roughness array following MacDonald et al. (1998):

$$\frac{d}{h} = 1 + A^{-\lambda}(\lambda - 1) \quad (2-10)$$

where λ is the plan area index defined as the ratio of the lot area to the plan area of the roughness element, and A is a constant taken as 4.43—the recommended value for a staggered array. The reference mean wind velocity U_{ref} was measured at a height $z_{ref} = 1.48$ m.

Plots of BLWT longitudinal turbulence spectra at a height $z = 610$ mm are shown in Figure 2-3 for the six corresponding mean velocity profiles. Measured data were compared with the power spectra model in ESDU 74030 and 74031 (1974), which was first derived by von Kármán (1948) for isotropic turbulence:

$$nS_{uu}(z, n)/\sigma_u^2 = 4f/(1 + 70.8f^2)^{\frac{5}{6}} \quad (2-11)$$

where $f = nL_u^x/U$. $S_{uu}(z, n)$ is the power spectral density function, n is the frequency, U is the longitudinal mean velocity, and L_u^x is the longitudinal integral length scale of the turbulence. Measured spectra were calculated following Welch's method in Bendat and Piersol (2000). Time histories were segmented into eight contiguous blocks, and a Hanning tapering window with 50% overlap was applied to suppress side-lobe leakage. These plots are representative of measurements obtained between 320-860 mm, outside of the immediate influence of the individual roughness elements. In all cases in this range, similitude was achieved.

Results

Higher Order Central Moments

Figures 2-4 and 2-5 show semi-logarithmic whisker subplots of the mean longitudinal skewness (γ_{3u}) and kurtosis (γ_{4u}) at elevations of 5 m and 10 m for three mean wind speed ranges for data collected in the field. The whiskers bound the 25th and 75th quantiles, and the letters B, C and D inside the whisker box indicate the exposure category. An increase in skewness with terrain roughness is evident for all wind speed ranges. Skewness values at 5 m are consistently larger than 10 m values for the three exposures. Records with mean wind speeds above 25 m/s in exposure B (suburban) show mean skewness values of 0.49 and 0.37 for elevations of 5 m and 10 m, respectively. Table 2-6 summarizes the statistics of all 5 m and 10 m 15-min records based on exposure category and mean wind speed. The table shows that for a given terrain exposure, the mean γ_{3u} may be assumed to be invariant to mean wind speed. No significant change in kurtosis was observed.

Reynolds Stress Fractions

In Figure 2-6, the average Reynolds stress fractions $|S_{i,H}|$ are shown as a function of H for and exposure categories. Observations at 10 m (top three subplots) display a slight decrease in ejection contributions with increasing roughness. At $H = 0$, ejection contributions in higher winds ($U \geq 25$ m/s) account for ~60, ~70, and ~82% of the total mean stress for exposures B, C, and D, respectively. Sweep events appear to contribute equally for the three exposure categories at $z = 10$ m. The 10 m subplots in Figure 2-6 also suggest a minor reduction in the contribution of inward/outward interaction events in more built-up terrain. At 5 m, a significant increase in sweep contributions is observed for exposure B (suburban) in high winds ($U \geq 25$ m/s), comprising over 95% of the total mean stress for $H = 0$. Sweep contributions are still present for larger hole sizes. At $H = 20$, mean $|S_{i,H}|$ associated with sweeps account for ~18% ($U \geq 25$ m/s), while ejection events appear to vanish for $H \geq 18$. The two interaction events at 5 m display greater contributions to the Reynolds stress in rougher terrain for $U \geq 25$ m/s (bottom right subplot).

Subplots of spatially averaged Reynolds stress fractions from BLWT simulation are shown in Figure 2-7. Two elevations (above the tunnel floor) z where normalized by the six roughness length estimates presented in Table 2-5. Large sweep contributions (greater than 90%) for $H = 0$ can be observed for element heights of 40, 60 and 100 mm, all oriented with the narrow edge perpendicular to the flow. For $h = 60$ mm, a height of $z = 5$ m will result in a roughness length of 0.36 m ($z/z_0 = 14$), which would classify as Exposure B in ASCE 7-10. Additionally, sweep contributions are still present up to $H = 20$ for these three element configurations. For $h = 80$ mm, sweep

contributions account for 80% of the Reynolds stress at $H = 0$. However, ejections at $H = 0$ are approximately 60%, which results in sweep dominance. Subplots for the two wide edge element orientations (top two subplots) show sweep contributions around 80% for $H = 0$. However, capturing the coherent structures in the roughness sublayer is more challenging as the element height approaches zero (i.e., flush tunnel floor)—i.e., the thickness of the “wake region” is zero for $h = 0$ mm.

Relation of Stress Fraction Difference and Skewness

Figure 2-8 plots the theoretical stress fraction difference ΔS_0 obtained from Equation 2-7 against the measured ΔS_0 values—i.e., Equation 2-6—for three wind speed ranges. Observations at both 5 m and 10 m heights show good agreement of measured ΔS_0 with values found from Equation 2-7. The bulk of records associated with exposure B (suburban) favor positive values of ΔS_0 , hence suggesting sweep dominance.

Figure 2-9 plots the longitudinal skewness values (γ_{3u}) against ΔS_0 values. The six scatter plots exhibit a positive linear trend between ΔS_0 and γ_{3u} . Proportionality coefficients obtained from linear regression analysis are included in the subplots. Slightly higher linear coefficient values are found at 5 m heights for all three wind speed regimes. This suggests greater sweep dominance at 5 m than over 10 m heights. Linear coefficient values for records with $U \leq 25$ m/s closely match proportionality values of γ_{3u} and ΔS_0 established in Raupach (1981). However, the coefficient decreases for $U \geq 25$ m/s, with values of 0.33 and 0.27 for 5 m and 10 m observations, respectively.

Scatter plots in Figure 2-10 show the relation of the vertical skewness (γ_{3w}) and ΔS_0 . An approximate negative linear relation between γ_{3w} and ΔS_0 is observed. Oikawa

and Meng (1995) detected similar trends from field observations at heights above the ground near the suburban canopy region. In addition, vertical skewness values in Figure 2-10 compare well with calculated γ_{3w} values from Raupach et al. (1996), which ranged from -0.5 to -1.0 within a vegetated canopy layer. A robust multilinear regression was performed to the scattered data using an iteratively re-weighted least squares method with a bi-square weighting function. The linear coefficients are included in the subplots. No prior work was found for comparison of regression analysis coefficient for γ_{3w} . Nevertheless, it can be deduced from Figure 2-9 that sweep events in suburban regions are predominantly associated with negatively skewed distributions of the vertical wind component in strong winds.

Table 2-7 summarizes results presented in this section, which reveal the increasing trend of sweep dominance in rougher upwind terrain. Measured ΔS_0 values exceed 20% for the three wind speed ranges in Exposure B at $z = 5$ m. However, Exposures C and D show mean stress fraction differences in the range of 2%-12% for the same measurement height. Furthermore, negative ΔS_0 values—i.e., ejection dominance—are observed for two wind speed ranges collected at 10 m in Exposure D.

Discussion

Effects of observed non-Gaussian trends within the roughness sublayer on suburban exposure coefficient values (K_z values in ASCE 7-10) are now examined. Figure 2-11 includes the proposed non-Gaussian exposure coefficient K_{zNG} profile for suburban exposure based on linearly varying γ_{3u} values with height above ground level—i.e., the skewness profile. The proposed non-Gaussian exposure coefficient is calculated from

$$K_{zNG} = \left(\frac{U_{gNG}(z)}{U_{g,ref}} \right)^2 \quad (2-12)$$

in which $U_{g,ref}$ is the 3 s gust velocity at 10 m in open terrain ($z_0 = 0.02$ m), $U_{gNG}(z)$ is the gust velocity profiles obtained from

$$U_{gNG}(z) = U(z)[1 + g_{NG}I_u] \quad (2-13)$$

where $U(z)$ is the mean velocity profile (Equation 2-2). The shear velocity in Equation 2-2 is determined for a given gradient wind speed U_g based on the relation between u_* and U_g described in Irwin (2006). The turbulent intensity I_u is computed from Harris and Deaves (1980) variance model.

Balderrama et al. (2012) demonstrated that the non-Gaussian peak factor model in Kareem and Zhao (1994, henceforth KZ94) is more accurate than the Gaussian model defined in Davenport (1964, henceforth D64). The non-Gaussian peak factor g_{NG} from KZ94 can be expressed as

$$g_{NG} = \alpha \left\{ \begin{array}{l} \left(\beta + \frac{\gamma}{\beta} \right) + h_3(\beta^2 + 2\gamma - 1) + \dots \\ h_4 \left[\beta^3 + 3\beta(\gamma - 1) + \frac{3}{\beta} \left(\frac{\pi^2}{12} - \gamma + \frac{\gamma^2}{2} \right) \right] \end{array} \right\} \quad (2-14)$$

where γ is Euler's constant, 0.5772, $\beta = \sqrt{2 \ln(\nu T)}$, ν is the crossing rate, and T is the duration of the record. The parameters α , h_3 , and h_4 are dependent on the third (skewness) and fourth (kurtosis) moments (KZ94). In the special case where $\gamma_{3u} = 0$ and $\gamma_{4u} = 3$, Equation 2-14 takes the form of the Gaussian D64 peak factor model. A constant kurtosis value of $\gamma_{4u} = 3.0$ was selected in Equation 2-14 to generate K_{zNG} values. A value of $z_0 = 0.15$ m was chosen for the proposed K_{zNG} profile. This

roughness length corresponds to the lower limit value specified in ASCE 7-10 (2010) for suburban terrain.

The (linear) skewness profile shown in Figure 2-11 (left subplot) was constructed from mean γ_{3u} values of FCMP observations at 5 m, 7.5 m, 10 m, 12.5 m, and 15 m for suburban exposure ($z_0 = 0.15$ m-0.7 m). Full-scale γ_{3u} values in Figure 2-10 are limited to 15 min records collected from 2012-2016 using ultrasonic (US) anemometry—Table 2-1. Only records satisfying $U \geq 10$ m/s were considered. Horizontal whiskers at the three FCMP elevations indicate the 25th and 75th quantiles. Below $z = 4.6$ m, skewness values are kept constant ($\gamma_{3u} = 0.46$).

BLWT skewness profiles from the six independent tests summarized in Table 2-5 are also shown in Figure 2-11 (left subplot). Most of the BLWT data show skewness values in the range of 0.20-0.5 up to 5 m full-scale elevation. Above 5 m, the BLWT data exhibit a noticeable decreasing trend towards zero skewness. Table 2-8 summarizes proposed skewness values and non-Gaussian K_{zNG} values for heights up to 24.4 m. The table shows a ~14% increase in suburban exposure coefficient values at $z = 10$ m from K_z values provided in ASCE 7-10 (2010).

Summary

Analysis of anemometric observations collected during 1999-2016 Atlantic hurricane seasons, along with BLWT data, exhibit non-Gaussian wind behavior in suburban terrain exposures within the suburban roughness sublayer. Observations in suburban terrain predominantly show positively skewed distributions of the along-wind component, thus increasing the probability of peak gust events. In addition, field data suggests a dependence of longitudinal skewness with height in rougher terrain. Positive

skewness values appear to increase with decreasing elevation near the suburban canopy. BLWT studies for suburban terrain also seem to follow similar tendencies. Quadrant analysis reveals the linkage between positive values of the longitudinal skewness and downward transfers of momentum (sweep events). Most of these records are associated to rougher terrain conditions (suburban). However, sweep dominance appears to be less pronounced in higher winds. Positively skewed distributions measured within the roughness sublayer were incorporated into exposure coefficient calculations for suburban terrain through a non-Gaussian peak factor model. A non-trivial increase in suburban exposure coefficient values was found.

Table 2-1. FCMP datasets included in this study in addition to those analyzed in Balderrama et al. (2012).

Year	Tropical Cyclone	Station ID	Latitude	Longitude	Town	Anemometry
2016	Matthew	T1	+28.1947	-80.5944	Satellite Beach, FL	3-Axis Propeller
2016	Matthew	T2	+32.7141	-79.9664	Charleston, SC	Ultrasonic
2016	Matthew	T2	+27.1889	-80.2411	Stuart, FL	Ultrasonic
2016	Matthew	T3	+32.7902	-79.9881	Charleston, SC	Ultrasonic
2016	Matthew	T3	+28.1937	-89.6056	Satellite Beach, FL	Ultrasonic
2016	Matthew	T5	+27.1802	-80.2295	Stuart, FL	3-Axis Propeller
2016	Hermine	T2	+29.6735	-83.3746	Steinhatchee, FL	Ultrasonic
2016	Hermine	T3	+29.6731	-83.3798	Steinhatchee, FL	Ultrasonic
2016	Hermine	T5	+29.6728	-83.3703	Steinhatchee, FL	3-Axis Propeller
2014	Arthur	T2	+35.2322	-75.6215	Hatteras, NC	Ultrasonic
2012	Sandy	T3	+39.3208	-74.5953	Linwood, NJ	Ultrasonic
2012	Isaac	T3	+29.6487	-90.6940	Houma, LA	Ultrasonic
2012	Isaac	T2	+29.5385	-89.7751	Bohemia, LA	Ultrasonic

Table 2-2. Total number of 15-min records ($z = 10$ m) stratified into mean wind speed and roughness length based on ASCE 7-10 exposure categories.

Terrain Type	ASCE 7 Exposure	Roughness Length Regimes	No. of 15-min data segments			
			WS1	WS2	WS3	Total
Suburban	B	$0.15 \text{ m} > z_0 \geq 0.7 \text{ m}$	507	233	105	845
Open country	C	$0.01 \text{ m} > z_0 \geq 0.15 \text{ m}$	483	350	760	1593
Very smooth	D	$z_0 < 0.01 \text{ m}$	73	129	499	701
Total			1063	712	1364	3139

Note: WS1 = $5 \text{ m/s} \leq U < 15 \text{ m/s}$, WS2 = $15 \text{ m/s} \leq U < 25 \text{ m/s}$, and WS3 = $U \geq 25 \text{ m/s}$

Table 2-3. Mean roughness lengths stratified into mean wind speed and roughness length ($z = 10$ m) based on ASCE 7-10 exposure categories.

Terrain Type	ASCE 7 Exposure	Roughness Length Regimes	Mean Roughness Length, z_0 (m)		
			WS1	WS2	WS3
Suburban	B	$0.15 \text{ m} > z_0 \geq 0.7 \text{ m}$	0.499	0.536	0.423
Open country	C	$0.01 \text{ m} > z_0 \geq 0.15 \text{ m}$	0.119	0.095	0.064
Very smooth	D	$z_0 < 0.01 \text{ m}$	0.005	0.004	0.004

Note: WS1 = $5 \text{ m/s} \leq U < 15 \text{ m/s}$, WS2 = $15 \text{ m/s} \leq U < 25 \text{ m/s}$, and WS3 = $U \geq 25 \text{ m/s}$

Table 2-4. Quadrants of events contributing to the total mean Reynold stress.

Quadrant (<i>i</i>)	u'	w'	Event
1	≥ 0	≥ 0	Outward interactions
2	≤ 0	≥ 0	Ejections
3	≤ 0	≤ 0	Inward interactions
4	≥ 0	≤ 0	Sweeps

Table 2-5. Equivalent full-scale roughness lengths obtained from suburban terrain BLWT simulation.

BLWT Test No.	Terraformer Configuration		BLWT Aerodynamic Parameters			Equivalent Full-Scale Roughness Length	
	Roughness Element Orientation	Element Height, h (mm)	U_{ref}/u_*	d/h	z_0/h	Geometric Scale	z_{0FS} (m)
1	Wide	20	29.9	0.131	0.021	400	0.171
2	Wide	30	16.4	0.131	0.076	100	0.227
3	Narrow	40	19.7	0.131	0.017	300	0.208
4	Narrow	60	16.5	0.131	0.037	120	0.267
5	Narrow	80	14.2	0.131	0.066	70	0.371
6	Narrow	100	12.5	0.131	0.095	60	0.572

Table 2-6. Statistics of 15-min records stratified into mean wind speed and roughness length based on ASCE 7-10 exposure categories.

ASCE 7-10 Exposure	U range (m/s)	U (m/s)		I_u		γ_{3u}		γ_{4u}	
		5-m	10-m	5-m	10-m	5-m	10-m	5-m	10-m
B	$5 \leq U < 15$	8.2	9.9	0.33	0.31	0.50	0.43	3.28	3.10
	$15 \leq U < 25$	17.8	20.8	0.31	0.30	0.55	0.47	3.28	3.05
	$U \geq 25$	28.6	32.8	0.29	0.28	0.53	0.41	3.24	2.97
C	$5 \leq U < 15$	9.3	10.5	0.25	0.23	0.36	0.30	3.06	2.97
	$15 \leq U < 25$	18.6	20.7	0.23	0.22	0.39	0.33	3.06	2.96
	$U \geq 25$	35.6	40.3	0.21	0.20	0.33	0.25	2.99	2.89
D	$5 \leq U < 15$	9.5	10.8	0.18	0.16	0.24	0.17	2.97	3.00
	$15 \leq U < 25$	18.2	20.5	0.19	0.17	0.28	0.24	2.99	2.99
	$U \geq 25$	37.7	42.6	0.17	0.15	0.21	0.17	2.93	2.90

Table 2-7. Mean stress fraction difference ΔS_0 between sweep and ejection stratified into mean wind speed and roughness length based on ASCE 7-10 exposure categories.

ASCE 7 Exposure	U range (m/s)	γ_{3u}		Measured ΔS_0		Theoretical ΔS_0	
		5-m	10-m	5-m	10-m	5-m	10-m
B	$5 \leq U < 15$	0.48	0.41	0.202	0.153	0.192	0.146
	$15 \leq U < 25$	0.49	0.41	0.229	0.161	0.222	0.155
	$U \geq 25$	0.49	0.37	0.239	0.132	0.227	0.126
C	$5 \leq U < 15$	0.31	0.28	0.093	0.090	0.094	0.087
	$15 \leq U < 25$	0.36	0.31	0.120	0.091	0.114	0.088
	$U \geq 25$	0.31	0.24	0.090	0.058	0.088	0.058
D	$5 \leq U < 15$	0.24	0.17	0.004	-0.012	0.004	-0.003
	$15 \leq U < 25$	0.26	0.22	0.036	0.024	0.038	0.024
	$U \geq 25$	0.21	0.17	0.021	-0.005	0.026	0.000

Table 2-8. Proposed exposure coefficient values obtained from non-Gaussian peak factor model

Height above ground level, z		γ_{3u}	Peak factor, $g_{NG}(t = 3s)$	Suburban exposure coefficient, K_z		% Increase
ft	(m)			Proposed (K_{zNG})	ASCE 7-10 Exposure B	
15	4.6	0.46	3.48	0.63	0.57	+9.8
20	6.1	0.43	3.44	0.70	0.62	+12.3
25	7.6	0.39	3.40	0.75	0.66	+13.5
30	9.1	0.35	3.36	0.80	0.70	+14.0
40	12.2	0.27	3.28	0.86	0.76	+13.9
50	15.2	0.20	3.21	0.91	0.81	+13.0
60	18.3	0.12	3.13	0.95	0.85	+11.7
70	21.3	0.04	3.05	0.98	0.89	+10.2
80	24.4	0.00	3.01	1.01	0.93	+9.3

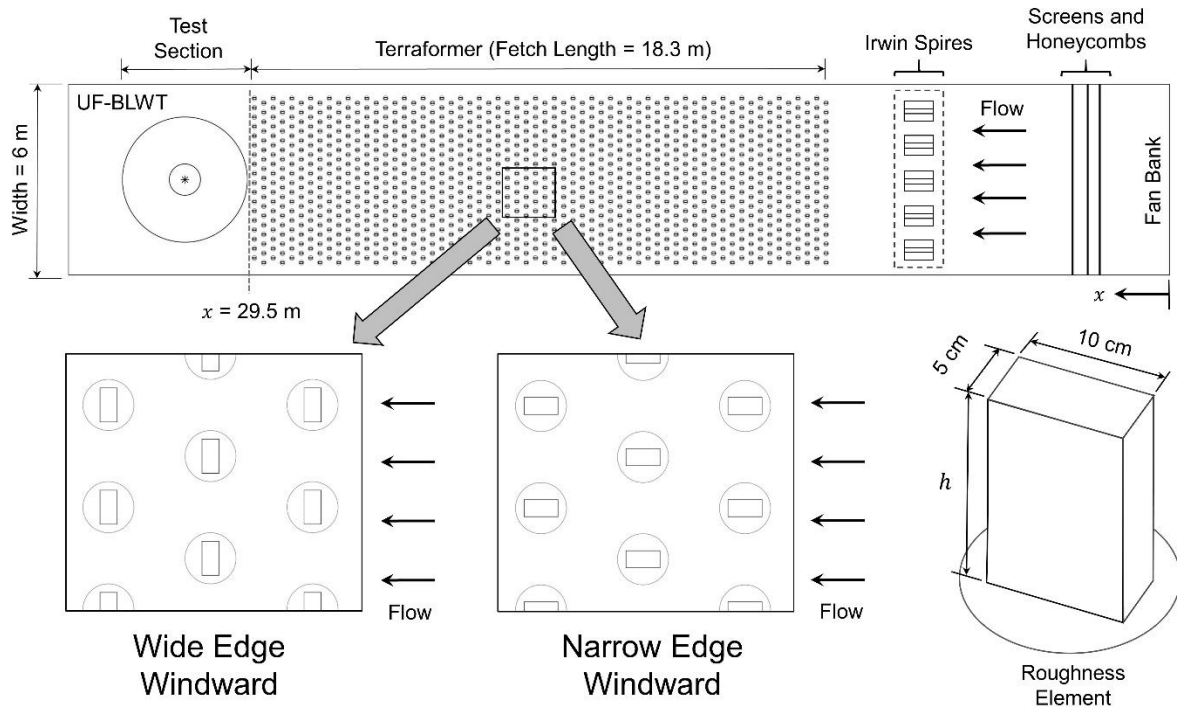


Figure 2-1. Plan view of the BLWT at the University of Florida, illustrating the two element orientations considered for this study, namely wide and narrow edge windward.

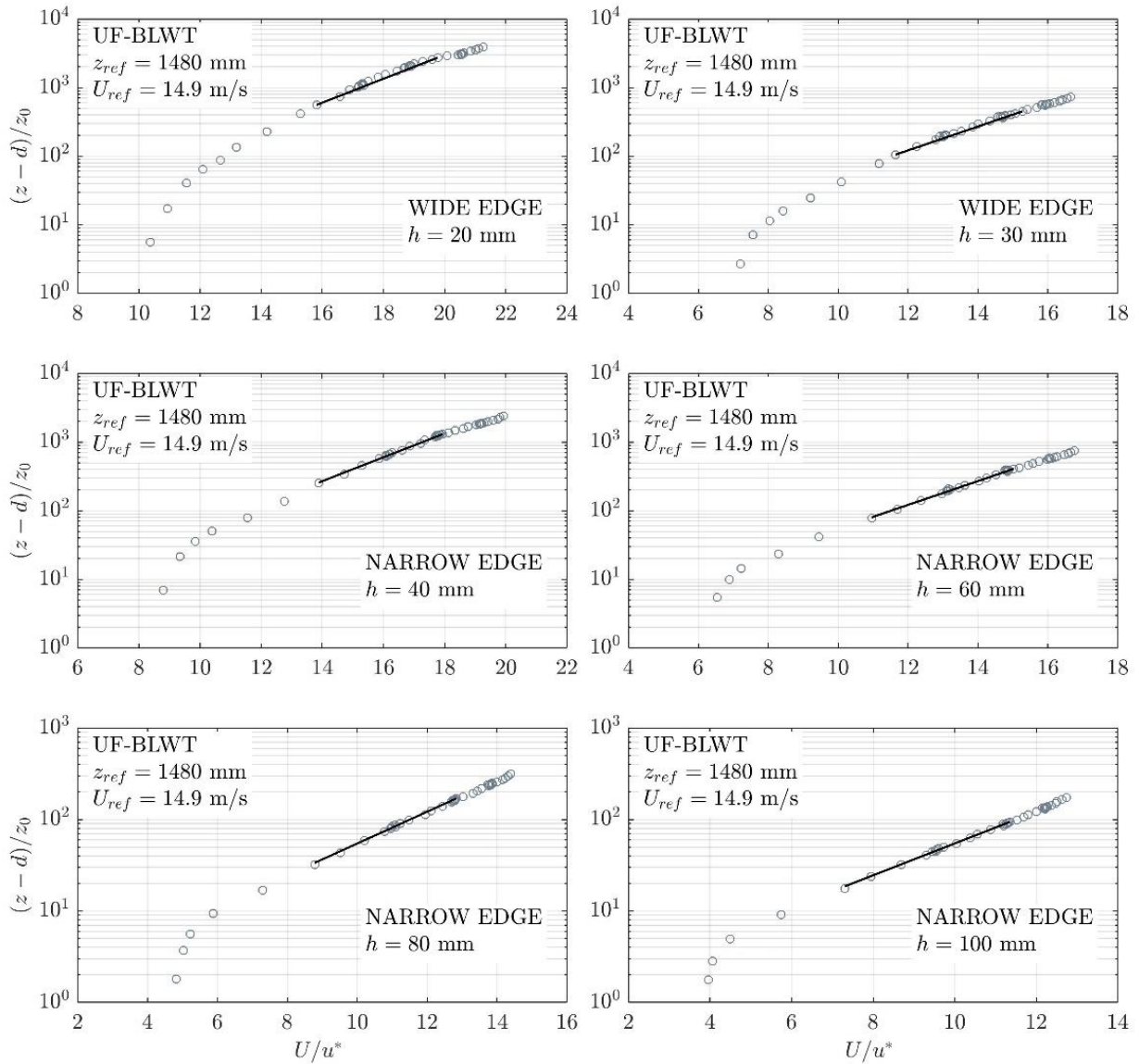


Figure 2-2. Spatially averaged mean velocity profiles of six independent BLWT simulations measured at location $x = 29.5$ m.

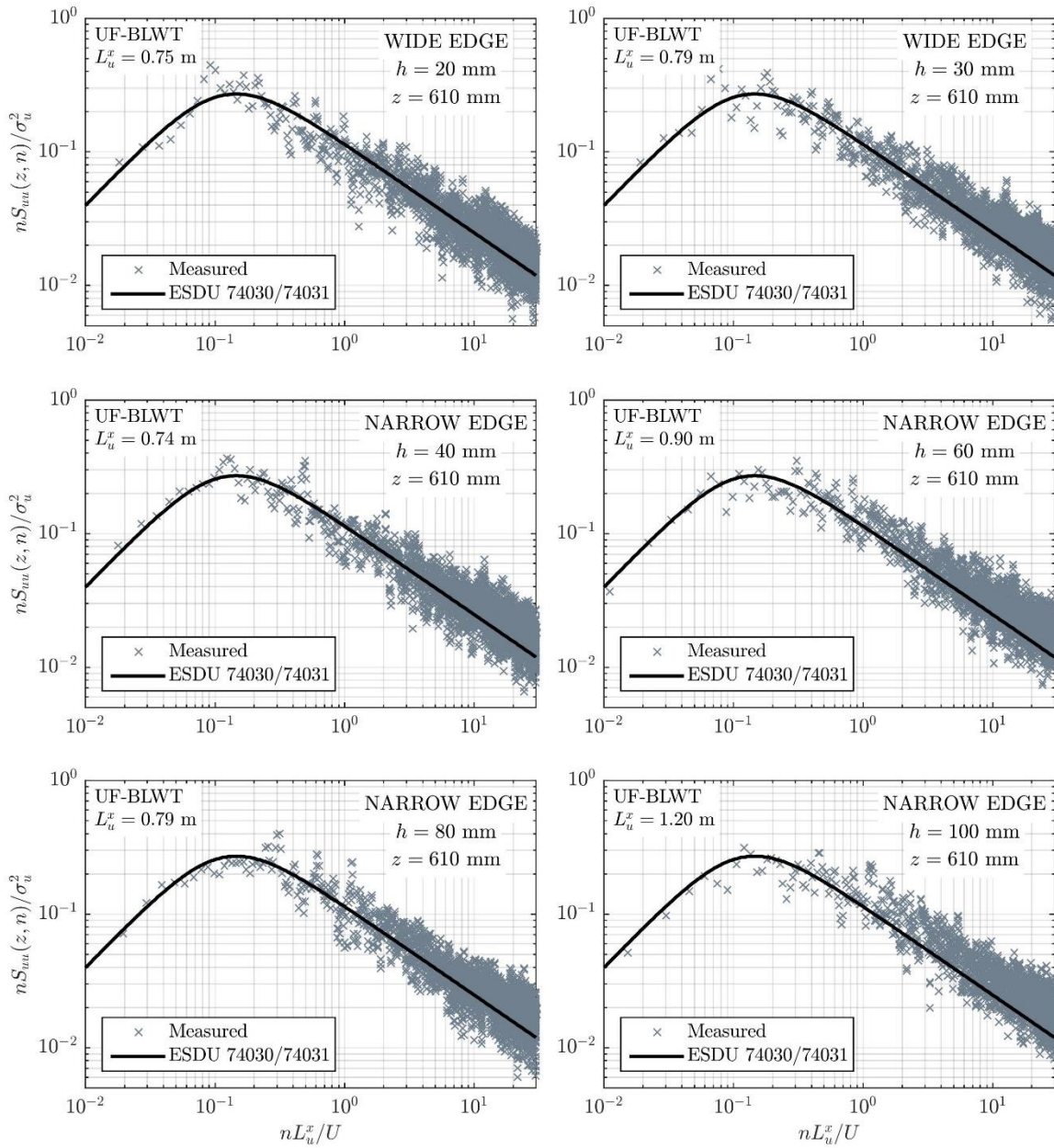


Figure 2-3. Longitudinal turbulence spectra of six independent BLWT simulations, measured at location $x = 29.5$ m ($z = 610$ mm).

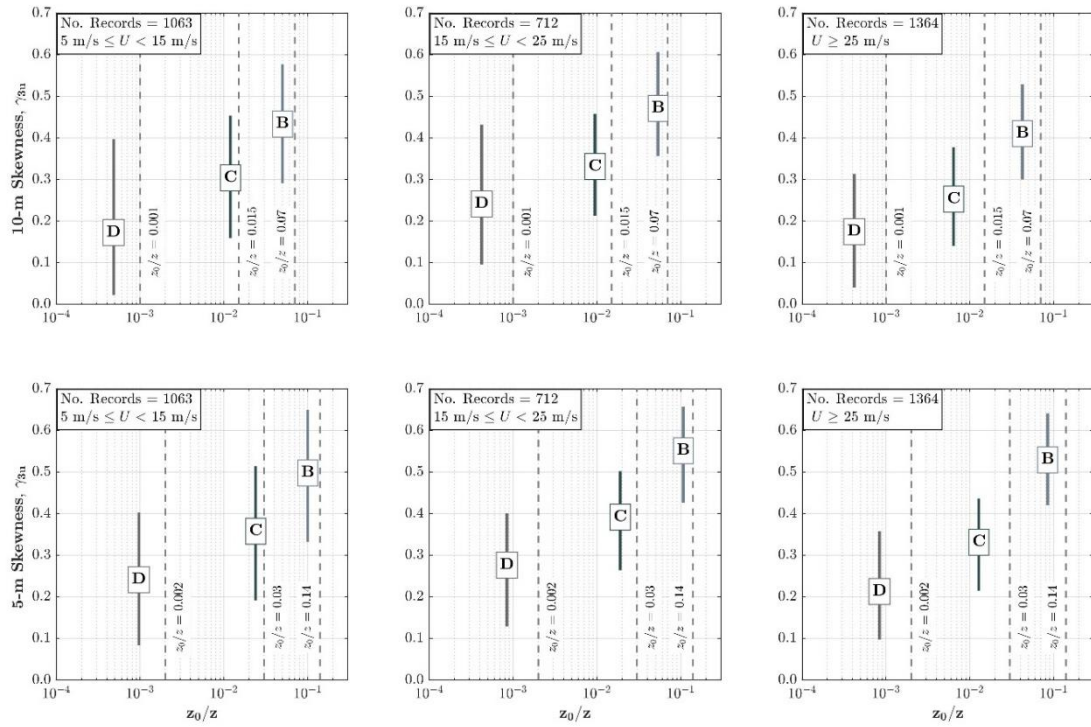


Figure 2-4. Observed mean (longitudinal) skewness values stratified into mean wind speed and terrain roughness.

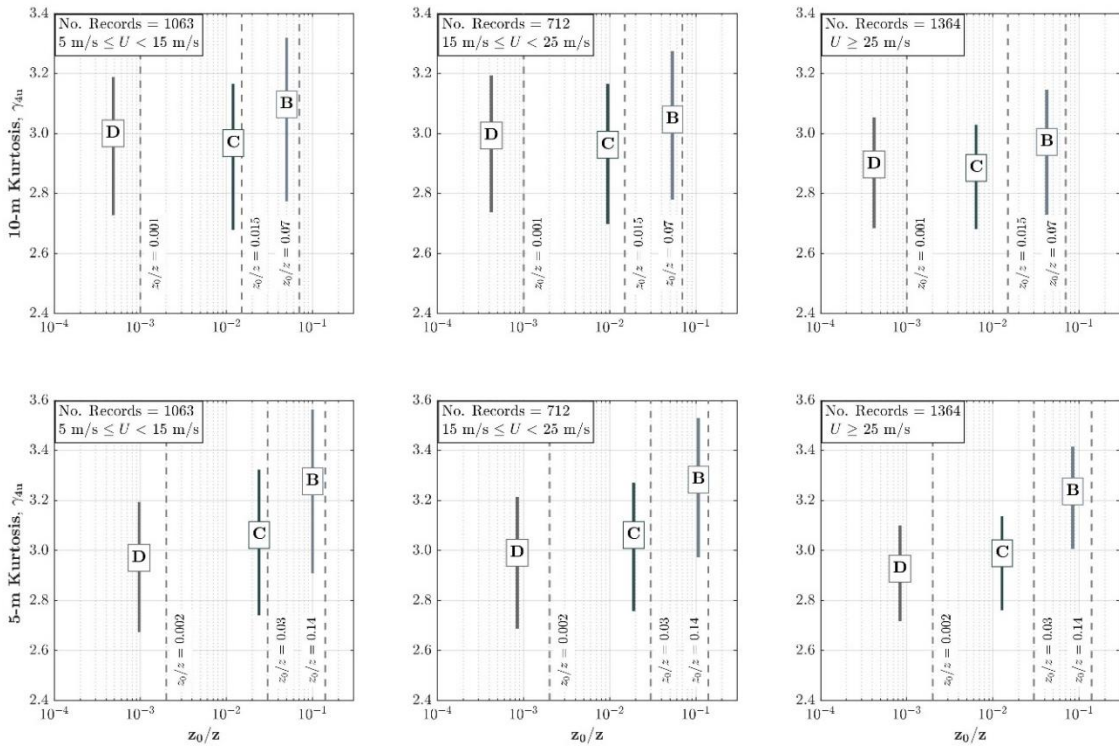


Figure 2-5. Observed mean (longitudinal) kurtosis values stratified into mean wind speed and terrain roughness.

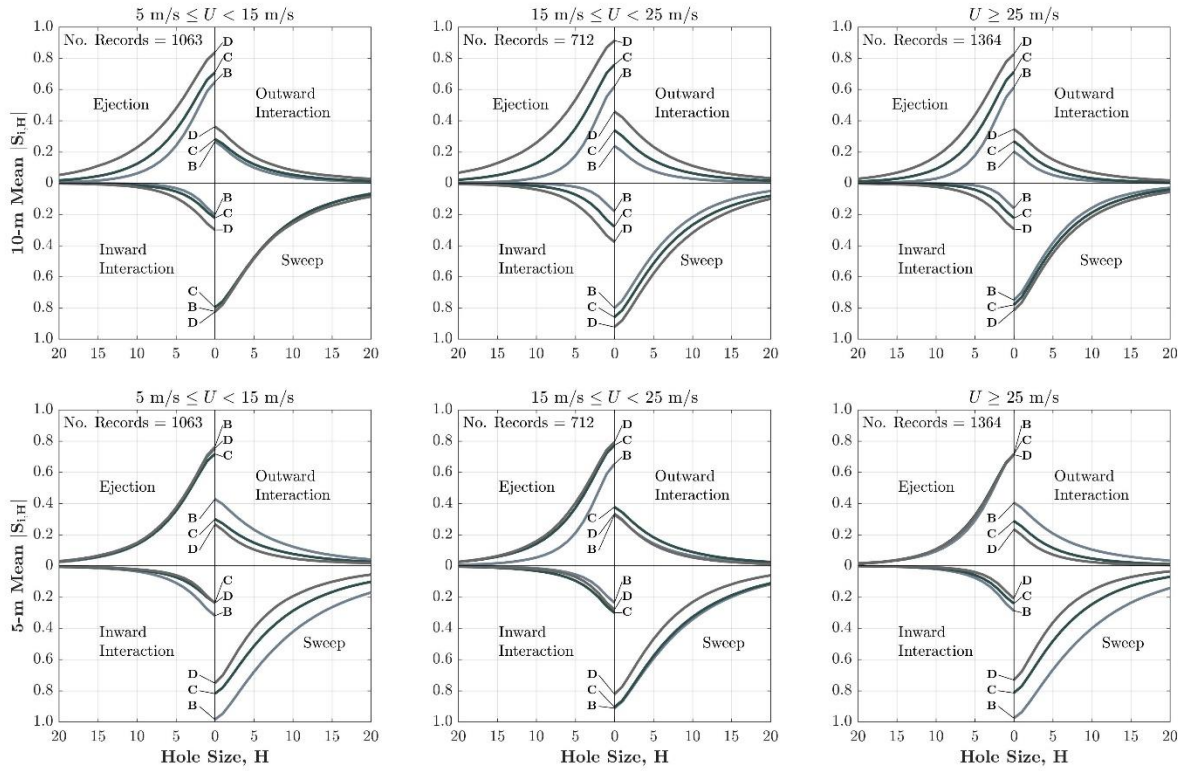


Figure 2-6. Mean Reynolds stress fractions $|S_{i,H}|$ for mean wind speed values stratified into mean wind speed and terrain roughness for the field observations.

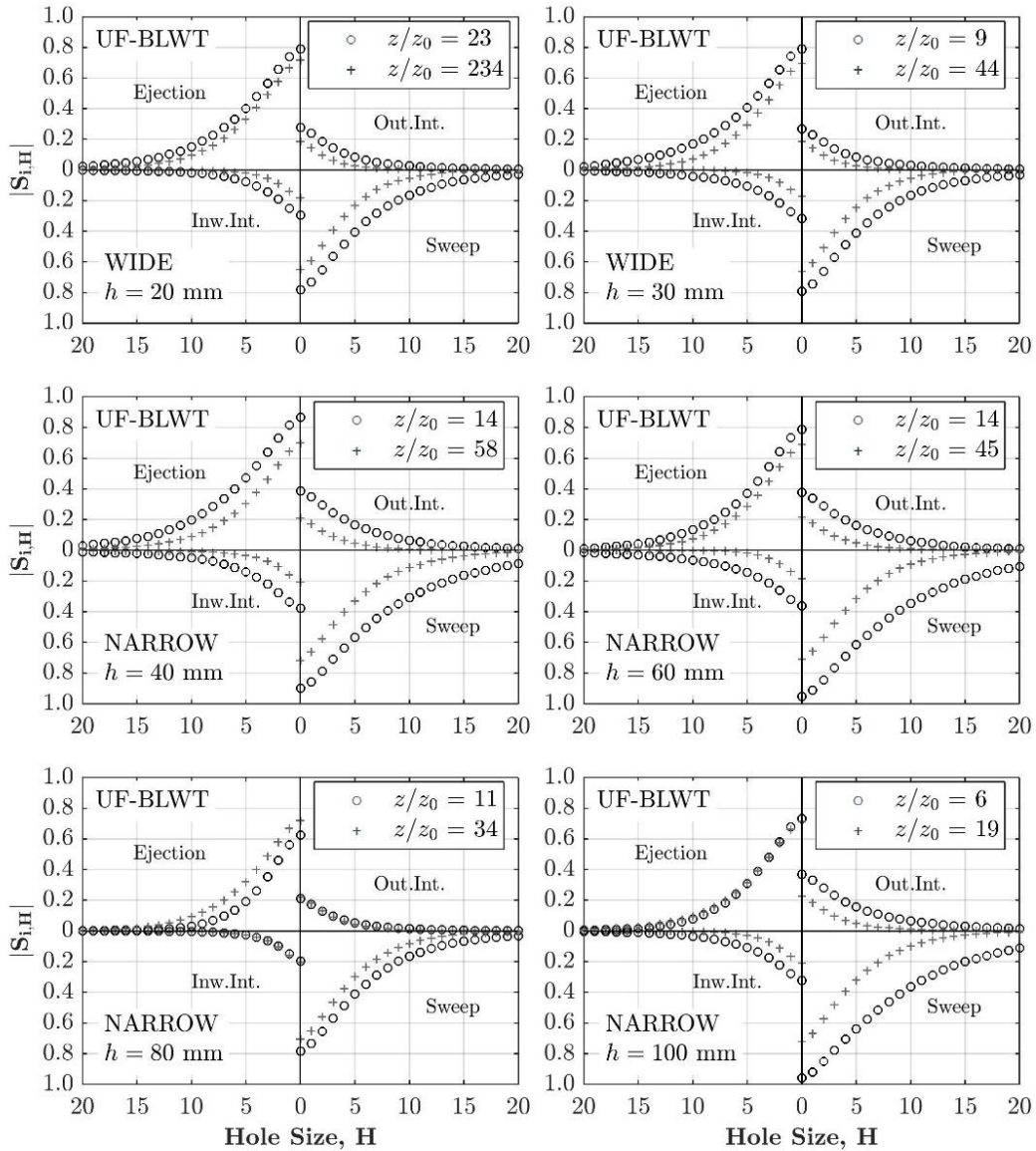


Figure 2-7. Spatially averaged Reynolds stress fractions $|S_{i,H}|$ of six independent BLWT simulations measured at location $x = 29.5$ m.

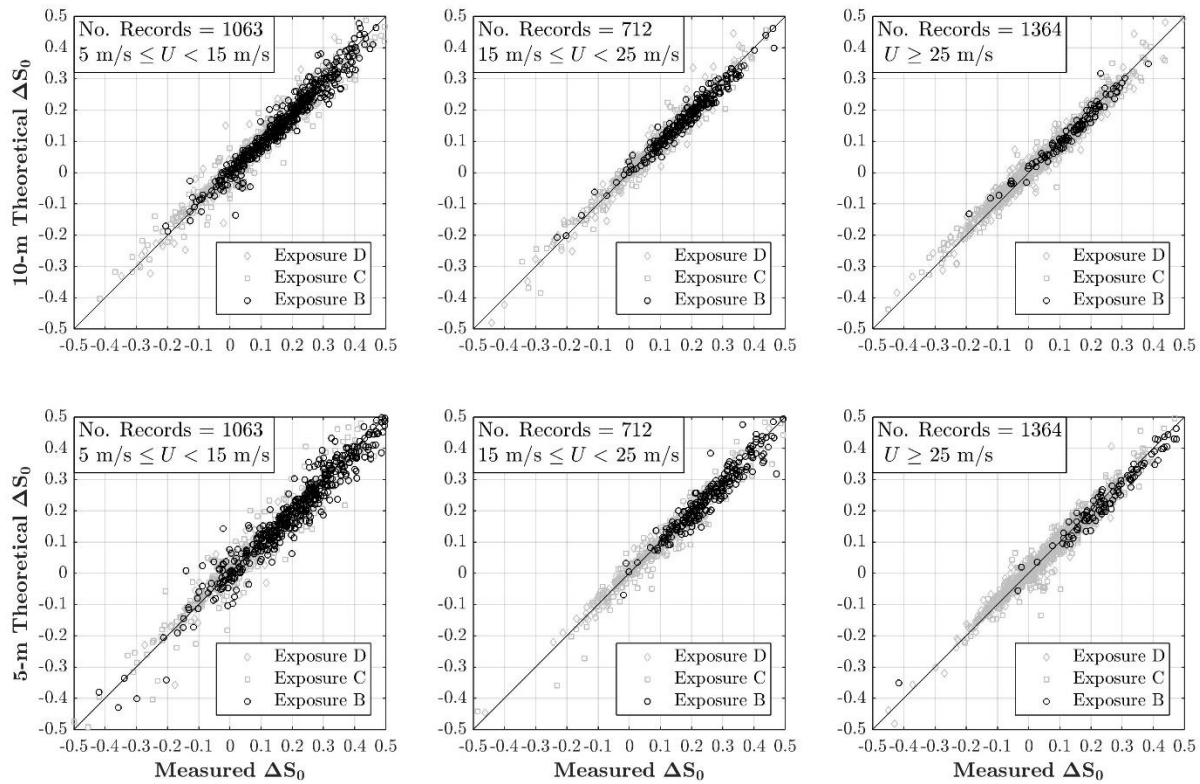


Figure 2-8. Theoretical and measured stress fraction difference ΔS_0 between sweep and ejection quadrants for mean wind speed values stratified into mean wind speed and terrain roughness. Suburban (Exposure B) measurements are denoted by black circular markers.

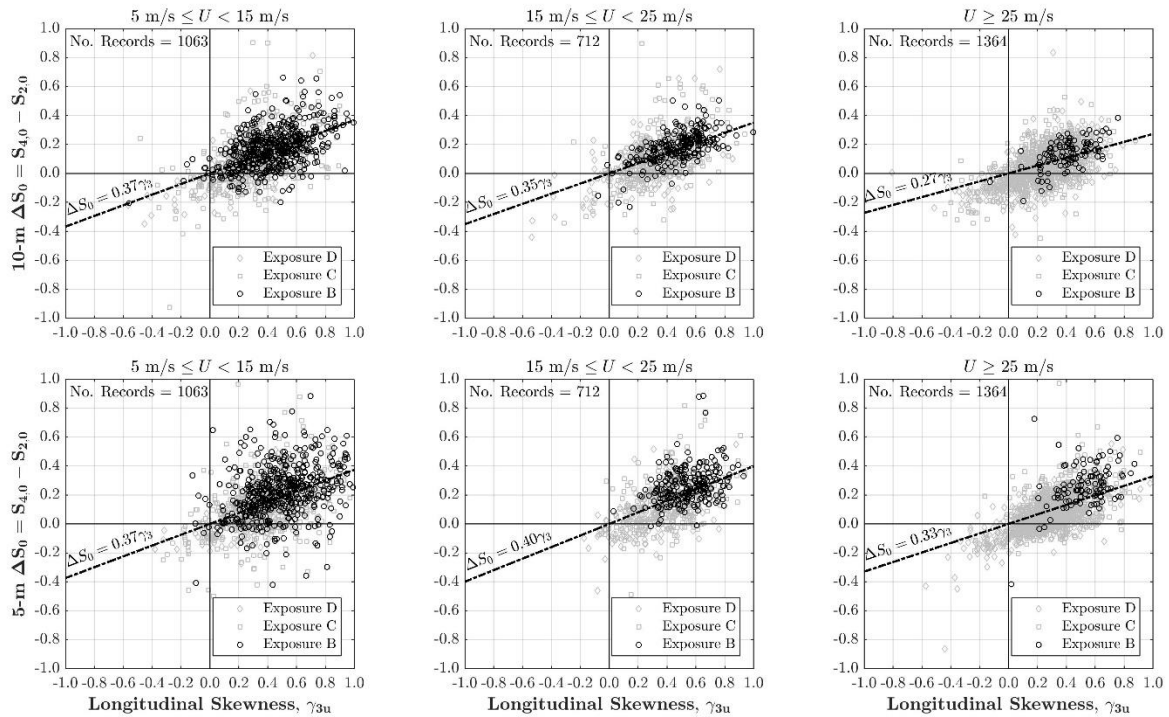


Figure 2-9. Measured stress fraction difference ΔS_0 versus longitudinal skewness for mean wind speed values stratified into mean wind speed and terrain roughness. Suburban (Exposure B) measurements are denoted by black circular markers.

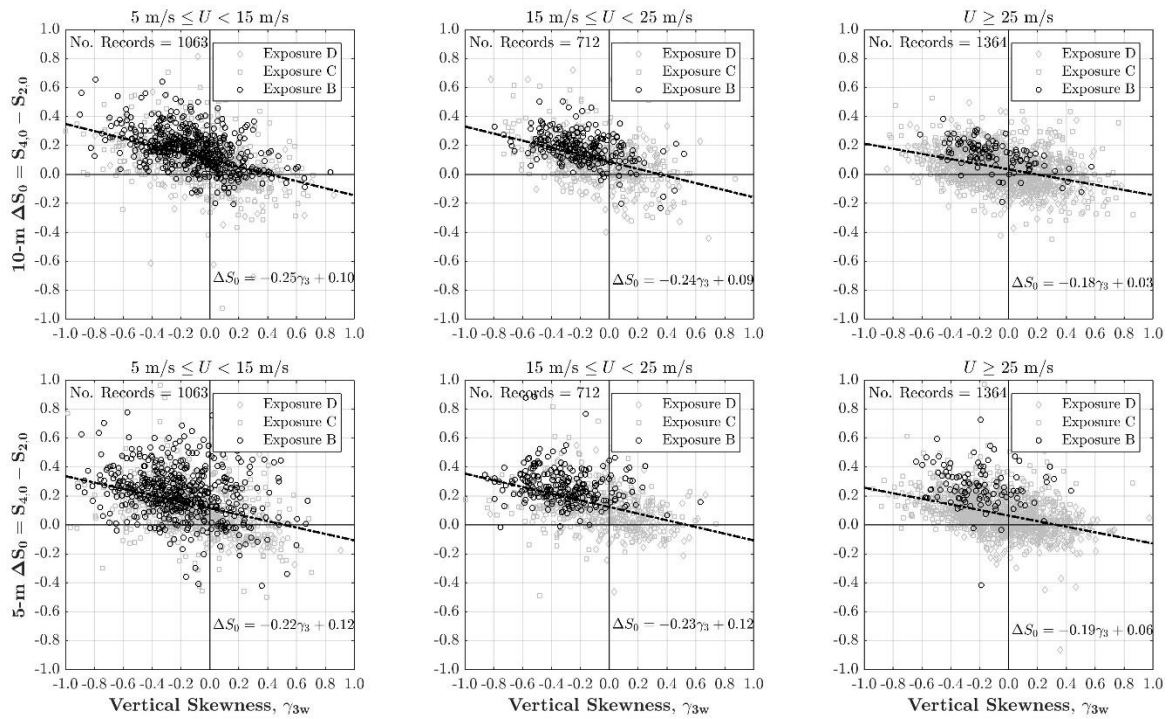


Figure 2-10. Measured stress fraction difference ΔS_0 versus vertical skewness for mean wind speed ranges: (a) 5 m/s-15 m/s, (b) 15 m/s-25 m/s, and (c) greater than 25 m/s. Suburban (Exposure B) measurements are denoted by black circular markers.

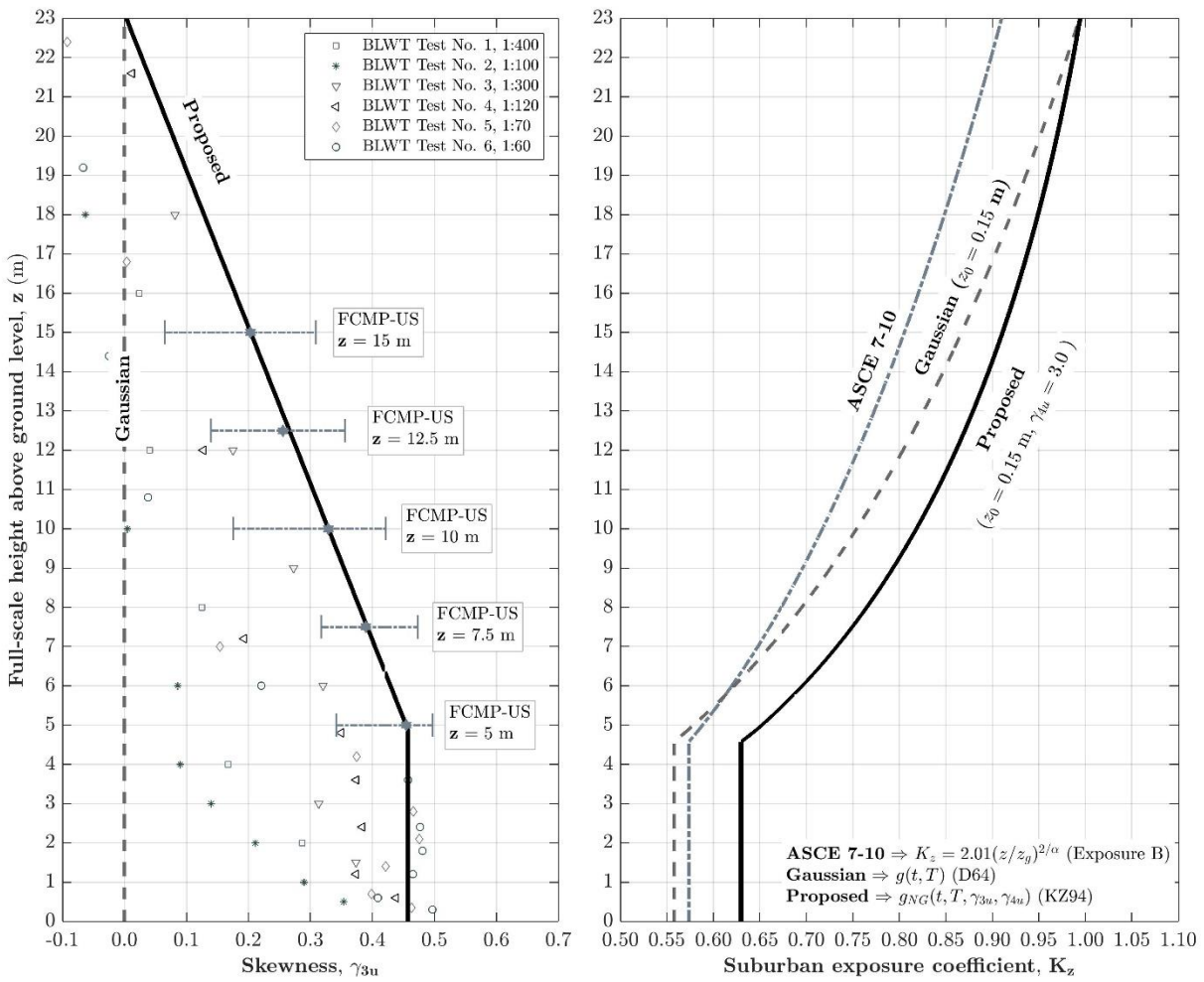


Figure 2-11. Proposed non-Gaussian exposure coefficient K_z versus elevation above ground z .

CHAPTER 3 WIND SIMULATION IN A LARGE BOUNDARY LAYER WIND TUNNEL

This chapter presents results from a series of flow measurements in a large boundary layer wind tunnel for validation of a computer controlled terrain generator and gives a detailed description of the flow conditioning and mixing devices of the BLWT, instrumentation utilized for flow measurements, and validation models for adequate simulation of the atmospheric boundary layer (ABL) for testing of building models.

Background

Despite significant advancements in computational modeling of boundary layer flows (e.g., CFD, LES), boundary layer wind tunnel (BLWT) testing still remains an indispensable tool for simulation of complex turbulent flows. BLWTs require adequate simulation of the atmospheric boundary layer (ABL), the lowest part of the atmosphere where the air flow is influenced by the Earth's surface. Although there is ongoing debate about what characteristics of the ABL should be match in wind tunnels, statistics of primary interest for wind engineering applications include: (1) mean longitudinal velocity component, (2) longitudinal turbulence intensity, (3) power spectral densities, and (4) integral scales in the along, across, and vertical directions.

Satisfying similarity requirements of ABL characteristics and test models is still a topic of discussion among wind tunnel modelers. Properly scaling the mean velocity and turbulence characteristics of the ABL to match a scaled model is typically a trial and error process. The natural scaling of the ABL in wind tunnels is in the range 1:400 to 1:600 (Davenport, 2007), thus test models should be built at similar geometric scales. This is readily achievable for tall building models. However, low-rise models with detailed features require larger geometric scales ranging (from 1:20 to 1:100) to better

capture flow separation regions as well as wind effects on building features such as parapets and chimneys. Additional flow modification devices are used to grow the ABL (i.e., scale-up the approach flow) and achieve better agreement between the scale of the model and the approach flow. Modification devices such as barriers, vortex generators, and spires have been employed to stimulate the growth of turbulent boundary layers.

Approach to Modeling

ESDU Model

The turbulent structure of the ASL, in strong winds, can be described by the boundary layer model developed in Harris and Deaves (1981), which introduces the effect of surface friction and Coriolis forces close to the Earth's surface. Near the ground (< 50 m), friction effects control and the mean velocity profile follows the "law of the wall"

$$V_z = 2.5u_* \ln(z/z_0) \quad (3-1)$$

where V_z is the longitudinal wind velocity (typically mean hourly) at elevation z , u_* is the friction (shear) velocity and z_0 is the aerodynamic roughness length. The longitudinal turbulence intensity is defined as the standard deviation of the velocity (σ_u) divided by the mean velocity and is expressed analytically as

$$\sigma_u = \frac{7.5\eta u_* [0.538 + 0.09 \ln(z/z_0)]^{\eta^{16}}}{1 + 0.156 \ln[u_*/(fz_0)]} \quad (3-2)$$

where $\eta = 1 - 6fz/u_*$, f is the Coriolis parameter = $2\omega \sin \phi$, in which $\omega = 72.9 \times 10^{-6}$ rad/s and ϕ = latitude in degrees.

If the turbulence intensity and mean velocity are known for a specific height z , z_0 and u_* can be obtained through a bounded nonlinear function minimization that simultaneously satisfies Equations 3-1 and 3-2. This procedure excludes the zero-plane displacement height, which is an important parameter for more built-up terrain (e.g., suburban).

Morphologic Models for Roughness Length Estimates

A wide range of approaches can be found in literature (e.g., Lettau, 1969; Counihan, 1971; Macdonald, 1998) to estimate surface roughness from the geometric arrangement of upstream obstacles. Lettau (1969) suggested a simple expression for estimating the roughness length for a uniform array of obstacles

$$z_0 = 0.5H \frac{A_f}{A_d} = 0.5H\lambda_f \quad (3-3)$$

where H is the mean obstacle height, A_f is the total frontal area of the obstacle, and A_d is the total plan area of the obstacles. This method for estimating roughness length is included in the Commentary section of ASCE 7-10 (2010). Equation 3-3 only applies for roughness area densities (i.e., λ_f) below 20-30% (Macdonald et al., 1998).

Macdonald et al. (1998) presented an improved method for the estimation of surface roughness, which accounts for the nonlinear decrease of roughness length at high roughness densities (i.e., $\lambda_f > 20\%$). Additionally, the model explicitly includes the drag coefficient (C_D) of the obstacles, based on the shape and layout of the roughness array, and the zero-plane displacement height (d). This results in the following expression:

$$\frac{z_0}{H} = \left(1 - \frac{d}{H}\right) \exp \left[- \left(0.5\beta \frac{C_D}{\kappa^2} \left(1 - \frac{d}{H}\right) \lambda_f \right)^{-0.5} \right] \quad (3-4)$$

where β is a multiplicative factor, which may be calibrated against experimental data. The displacement height (d) $d/h = 1 + A^{-\lambda}(\lambda_p - 1)$ in which λ_p is the plan area index defined as the ratio of the plan area of the roughness obstacles and A_d .

Methodology

Wind Tunnel

Experiments were carried out at University of Florida's Boundary Layer Wind Tunnel (BLWT), a low-speed open circuit tunnel with dimensions of 6 m W x 3 m H x 38 m L. Figure 3-1 shows a schematic plan drawing of the tunnel. The inlet of the tunnel houses eight vane axial fans, each driven by a 75 hp (56 kW) electric motor. Flow conditioning system consists of five sets of screens and honeycombs, located approximately 3 m downwind of the fans (Figure 3-2). The test section (1 m turntable) is located 31.5 m from the fan bank. The air speed through the test section can be set from 1 to 16 m/s (measured at a reference height). The tunnel is instrumented with reference anemometry (Figure 3-3) for static pressure measurements at specific locations along the streamwise direction. Reference velocity in the tunnel is taken at an elevation of 1.48 m above the floor using Pitot tubes (Figure 3-4), located approximately 2.5 m upwind of the center of the turntable. The ceiling of the tunnel is adjustable, which allows for zero pressure gradient along the length of the test section. Data is collected from a meteorological station (Figure 3-5) is in close proximity to the exit of the tunnel for monitoring of local atmospheric conditions.

Roughness Element Grid and Vortex Generators

Passive mixing devices in the tunnel include Irwin spires, downwind of the screens and honeycombs (Figure 3-6), and a computer controlled roughness array named the Terraformer, a 62 X 18 roughness element grid that rapidly reconfigures the height and orientation of 1116 roughness elements to achieve desired upwind terrain conditions. The grid extends nominally 18.3 m along the length of the tunnel.

Dimensions of the elements are 5 cm by 10 cm, and they are spaced 30 cm apart in a staggered pattern. Height and orientation can be varied from 0-160 mm and 0-360 degrees, respectively. The narrow and wide edge cases refer to the 5 cm and 10 cm face perpendicular to the flow, respectively. The height and orientation of each element in the roughness grid is controlled through LabView software. Consequently, the Terraformer can readily simulate an extensive series of homogeneous and heterogeneous terrains. Reconfiguration of all 1116 elements is typically achieved in less than 60 seconds.

Flow Measurements

An automated (computer controlled) gantry system was used for three-dimensional mapping of the flow. The gantry traverses four velocity probes in the three-orthogonal directions (i.e., three translational degrees of freedom) of the tunnel, namely along (x), across (y) and vertical (z). The position and probe parameters (e.g., sampling rate and duration) is controlled through LabView code. Velocity sensors consist 3-hole (i.e., taps) Cobra pressure probes from Turbulent Flow Instrumentation (TFI). The probes measure u , v , and w velocity components and static pressure within a $\pm 45^\circ$ acceptance cone. Response characteristics include a maximum frequency response of 2 kHz and a 2-100 m/s sensing range. Accuracy of the probes is typically between ± 0.5

m/s, although this is dependent on the turbulence levels. The probes remain relatively accurate for turbulence intensities greater than 30%. Pressure data from the four taps of the probe are measured by a data-acquisition (DAQ) system and processed by the TFI Device Control software to resolve the three components of the flows and static pressure measurements.

Experimental Design

For this experiment, 32 homogeneous terrain configurations were examined. The roughness element grid was raised (uniformly) from 10-160 mm, using 10 mm increments. Vertical and lateral traverses were taken for each element height increment for both narrow and wide edge windward element orientations.

Time histories of the u , v , and w components of the approach flow were measured at the test section ($x = 31.52$ m).. Vertical traverses consisted of 44 measurements along the height of the tunnel from $z = 5$ -1670 mm using cobra probes. Three lateral traverses were taken across the width of the tunnel—at the centerline and ± 500 mm off the centerline of the tunnel. A triple rotation procedure described in Foken and Nappo (2008) was performed to align the probe coordinate system into the streamlines and towards the mean flow coordinate system. Measurements for each probe position were collected for 30 seconds at a sampling rate of 1250 Hz.

Results and Discussion

Mean Velocity Profiles

Figures 3-7 and 3-8 show subplots of spatially averaged mean velocity profiles for a narrow and wide edge windward element orientation, respectively. Mean velocities are normalized by the reference wind velocity U_{ref} , at a height of $z_{ref} = 1670$ mm. The reference wind velocity appeared to mildly increase with increasing element height. A

noticeable difference in the shape of the profiles between wide and narrow edge windward element orientations is observed for high element heights ranging from 80 to 160 mm. The profile curves in Figure 3-8 (wide case) contain inflection points at approximately 500 mm for high element height. This is not observed in the narrow case. Furthermore, a small inner boundary layer (IBL) appears to be forming close to the tunnel. This might be a result of the rough to smooth transition between the test section and the last row of roughness elements.

Semi-logarithmic mean velocity profiles are depicted in Figures 3-9 and 3-10 for both element orientations. Roughness length (z_0) and shear velocity (u_*) values were obtained from a non-linear least-square fit of the logarithmic law (Equation 3-1) following Karimpour et al. (2012). The zero-plane displacement height (d) was estimated based on the morphometric models of roughness arrays found in Macdonald et al. (1998). The logarithmic fits were limited to data points in the inertial sublayer (ISL), above the wake region. Aerodynamic parameters for 16 element heights and two element orientations are presented in Table 3-1. For the same element height, larger roughness length estimates and shear velocities were obtained from the wide edge windward element orientation.

Turbulence intensity Profiles

Turbulence intensity profiles of the longitudinal velocity component (I_u) for a narrow and wide edge windward element orientation, respectively, are shown in Figures 3-11 and 3-12. The profiles suggest that a greater range of turbulence intensity levels can be generated by orienting the roughness elements in a wide edge windward manner. For an element height of 160 mm (wide), I_u values can exceed 30% below

500 mm. In comparison, maximum turbulence levels for the narrow case are around 22% at elevations below 200 mm.

Figures 3-13 and 3-14 include profiles of the lateral turbulence component (I_v). Below $z = 100$ mm, the wide element orientation can achieve I_v levels ranging from 7-29%, while the narrow case can generate lateral turbulence levels between 8-23%. Vertical turbulence intensity (I_v) profiles are shown in Figures 3-15 and 3-16 for the two element orientations. Maximum I_v values for the wide edge orientation occurs at approximately 250 mm above the floor. The peak I_v for the narrow case happens at $z = 100$ mm.

Summary

This chapter presents results from an extensive series of flow measurements in a large boundary layer wind tunnel (BLWT) for validation of the Terraformer, a computer controlled roughness element grid. Three-dimensional instantaneous velocities were measured at the BLWT's test section using an automated gantry, instrumented with Cobra probe sensors, for a wide range of homogeneous terrain configurations. Aerodynamic parameters, such as shear velocity and roughness length, were obtained from a non-linear least square fit of the "log law" to mean velocity profiles. Longitudinal turbulence intensity values in the range of 6 to 32 were observed at elevations below 500 mm from the tunnel floor. The wide edge windward element orientation generates higher turbulence levels.

Table 3-1. BLWT aerodynamic parameters.

h (mm)	z_0 (m)		u_* (m/s)		U_{ref} (m/s) ($z = 1.67$ m)	
	Narrow	Wide	Narrow	Wide	Narrow	Wide
10	0.0018	0.00291	0.883	0.966	15.290	15.508
20	0.0026	0.00564	0.944	1.094	15.415	15.594
30	0.0041	0.01075	1.014	1.246	15.465	15.708
40	0.0070	0.02250	1.135	1.480	15.536	15.712
50	0.0081	0.03649	1.172	1.678	15.573	15.730
60	0.0121	0.04832	1.275	1.825	15.486	15.794
70	0.0136	0.06327	1.315	1.990	15.616	15.980
80	0.0153	0.06885	1.348	2.039	15.628	15.966
90	0.0194	0.08751	1.433	2.237	15.703	16.069
100	0.0213	0.09081	1.466	2.250	15.686	16.126
110	0.0244	0.09406	1.522	2.290	15.778	16.252
120	0.0305	0.10140	1.619	2.349	15.868	16.271
130	0.0336	0.11345	1.663	2.446	15.804	16.298
140	0.0354	0.10582	1.692	2.327	15.858	16.250
150	0.0410	0.11514	1.769	2.438	15.838	16.322
160	0.0453	0.13393	1.832	2.587	15.933	16.279



Figure 3-1. Boundary layer wind tunnel (BLWT) at the University of Florida (Photo courtesy of John Jernigan).



Figure 3-2. Set of screens and honeycomb system downwind of the fan bank (Photo courtesy of author).



Figure 3-3. Pitot tube mounted to the wall of the tunnel (located at the test section)
(Photo courtesy of author).

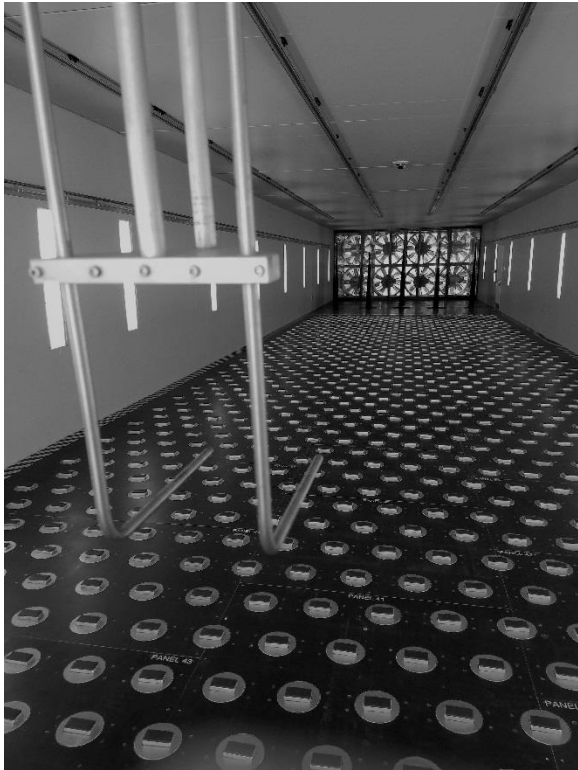


Figure 3-4. Freestream reference anemometry (Pitot tubes) (Photo courtesy of author).



Figure 3-5. Meteorological weather station located adjacent to the exit of the BLWT (Photo courtesy of author).



Figure 3-6. Irwin spires located downwind of the screens and honeycomb (Photo courtesy of author).

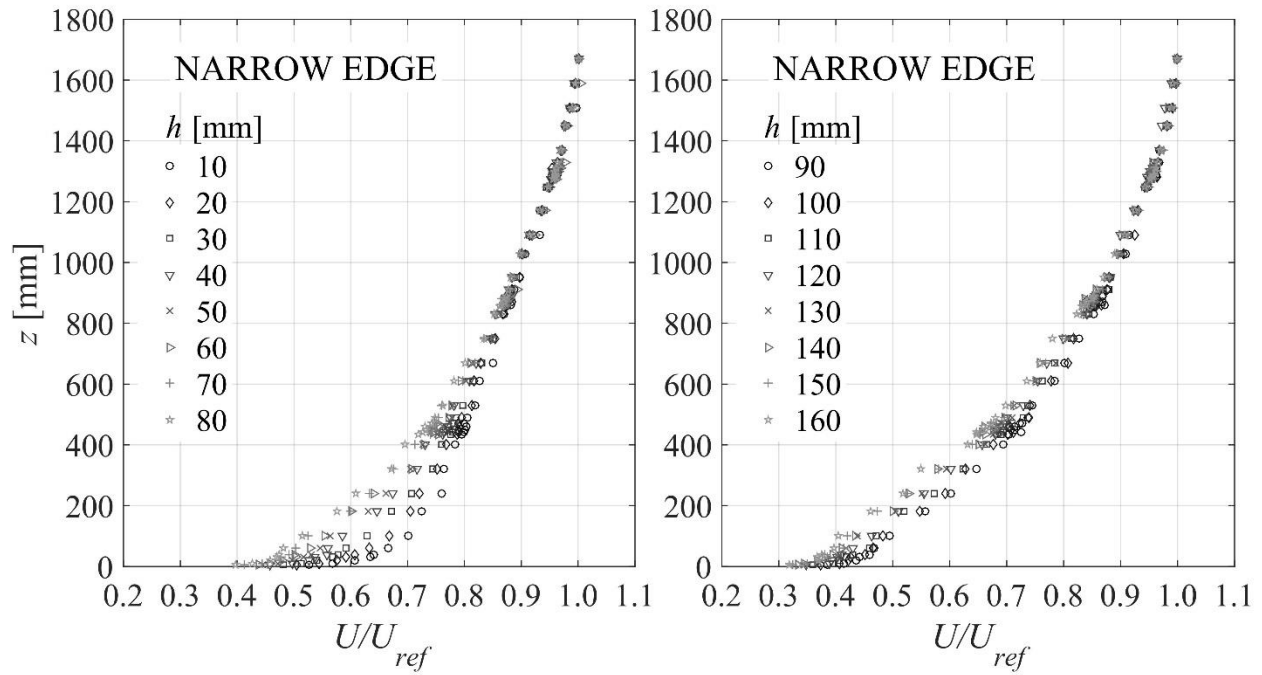


Figure 3-7. Longitudinal Mean velocity profiles for a narrow edge windward element orientation.

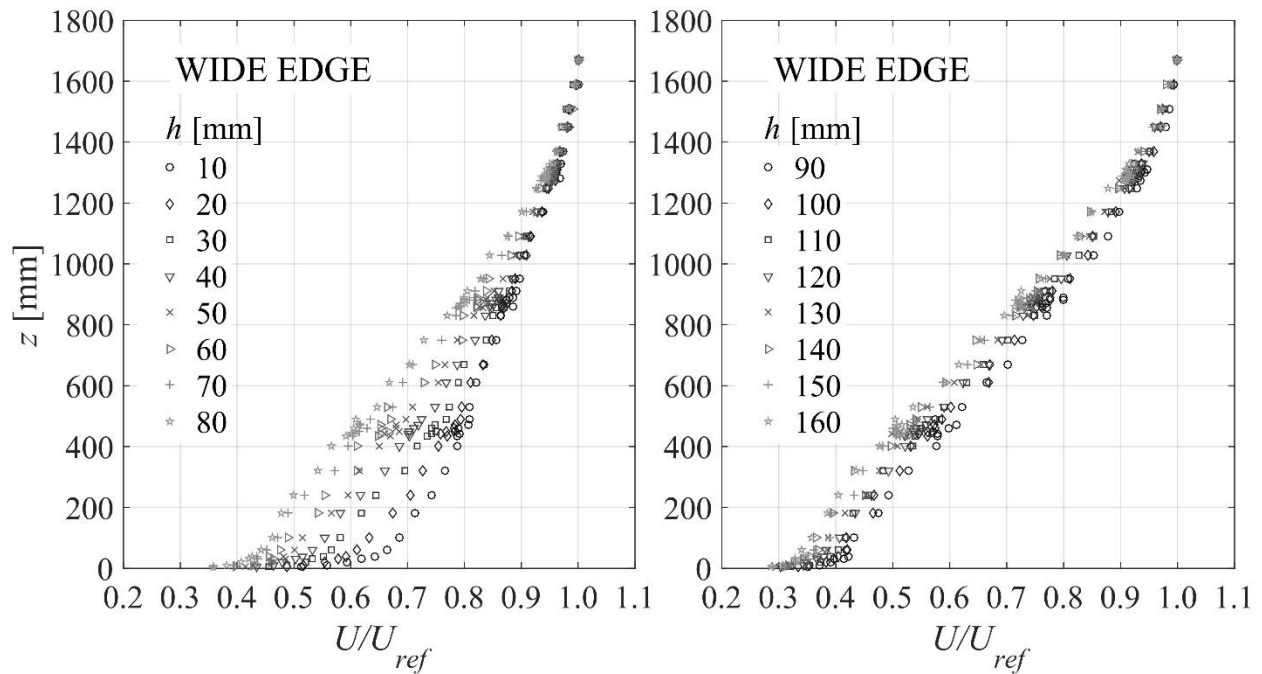


Figure 3-8. Longitudinal Mean velocity profiles for a wide edge windward element orientation.

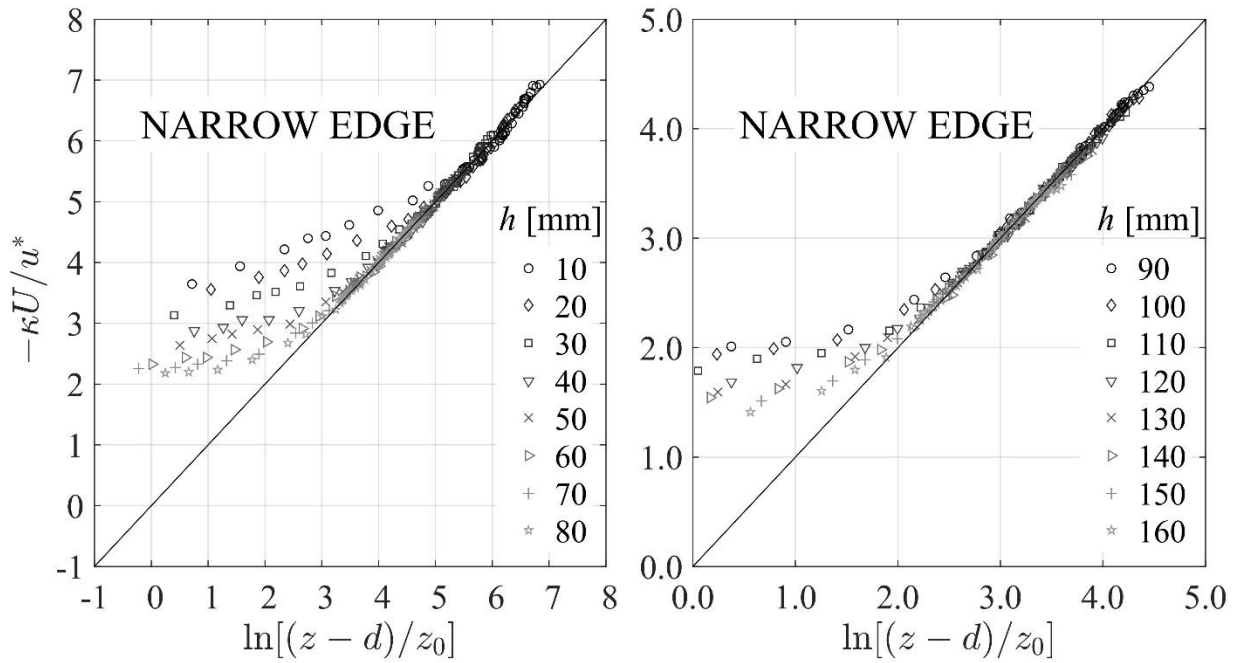


Figure 3-9. Semi-logarithmic mean velocity profiles for the narrow edge windward element orientation.

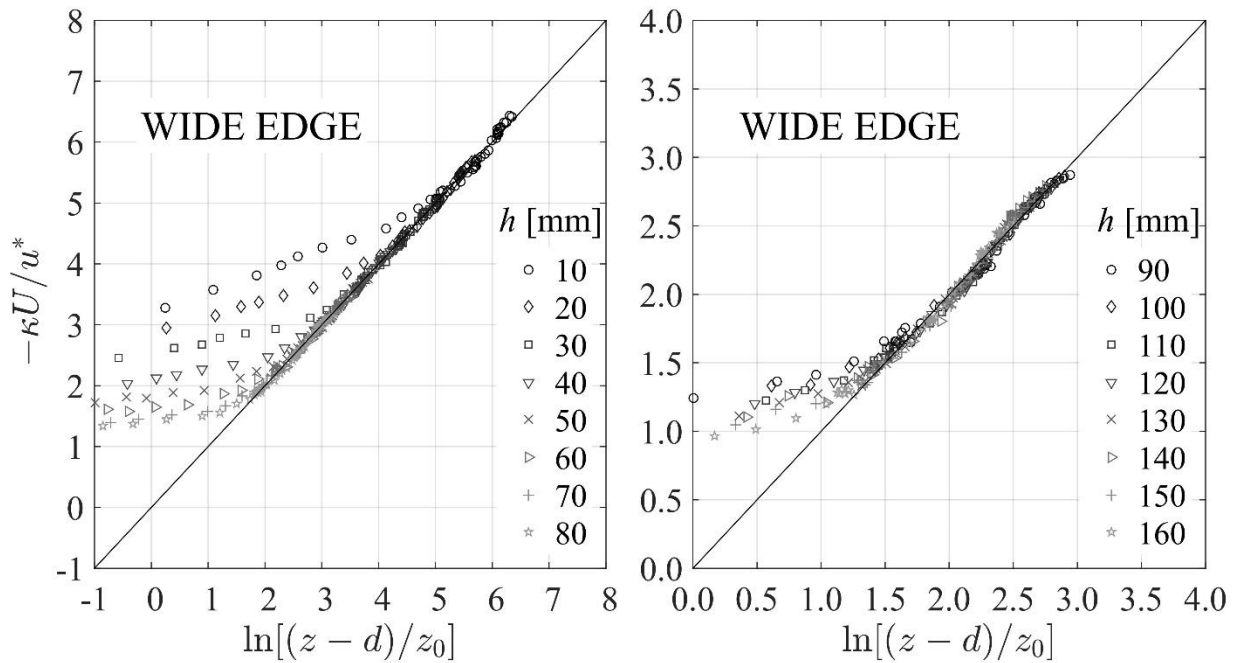


Figure 3-10. Semi-logarithmic mean velocity profiles for the wide edge windward element orientation.

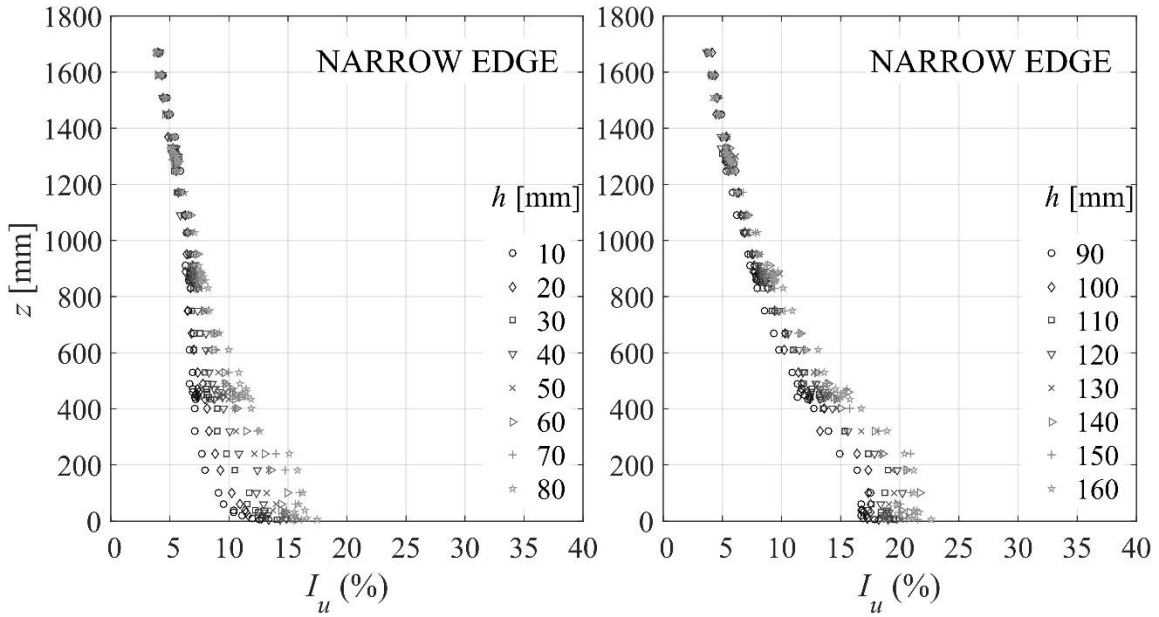


Figure 3-11. Longitudinal turbulence intensity profiles for a narrow edge windward element orientation.

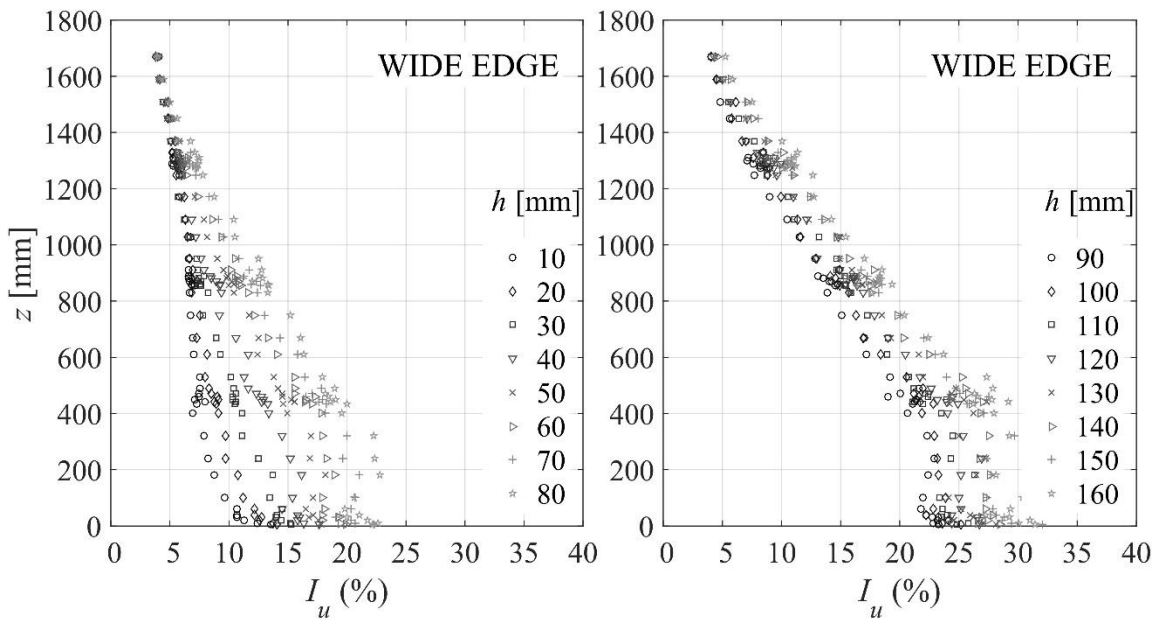


Figure 3-12. Longitudinal turbulence intensity profiles for a wide edge windward element orientation.

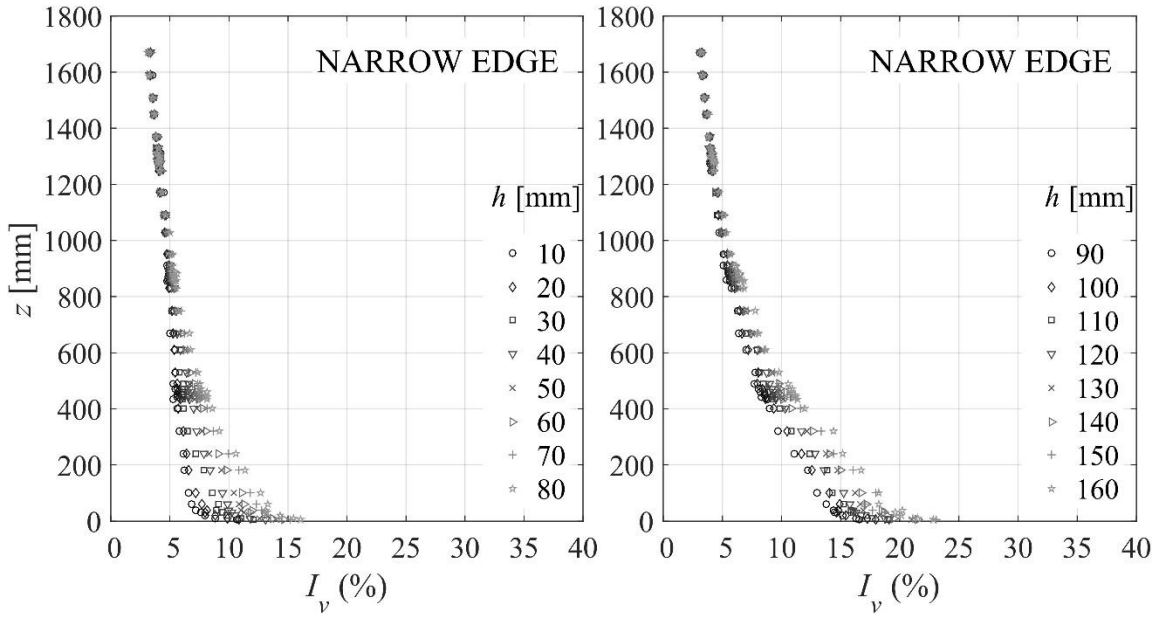


Figure 3-13. Lateral turbulence intensity profiles for a narrow edge windward element orientation.

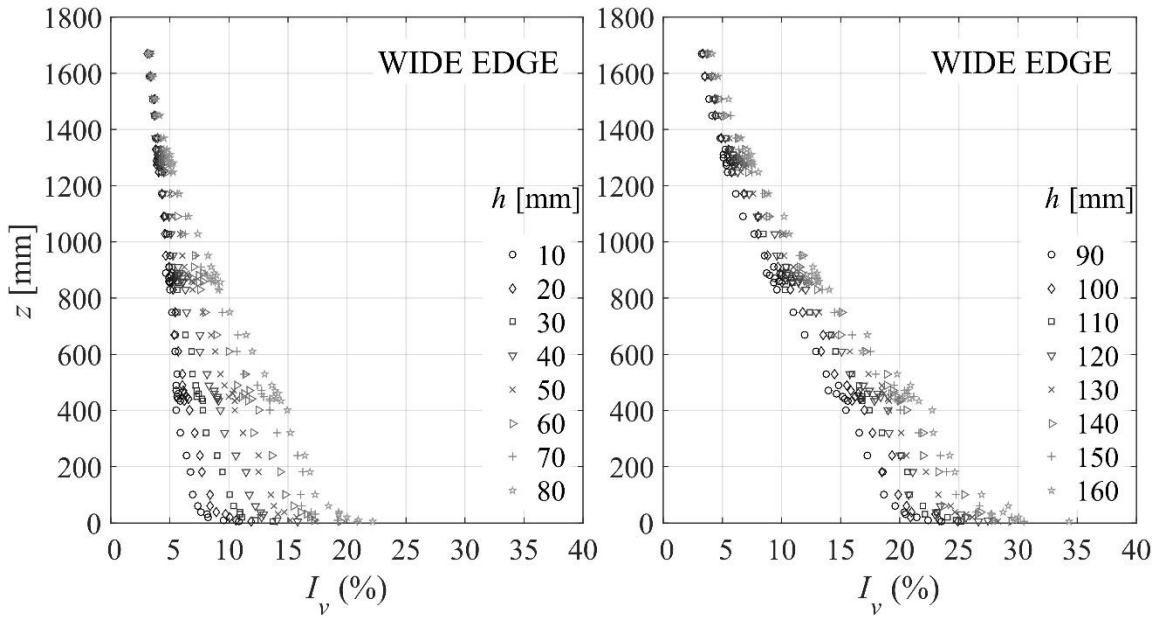


Figure 3-14. Lateral turbulence intensity profiles for a wide edge windward element orientation.

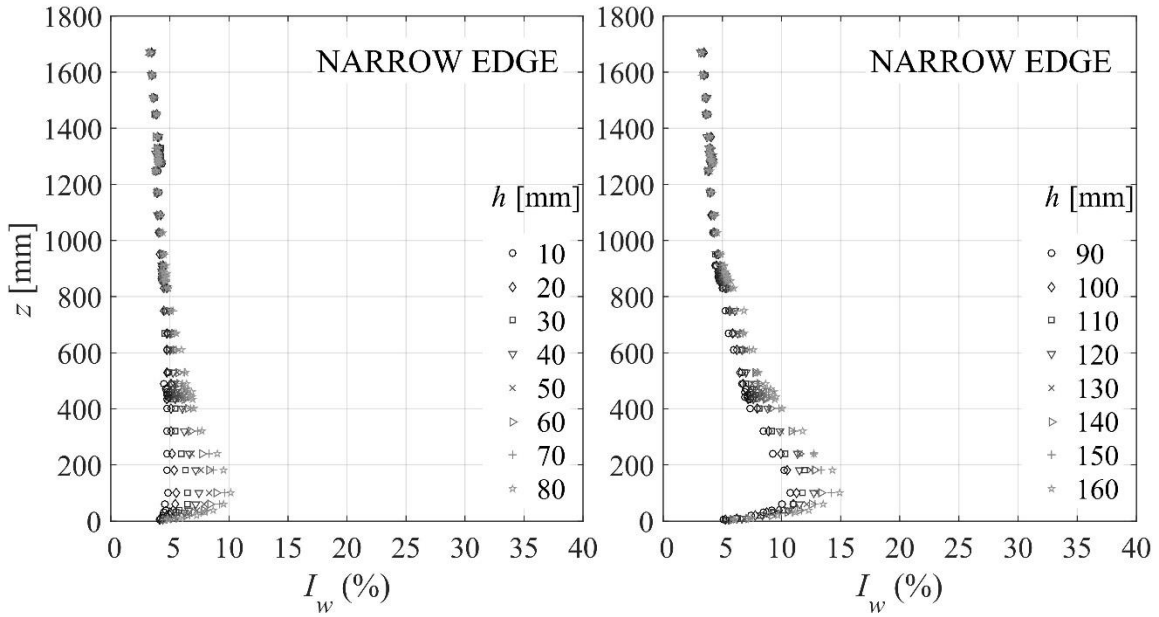


Figure 3-15. Vertical turbulence intensity profiles for a narrow edge windward element orientation.

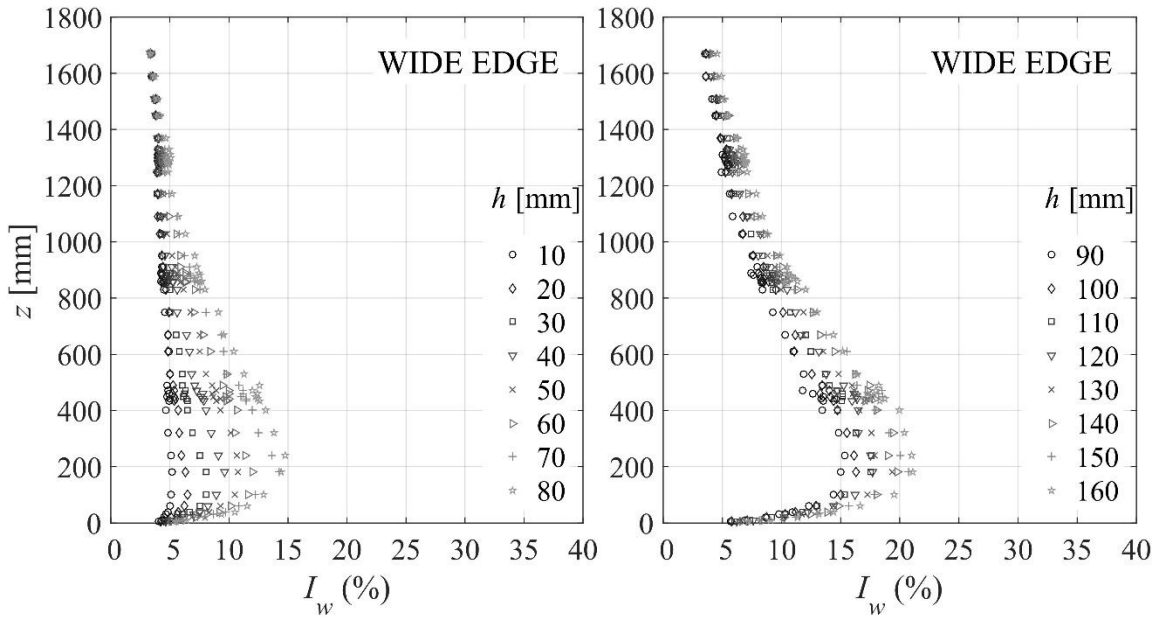


Figure 3-16. Vertical turbulence intensity profiles for a wide edge windward element orientation.

CHAPTER 4 SURFACE PRESSURES ON LOW-RISE BUILDINGS

This chapter presents the research design and subsequent findings from a comprehensive series of experiments in a large BLWT to investigate the variation of pressure coefficients with increasing surface roughness on low-rise buildings. Reduced geometric scale models of the Wind Engineering Research Field Laboratory (WERFL) experimental building (Tieleman et al., 1996) were subjected to a wide range of turbulent boundary layer flows, through precise adjustment of a computer control terrain generator called the Terraformer. The Terraformer allows rapid reconfiguration of upwind terrains ranging from marine to dense suburban exposures. Surface pressures on low-rise models were measured downwind of the Terraformer for a large series of upwind terrains, with particular attention to regions prone to flow separation.

Background

Significant research was conducted in the 1990s to assess uncertainties associated with wind tunnel tests of low-rise structures, and their accuracy in replicating full-scale surface pressures. Tieleman (1992) compared BLWT simulations with full-scaled pressure measurements from the Wind Engineering Research Field Laboratory (WERFL) experimental building at Texas Tech University. The study examines the importance of generating small-scale turbulence in the incident BLWT flow, to properly simulate peak full-scale suction pressures, present near the edges and roof corners. This and other studies (e.g., Tieleman and Reinhold, 1978; Hillier and Cherry, 1981; Gartshore, 1984) argued that adequate matching of the turbulence intensity takes priority over simulating

the shape of the mean velocity profiles, given that vortex formation on roof edges and corners are primarily controlled by the presence of the small-scale turbulence in the incident flow. In addition, several authors (e.g., Stathopoulos and Surry, 1983; Meecham et al., 1991; Lin et al., 1995) have recommended the use of larger models to better duplicate full-scale turbulence characteristics. However, most boundary layer tunnels are incapable of accommodating large low-rise models without causing excessive blockage effects (Krishna, 1995).

One governing factor for assessing wind loads on low-rise buildings is the effect of upwind terrain conditions. The shape and turbulence characteristics of the approaching boundary layer flow is strongly dependent on the level of surface roughness upwind of the building. The surface roughness is defined by the presence of obstructions on the earth's surface such as buildings and trees, which retards the along-wind flow. In rougher terrain, the longitudinal component of the mean velocity tends to slow down, while the along-wind turbulence intensity increases (i.e. the coefficient of variation). Wind load provisions, such as ASCE 7-10 (2010), introduce exposure coefficient profiles (Irwin, 2006) in design wind pressure calculations to account for the variation of wind velocity with terrain and elevation above ground. In the case of low-rise buildings, a single exposure coefficient is, in most cases, applied to design pressures acting on roof and walls. Therefore, it is implicitly assumed that the effect of terrain exposure on design pressures is the same for different regions on the building surface. However, studies (e.g., Tieleman et al., 1997; Pierre et al., 2005) have shown significant variation on peak pressure coefficients close to flow-separation regions, such as roof edges and corners, with increasing turbulence.

The bulk of wind tunnel studies assessing extreme surface pressures on buildings have been limited to two terrain conditions, namely open and suburban (e.g., Hunt, 1982, Pierre et al., 2005). In boundary layer wind tunnels, simulation of these two terrains is typically attained by manual modification of upwind terrain via mixing devices—e.g., vortex generators, roughness grid, barriers—until aerodynamic parameters, such as roughness length, closely match predefined values from wind load provisions. This study is the first of its kind to systematically characterize both the flow and pressure coefficient distribution on building models.

Simulation of Approach Flow

BLWT experiments were conducted at the University of Florida (UF) Natural Hazard Engineering Research Infrastructure (NHERI) Experimental Facility. The BLWT at UF is a low-speed open circuit tunnel with dimensions of 6 m W x 3 m H x 38 m L (Chapter 4). Simulation of terrain roughness is performed via the Terraformer, an automated roughness element grid that rapidly reconfigures the height and orientation of 1116 roughness elements in a 62 X 18 grid to achieve desired upwind terrain conditions. The grid extends nominally 18.3 m along the length of the tunnel. Dimensions of the elements are 5 cm by 10 cm, and they are spaced 30 cm apart in a staggered pattern. Height and orientation can be varied from 0-160 mm and 0-360 degrees, respectively. The previous chapter of this document describes the components of UF's BLWT and presents results from an extensive series of boundary layer flow measurements at the test section of the tunnel.

Low-Rise Building Models

Pressure tests were conducted on three rigid building models of Wind Engineering Research Field Laboratory (WERFL) experimental building with geometric scales of 1:20, 1:30, and 1:50. Multiple model scales were tested to investigate the effects of reattachment regions. The three models are identical but scale by a constant geometric multiplier. The models were instrumented with 266 pressure taps on the four walls and roof. The tap location follows the same layout as UWO (Pierre et al., 2005), however 60 additional pressure taps were added on the roof of the model (Figure 4-1). The roof pitch is 1:48 for all models. The models were placed at the center of the test section.

Pressure Measurements

Instrumentation

Time series of differential pressures acting on each tap were measured using eight 64Px ZOC33 electronic pressure scanning modules (64Px ZOC33, Scanivalve Corp.). Each module consists of 64 channels, and are housed in a rugged stainless steel thermal control unit (TCU), along with an Ethernet remote analog to digital (A/D) module (E-RAD 4000, Scanivalve Corp.). The TCU can operate in temperatures ranging from - 45°C up to 65°C. Each ZOC33 module incorporates 64 individual silicon pressure sensors, calibration valving, a high speed multiplexer (45 kHz), and an instrumentation amplifier.

Clear urethane tubing (URTH-063, Scanivalve Corp.) were used to connect each pressure tap to a corresponding channel in a pressure scanning module. The tubes have an outer diameter of 0.086 inches and inner diameter of 0.054 inches. The length of the tube was 48 in for all taps and model scales.

The use of tubing systems to connect pressure taps to the pressure scanners creates distortion of the pressure fluctuations—i.e., $p(t)$ —resulting from resonance and damping effects in the tubing system (Irwin et al., 1979). The distortion depends on several factors including: (1) tube length and diameter, (2) geometry of the pressure scanner internal passageways, (3) and on the transducer internal volume. To correct for distortion effects, measured pressures were digitally filtered using tubing system transfer functions (Figure 4-2) for several tube lengths. The frequency response function for tubing of a given length is obtained by generating a random input pressure signal containing all of the desired frequencies (i.e., a pink noise signal). The pressure signal is measured at two taps, one connected to a pressure transducer through a minimal length tube (< 6 inches) and the other through a tube of a specific length for which distortion effects need to be corrected. The ratio of the FFTs of the two signals provides the frequency response function, which essentially contains factors to adjust the amplitude and phase of the distorted signal at specific frequencies from 0 to half of the sampling frequency, known as the Nyquist frequency.

Pressure Coefficients

External pressure coefficients for all experiments were calculated as the ratio of the differential pressure and the velocity (dynamic) pressure at model eave height:

(4-1)

$$C_p(t) = \frac{p(t) - p_0}{\frac{1}{2} \rho \bar{U}_{ref}^2}$$

where $p(t)$ is the (absolute) pressure measured, p_0 is the reference (static) pressure, ρ is the air density, and \bar{U}_{ref} is the mean longitudinal velocity at eave height. Normalization of surface pressures to the velocity pressure at eave height is common practice in pressure tests of generic low-rise models (e.g., Uematsu and Isyumov, 1999; Pierre et al., 2005). Static reference pressures (p_0) will be taken from the static port of the Pitot tube, ensuring stable measurements with negligible fluctuations. Air density (ρ) will be estimated based on the air temperature, barometric pressures, and relative humidity measured during each test.

During testing, \bar{U}_{ref} were measured indirectly based on Pitot tube measurements. A conversion factor was used to relate the mean wind speed at Pitot tube height to the model eave height (Figure 4-3). Direct measurement of \bar{U}_{ref} would require placing a velocity probe (i.e., Cobra Probe) in close proximity to the model, causing flow distortion and adverse effects of pressure measurements in the model. Additionally, distortion in the flow due to blockage effects (ASCE-SEI 49-12) are non-existing given the large cross-section of the tunnel relative to the model dimensions.

Peak Pressures

Extreme value analysis was applied to provide a more reliable estimate of peak surface pressures (Lieblein, 1974). A Fisher-Tippett Type I—also known as Gumbel—extreme-value distribution has proven to be a useful method for assessing peak pressures in building studies (Mayne and Cook, 1979). The

Gumbel fit models the peak pressures well for a modest number of peak events—i.e., less than 100 (Holmes and Cochran, 2003)—for a positive or negative pressure regime. The procedure for estimating peak pressures can be summarized as follows: (1) Peak (maximum or minimum) C_p values from N non-overlapping segments are obtained from pressure time series. (2) Peak values are sorted in ascending order, and allocated a Gumbel plotting position given by $i/(N + 1)$, where i is the order. (3) The plotting parameter is transformed into a reduced variate: $y_r = -\ln\{-\ln[i/(N + 1)]\}$. (4) \check{C}_p values are plotted against y_r , and a linear regression fit is performed. (5) Mode (u) and shape ($1/a$) parameters are obtained from the fit. (6) Peak estimates for a given probability of exceedance F_{exc} can be obtained from the Gumbel cumulative distribution function: $F(x) = \exp[-\exp(-x - u)/a]$, where x is the random variable—i.e., peak C_p .

Experimental Design

Three models of the WERFL building were immerse in 33 turbulent flow fields. The approach flow was varied by changing the configuration of the roughness element grid—i.e., Terraformer—upwind of the model. Two element orientations were be considered, namely wide and narrow edge windward. Roughness elements were elevated from 0-160 mm using increments of 10 mm, thus generating 16 upwind terrain conditions for each element orientation—for a total of 33 terrains.

Three wind angles were considered for each terrain configuration and model scale, namely 0, 45, and 90 degrees. Figure 4-4 shows three wind tunnel tests from the 1:30 WERFL model. The figure provides a representative case of

the three model orientations: (1) long building dimension parallel to the wind—0°, (2) cornering wind—45°, and (3) short building dimension parallel to the wind—90°. From herein, the term “test” will be defined as a single experiment for a particular (1) terrain configuration, (2) model scale, and (3) wind orientation.

Sampling rate will be selected according to reduced frequency relation:

$$\left(\frac{fL}{U}\right)_M = \left(\frac{fL}{U}\right)_{FS} \quad (4-5)$$

where f is the sampling rate, L is the characteristic length, and U is the reference wind velocity for model (M) and full-scale (FS), respectively. For all the tests, the mean reference wind velocity—at Pitot tube height (Figure 4-3)—was approximately 15 m/s. The characteristic length of the model is directly proportional to the geometric scale of the model.

The sampling period of each test must be sufficiently long to provide stable estimates of the statistics of surface pressures—mean and root-mean square (RMS). Additionally, peak pressures must provide a representative estimate of full-scale intervals of approximately 3600 seconds, because these are used in combination with the statistics of hourly mean wind speeds for calculation of full-scale peak pressures (Davenport, 2007). Table 4-1 summarizes the selected testing parameters for the three model scales.

Results and Discussion

Validation of Pressure Measurements

Pressure coefficients were compared to aerodynamic tests conducted at the University of Western Ontario (UWO). Two terrains were examined on UWO’s 1:100 WERFL model tests, namely, open ($z_0 = 0.01$ m) and sparse

suburban ($z_0 = 0.087$). The measured turbulence intensity at eave height for the two exposures were approximately $I_u = 14$ and 22%, for open and sparse suburban, respectively. Figure 4-5 shows a comparison of mean pressure coefficients between the 1:100 UWO model and the three models tested in this study. A roughness element configuration was selected to closely match the turbulence levels of UWO (22%). Data points in Figures 4-5 correspond to mean pressure coefficients from UWO's 206 pressure taps. The three models scales—1:20, 1:30, and 1:50—show reasonable agreements to surface pressures from UWO. However, most of the data points are below the 45 line, indicating that mean pressures from this study were slightly larger than the tests conducted at UWO. Figure 4-6 includes representative peak (minimum) pressure coefficients corresponding to a 78% probability of non-exceedance. The data points in the figure are more scattered compared to mean pressures. The bulk of the experiments showed acceptable agreement between UWO and UFL WERFL data when turbulence levels at eave height were matched.

Illustrative power spectral densities of pressure coefficient time histories for the 1:20 WERFL model (45 degree angle of attack) are depicted in Figure 4-7. The pressure signal corresponds to Tap 216, located at the roof corner closest to the main wind direction (Figure 4-1). The signal was low-pass filtered at 150 Hz. A roughness element height was selected for a narrow (left subplot) and wide (right subplot) element orientation to approximately match the longitudinal turbulence at eave height (I_u). Agreements is observed between UWO and UFL data.

Spatial Distribution of Surface Pressures

Contour subplots of mean pressures ($C_{p,mean}$) from four BLWT tests are shown in Figure 4-8 for the 1:20 WERFL model and a wind direction parallel to the long building dimension ($\alpha = 0^\circ$). The four subplots correspond to turbulence intensities at eave height of 10.4, 18.7, 25.7, and 27.7%, all achieved from a wide edge windward element orientation. Positive mean pressures of 0.5 are observed near the centroid of the windward wall—stagnation point—for turbulence levels of 10.4% and 18.7% (top two subplots). Higher turbulence intensities show mean C_p values around 0.75 (bottom subplots). Roof taps close to the windward wall show mean suction (negative) of approximately -1.2 for $h/H = 0.10$ and 0.30 , and -1.75 for $h/H = 0.56$ and 0.71 .

Figure 4-9 illustrates the spatial distribution of root-mean squares (RMS) of pressures for the 1:50 WERFL model and a wind direction perpendicular to the long building dimension ($\alpha = 90^\circ$). It is evident from the four subplots that the two roof corners facing the main wind direction experience the highest RMS values. Maximum RMS pressures range from 1.2 for $I_u = 11.7\%$ to 2.2 for $I_u = 27.3\%$.

Maps of peak pressure coefficients from four representative BLWT tests are presented in Figure 4-10 for the 1:30 WERFL model and a cornering wind angle of 45° . Peak pressure values at the roof corner closest to the main wind direction were around -6 for $h/H = 0.15$, while $h/H = 1.06$ produced peak pressures exceeding -14.

Figures 4-11, 4-12, and 4-13 show the distribution of mean pressures along a line of taps in the long building dimension for the 1:20, 1:30, and 1:50 WERFL models, respectively. The wind direction is along the tap line ($\alpha = 0^\circ$).

Each figure includes 16 curves, one for each element height (h) oriented in the wide edge windward element orientation. Turbulence intensity values at eave height (H) for each elements height are included in the legend of the figure. For the 1:20 model (Figure 4-11), mean pressures vary from -0.9 to -1.3 near the leading edge of the roof (i.e., $x/H = 0$) for turbulence levels between 8.6-29.1%. Comparable ranges of mean pressures at $x/H = 0$ can be observed for the 1:30 model (Figure 4-12). However, slightly lower values of mean pressures at $x/H = 0$ were found for the 1:50 WERFL model. This is depicted in Figure 4-13.

Mean pressures along a line of taps perpendicular to the ridgeline of the roof, for $\alpha = 90^\circ$, are shown in Figures 4-14, 4-15, and 4-16 for the three model scales, and a wide edge element orientation. For the 1:20 and 1:30 models (Figures 4-14 and 4-15), mean pressures at $x/H = 0$ range from -1.1 to -1.5. The 1:50 model shows slightly lower values ranging from -1.0 to -1.2 near the leading edge of the roof.

Representative profiles of peak pressures along a line of roof taps—parallel to the long building dimension—for the three WERFL models are displayed in Figures 4-17, 4-18, and 4-19, for $\alpha = 0^\circ$. A large spread in peak pressures near the leading edge of the roof is evident on the three figures. However, the spread for the 1:50 WERFL model is small in relation to the other two models. Variation in peak pressures were between -3 and -9 for the 1:20 and 1:30 models, while peak pressures only ranged from -2.5 to -6 at $x/H = 0$ for the 1:50 model.

Characterizing Upwind Terrain and Model Scale Comparison

Figure 4-20 includes peak pressures—on all 266 pressure taps—from the 1:30 and 1:50 WERFL (UFL) models plotted against the 1:20 model. The top subplot displays pressures from selected upwind terrain configurations matching turbulence intensities (at eave height) representative of open exposure ($I_u \sim 14\%$). The bottom subplot includes pressures corresponding to roughness array configurations matching equivalent full-scale roughness lengths z_0 for open country exposure—BLWT roughness lengths were geometrically scaled based on the model scale. ASCE 7-10 (2010) provides a range of roughness lengths for open terrain ranging from $z_0 = 0.01\text{-}0.15$ m. Comparable (peak) pressures are observed for the two subplots in Figure 4-20. In contrast, Figure 4-21 shows significant differences in peak pressures for suburban simulation. Larger peak values (-6 to -8) are detected, for $\alpha = 0^\circ$, when reconfiguring the Terraformer to attain the required turbulence levels at eave height. Nevertheless, both suburban and open simulation, show consistent agreement between the three model scales, when the turbulence intensity was matched at the eave of the model.

Figure 4-22 provides a comparison of two simulations of open terrain, achieved using a narrow (top subplot) and wide (bottom subplot) edge windward element orientation. Roughness element heights of 30 mm and 60 mm were selected for the wide and narrow subplots, respectively. The resulting turbulence intensities (at eave height) for the three model scales are included. The two upwind terrains appear to generate comparable (peak) pressures for the considered wind direction.

Summary

A series of experiments was conducted in a large BLWT to investigate the effects of envelop pressures on low-rise buildings with increasing surface roughness. Models of the WERFL experimental building were immersed in 33 of turbulent boundary layer flows via precise regulation of a computer control terrain generator.

BLWT pressure tests were compared to aerodynamic experiments of a 1:100 model of the WERFL building conducted at UWO. In general, good agreement was found between UWO and UFL WERFL pressure measurements when matching the turbulence levels at eave height. Furthermore, the 1:50 model consistently showed the best match with UWO's pressure data. Experiments revealed the dependency of extreme (minimum) pressure coefficients with increasing surface roughness. Peak pressures near the leading edge of the roof appeared to vary linearly with increasing turbulence levels at eave height. The trend was more pronounced in the 1:20 and 1:30 models. Only slight variations in the mean pressures were observed with increasing turbulence levels.

Table 4-1. WERFL testing parameters

Model Scale	1:20	1:30	1:50
Sampling period, T	300 s	180 s	120 s
Sampling rate, f		625 Hz	
Wind direction, α		0°, 45°, and 90°	
Mean reference wind speed (pitot), \bar{U}_{ref}		15.3 m/s	
Eave height, h_{eave} (mm)	198	132	80
Number of pressure taps		266	
Roof slope		1:48	

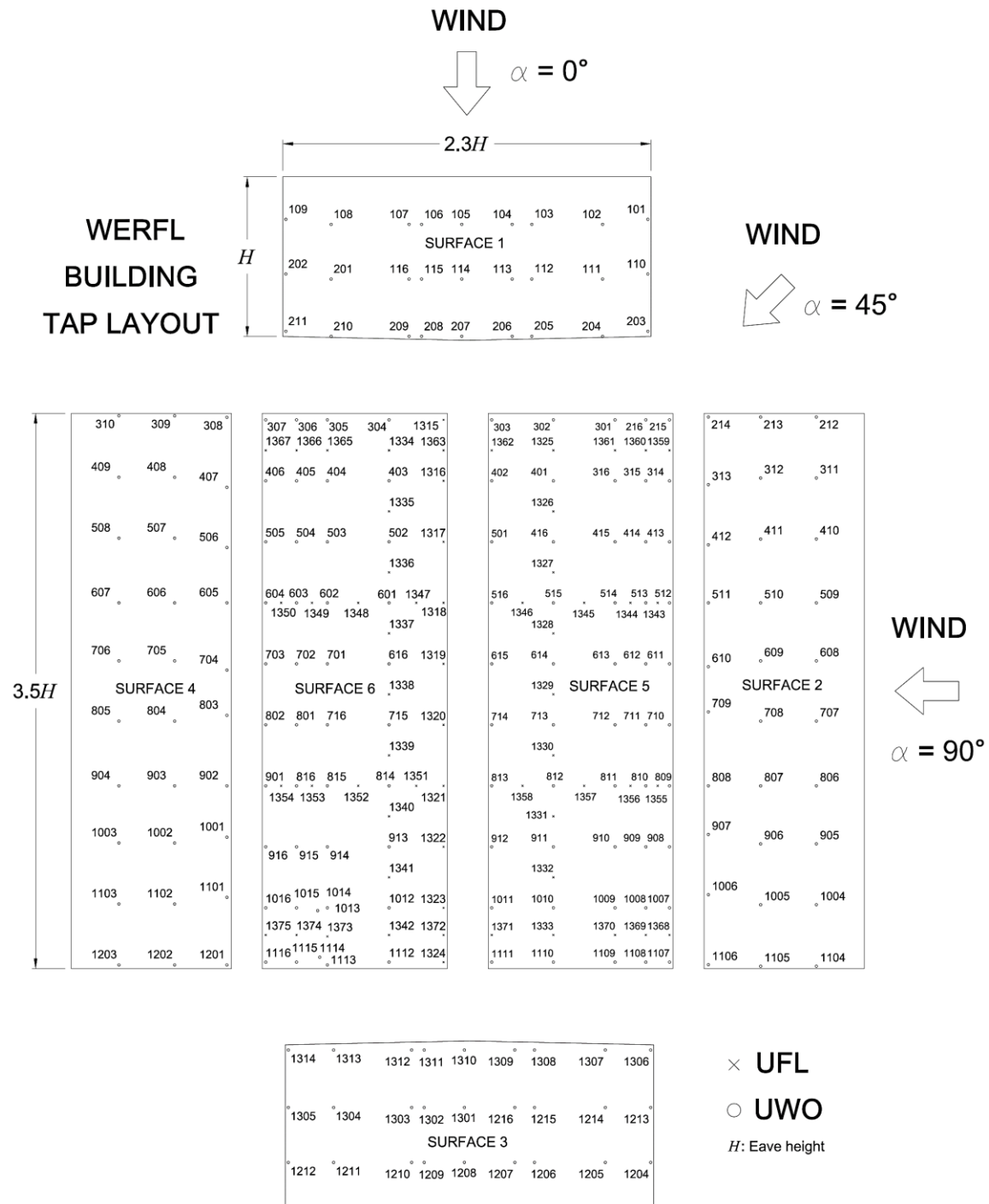


Figure 4-1. Pressure tap layout for 1:20, 1:30, and 1:50 WERFL building models.

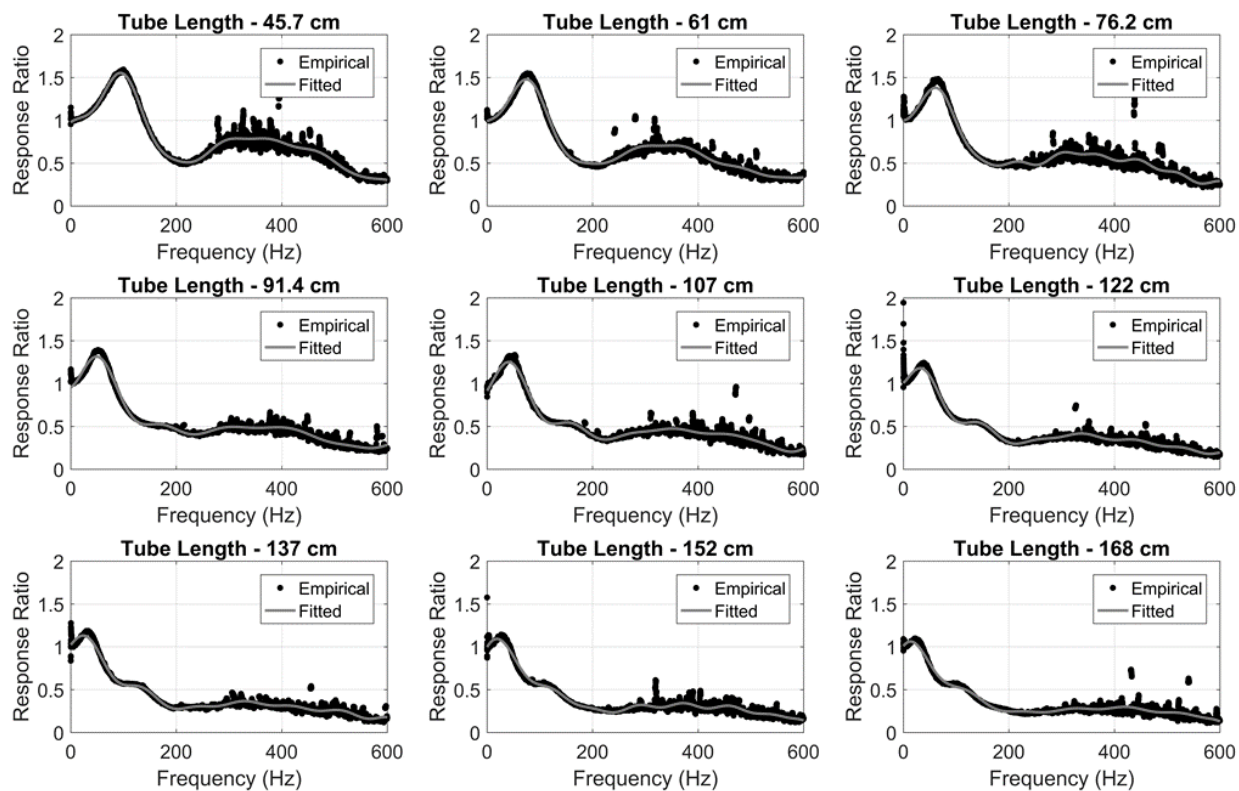


Figure 4-2. Measured and fitted response amplitudes up to a frequency of 600 Hz (Courtesy of Dr. David Roueche).

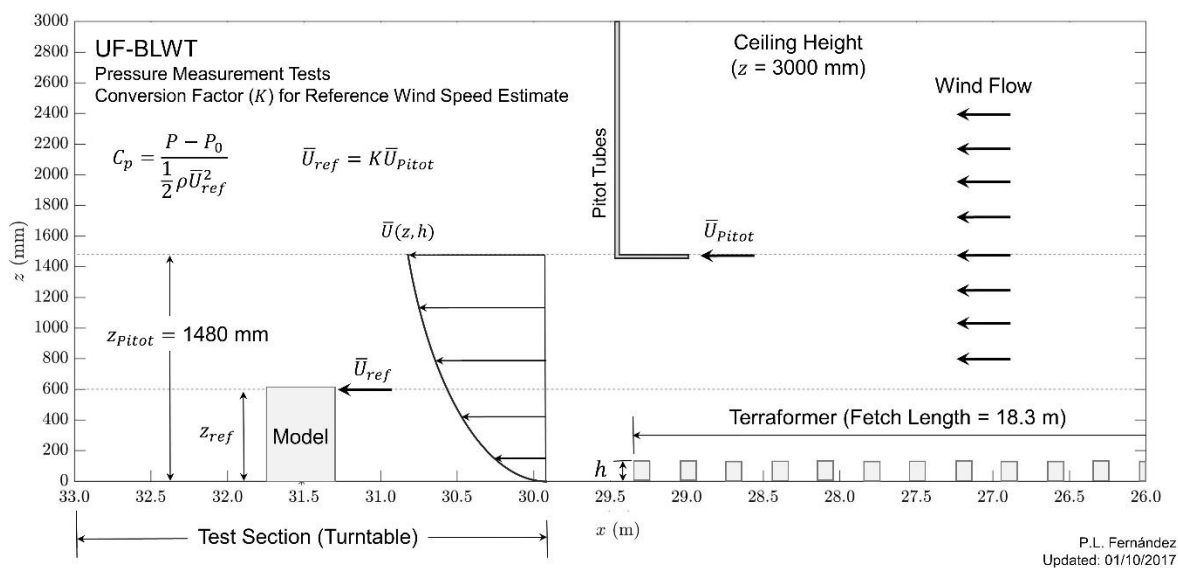


Figure 4-3. Schematic diagram of BLWT physical arrangement near the test section for pressure tests.

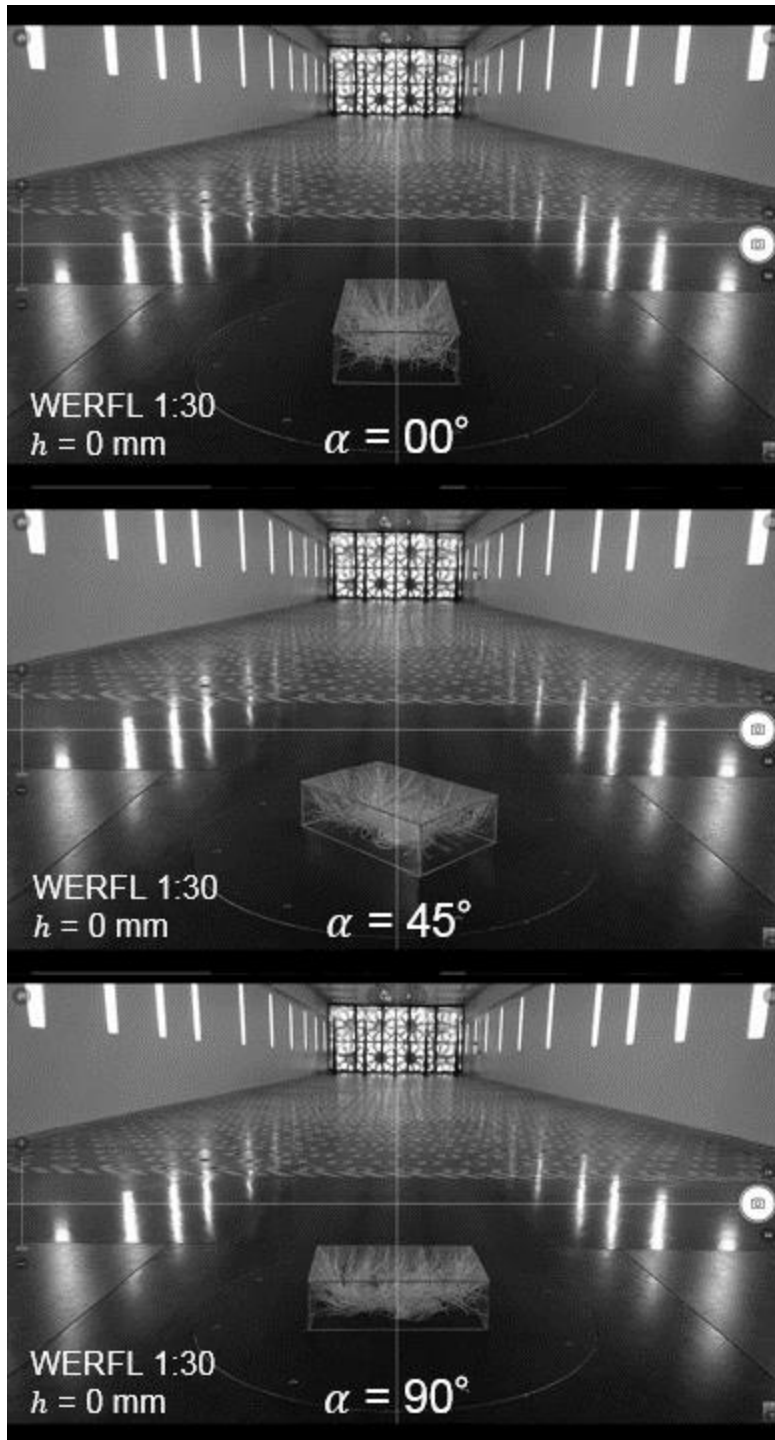


Figure 4-4. Aerodynamic test of 1:30 WERFL building model at UF's BLWT (Photos courtesy of author).

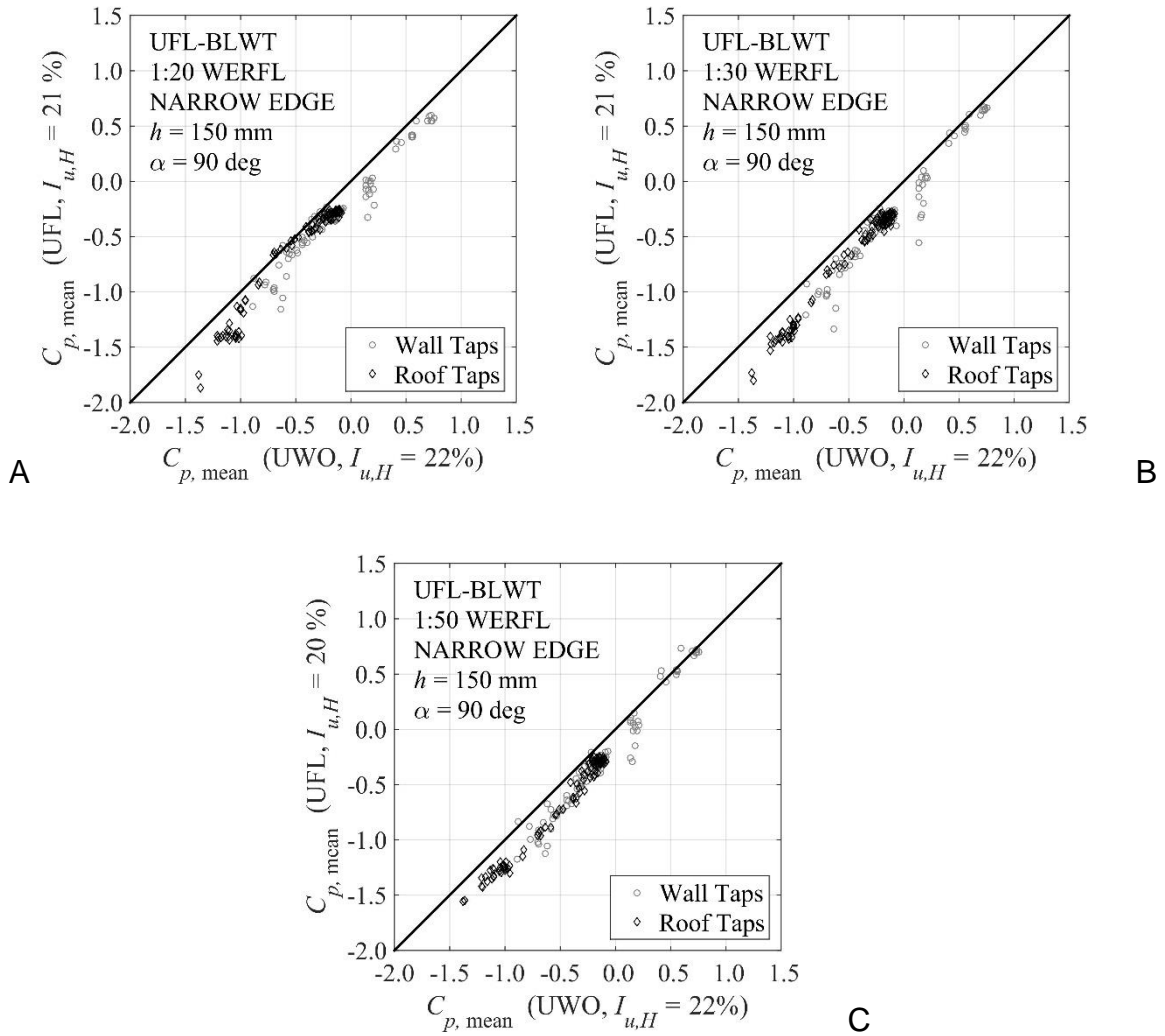


Figure 4-5. Comparison of mean pressure coefficients for the A) 1:20, B) 1:30, and C) 1:50 WERFL models (Narrow edge, $h = 150 \text{ mm}$, $\alpha = 90^\circ$).

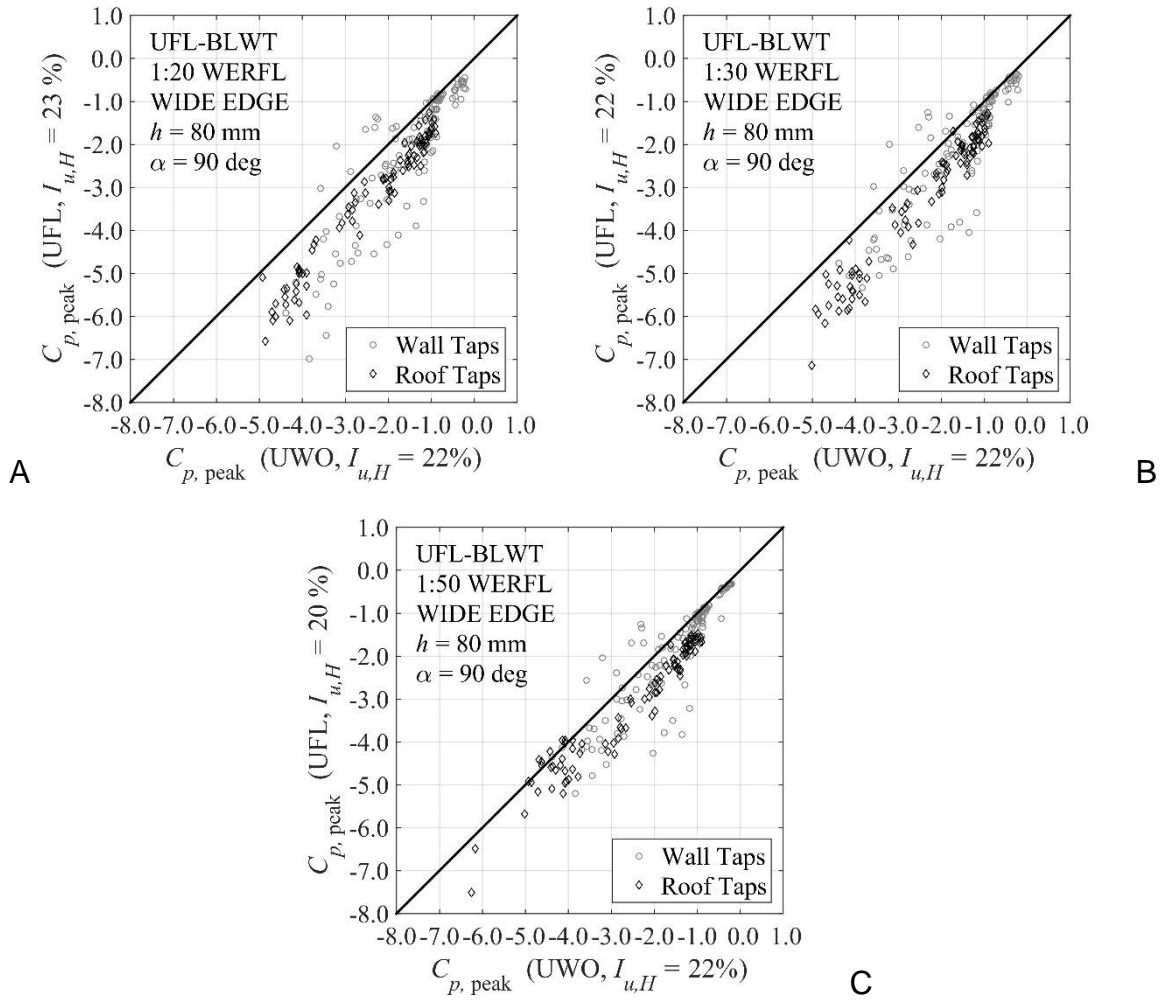


Figure 4-6. Comparison of peak pressure coefficients for the A) 1:20, B) 1:30, and C) 1:50 WERFL models (Wide edge, $h = 80 \text{ mm}$, $\alpha = 90^\circ$).

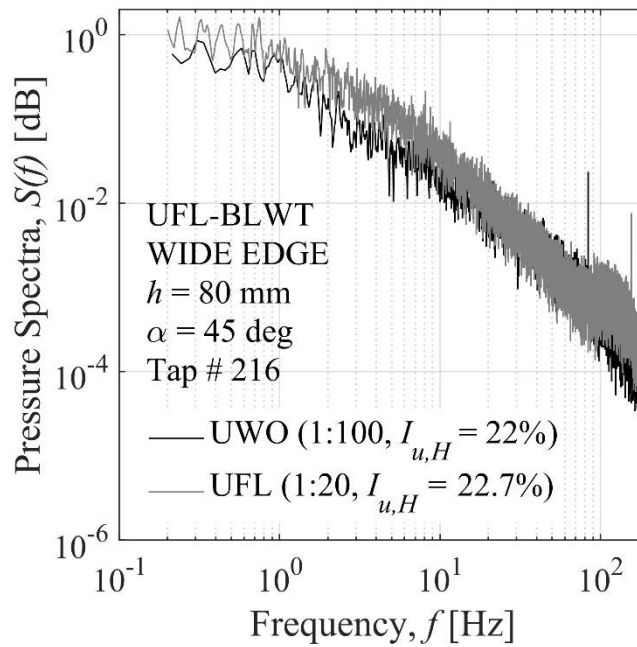
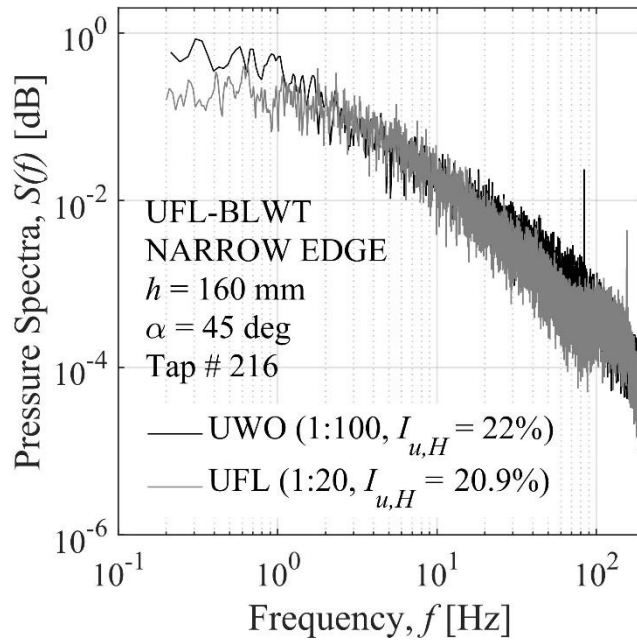


Figure 4-7. Pressure spectra comparison of Tap 216 (located near the roof corner closest to the approach flow) for the 1:20 WERFL model.

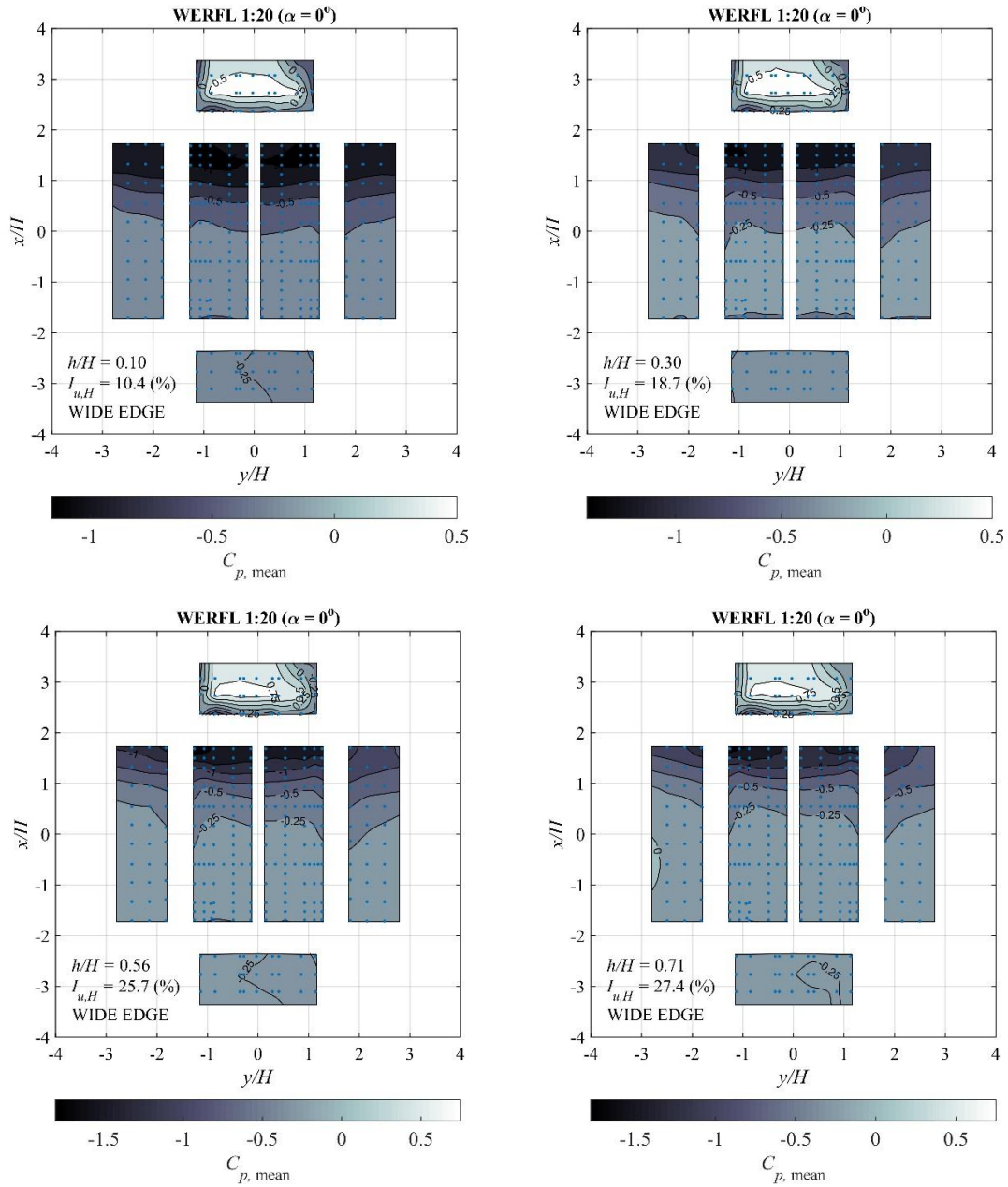


Figure 4-8. Distribution of mean pressure coefficients for the 1:20 WERFL model (Wide edge, $\alpha = 0^\circ$).

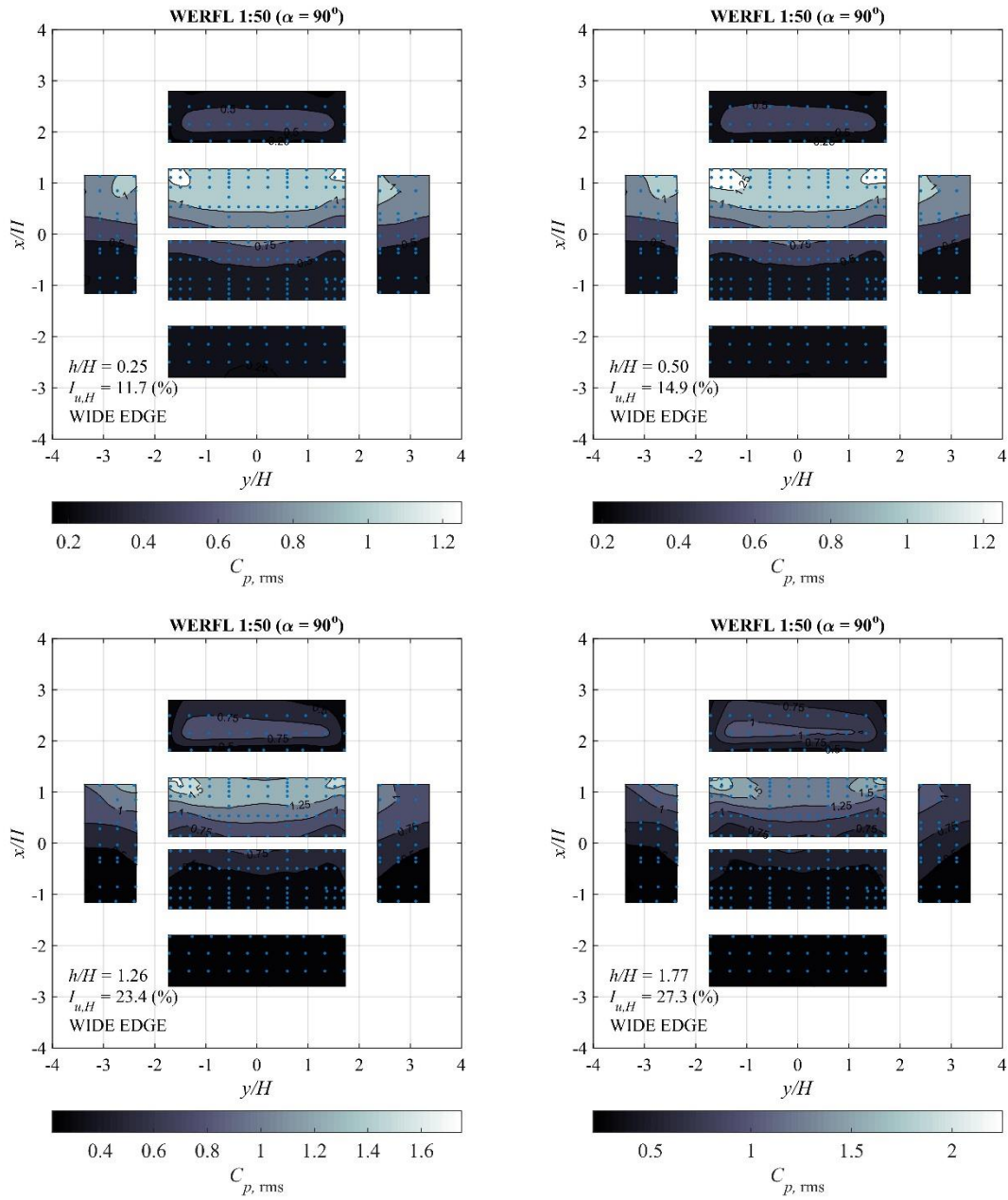


Figure 4-9. Distribution of RMS pressure coefficients for the 1:50 WERFL model (Wide edge, $\alpha = 90^\circ$).

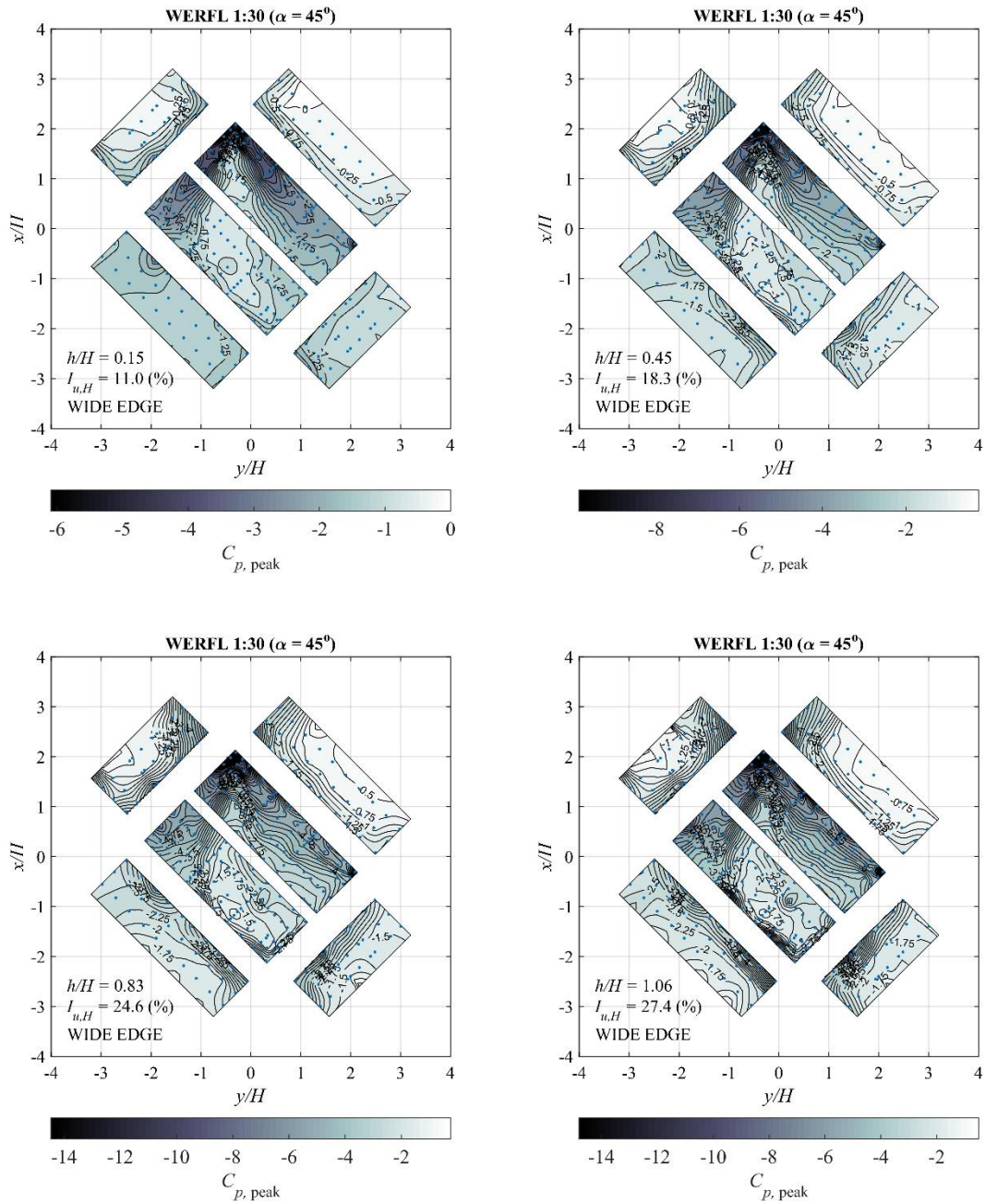


Figure 4-10. Distribution of peak pressure coefficients for the 1:30 WERFL model (Wide edge, $\alpha = 45^\circ$).

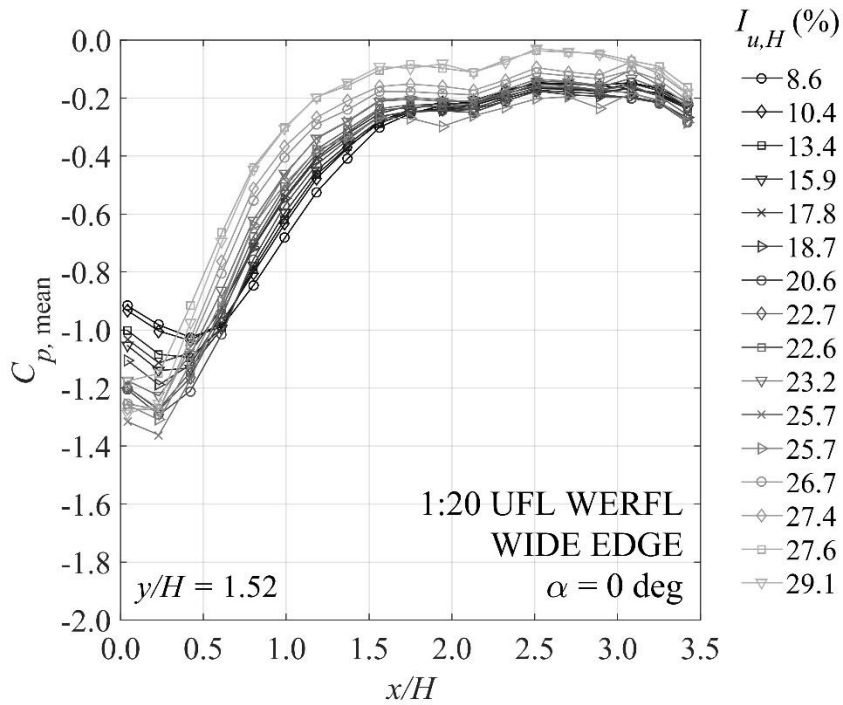


Figure 4-11. Distribution of mean pressures along a line of taps (parallel to the long building dimension) for the (a) 1:20 WERFL model (Wide edge, $\alpha = 0^\circ$).

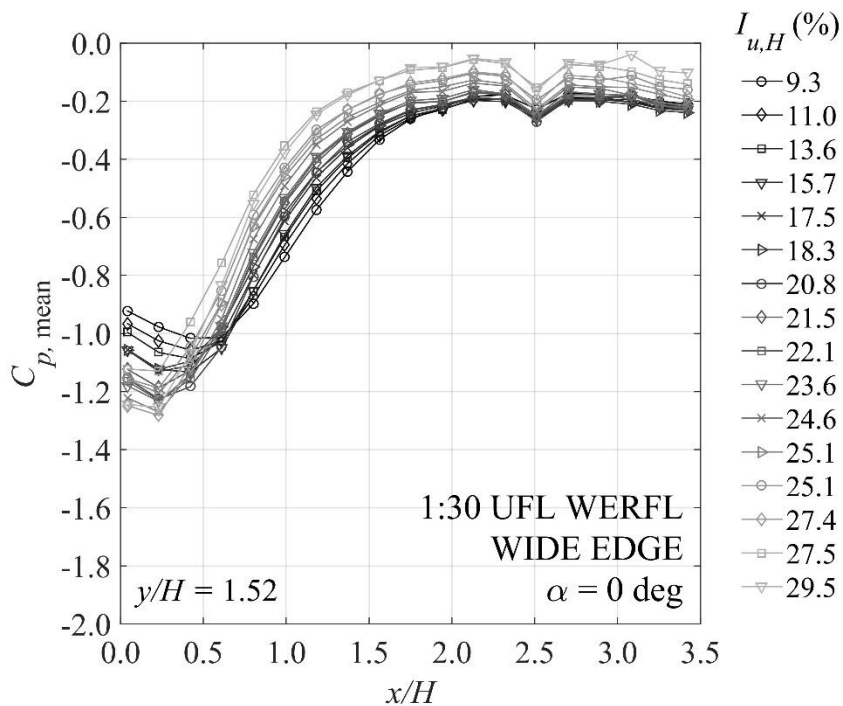


Figure 4-12. Distribution of mean pressures along a line of taps (parallel to the long building dimension) for the 1:30 WERFL model (Wide edge, $\alpha = 0^\circ$).

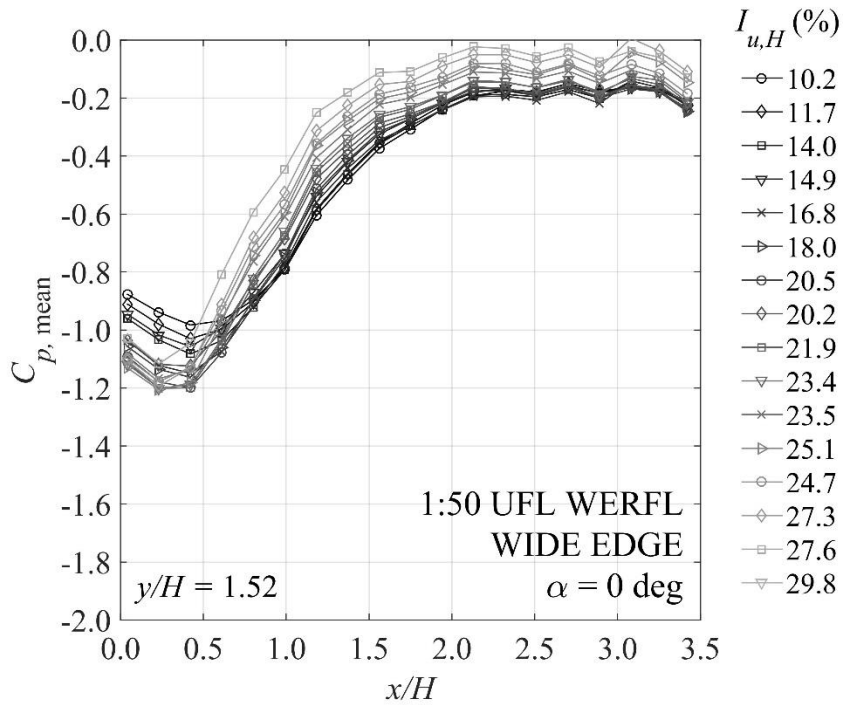


Figure 4-13. Distribution of mean pressures along a line of taps (parallel to the long building dimension) for the 1:50 WERFL model (Wide edge, $\alpha = 0^\circ$).

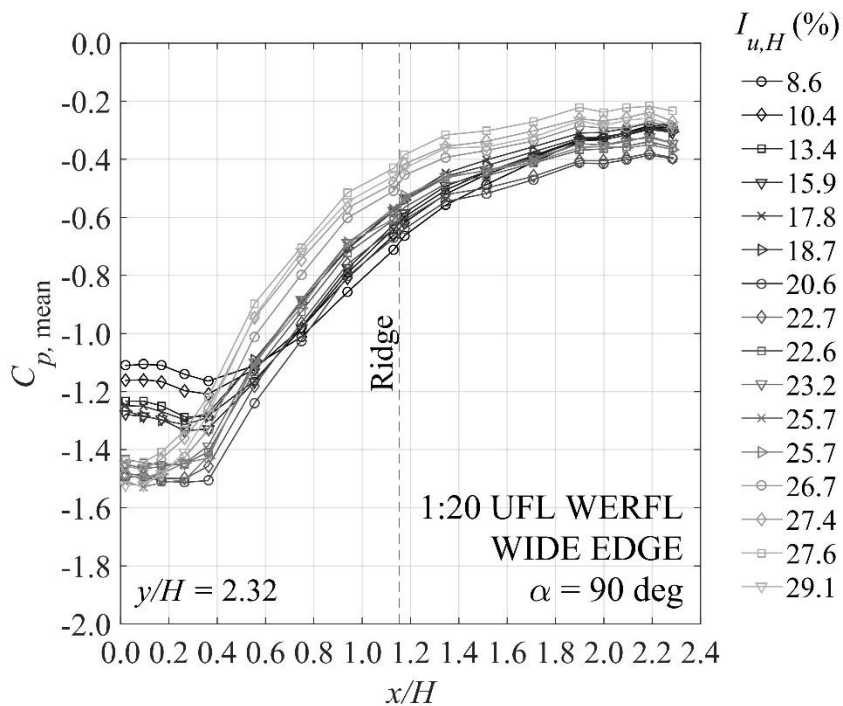


Figure 4-14. Distribution of mean pressures along a line of taps (perpendicular to the long building dimension) for the 1:20 WERFL model (Wide edge, $\alpha = 90^\circ$).

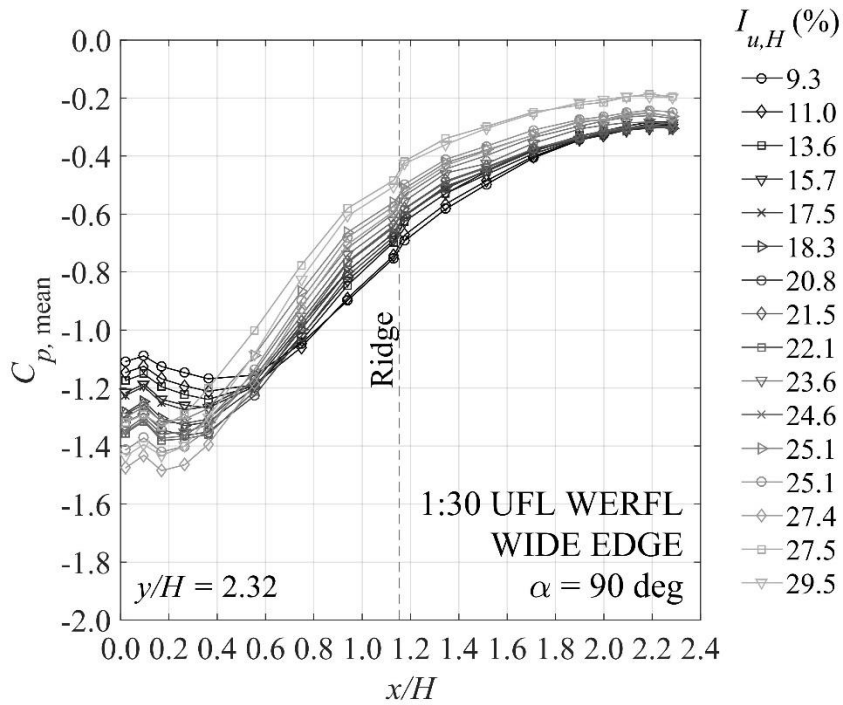


Figure 4-15. Distribution of mean pressures along a line of taps (perpendicular to the long building dimension) for the 1:30 WERFL model (Wide edge, $\alpha = 90^\circ$).

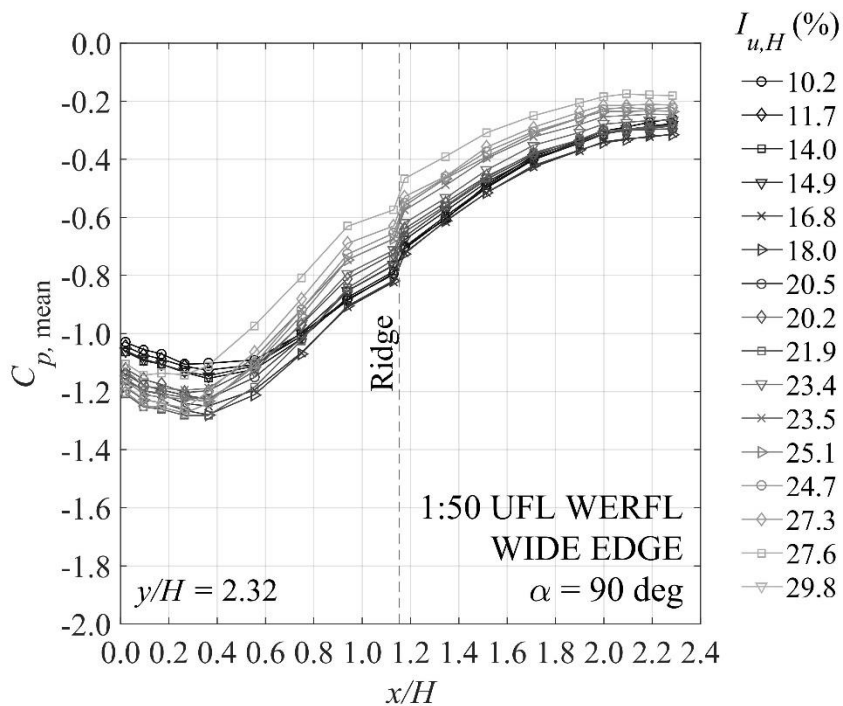


Figure 4-16. Distribution of mean pressures along a line of taps (perpendicular to the long building dimension) for the 1:50 WERFL model (Wide edge, $\alpha = 90^\circ$).

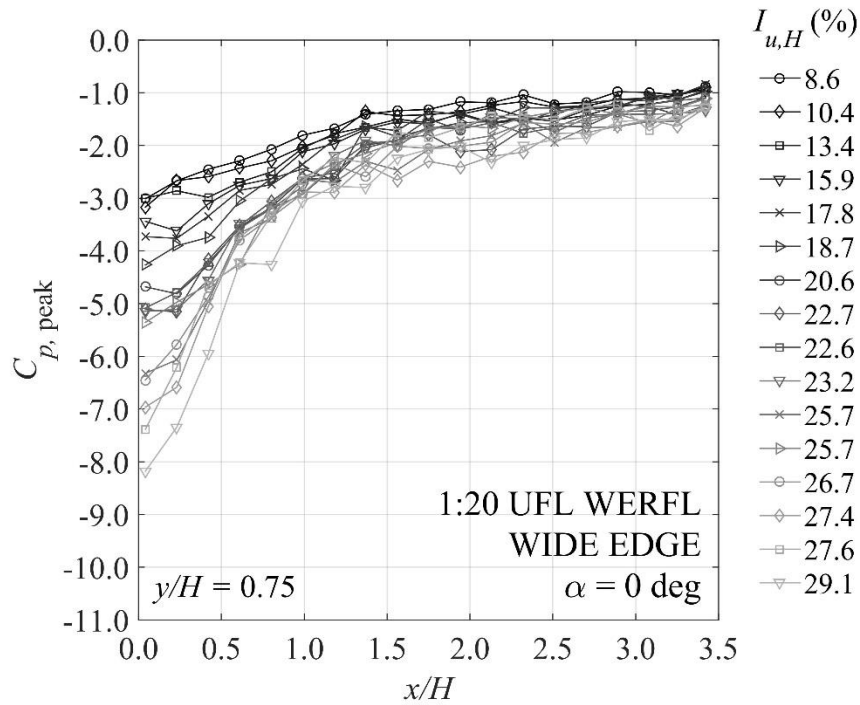


Figure 4-17. Distribution of peak pressures along a line of taps (parallel to the long building dimension) for the 1:20 WERFL model (Wide edge, $\alpha = 0^\circ$).

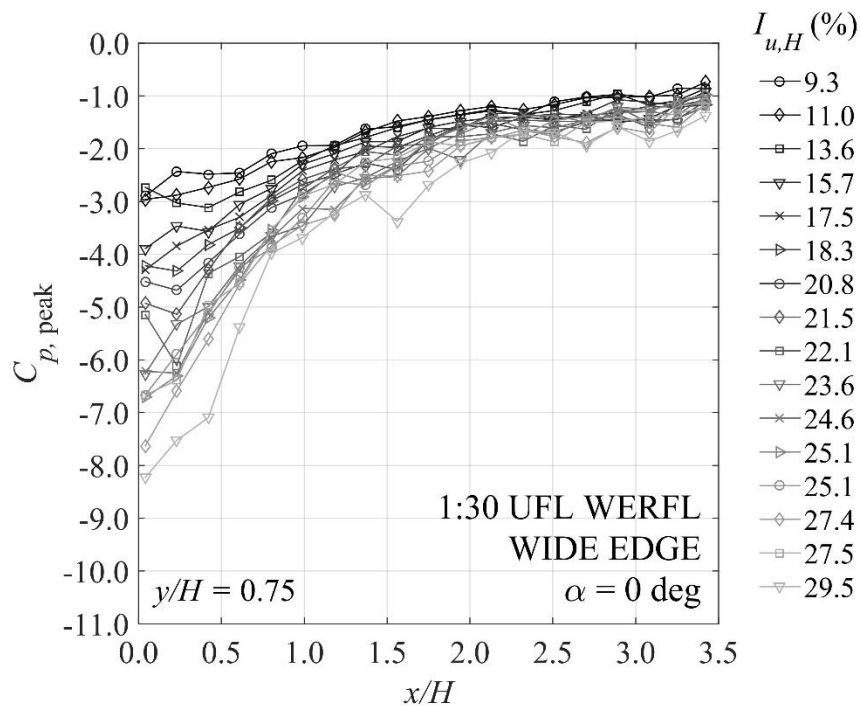


Figure 4-18. Distribution of peak pressures along a line of taps (parallel to the long building dimension) for the 1:30 WERFL model (Wide edge, $\alpha = 0^\circ$).

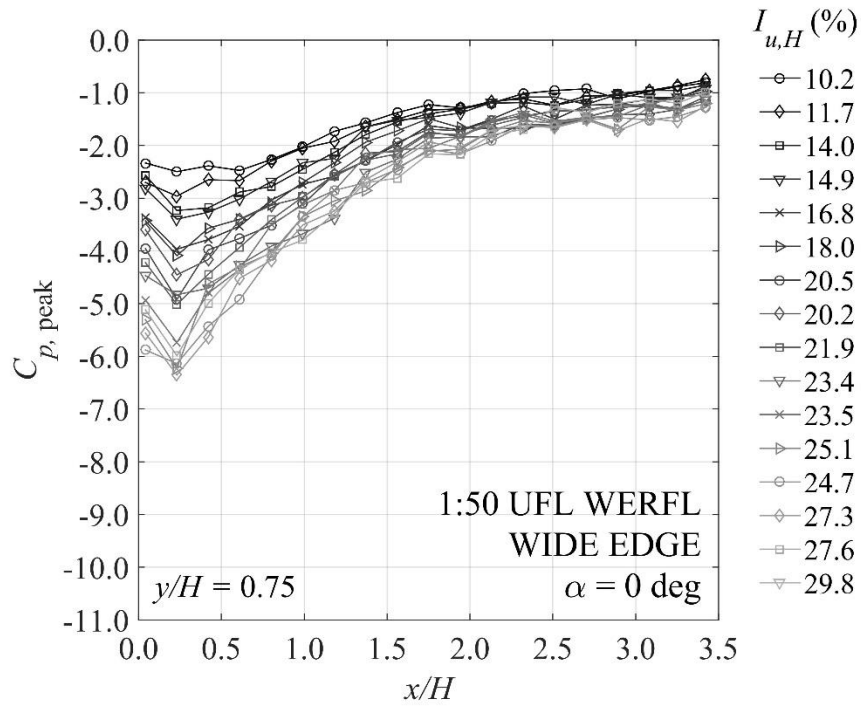
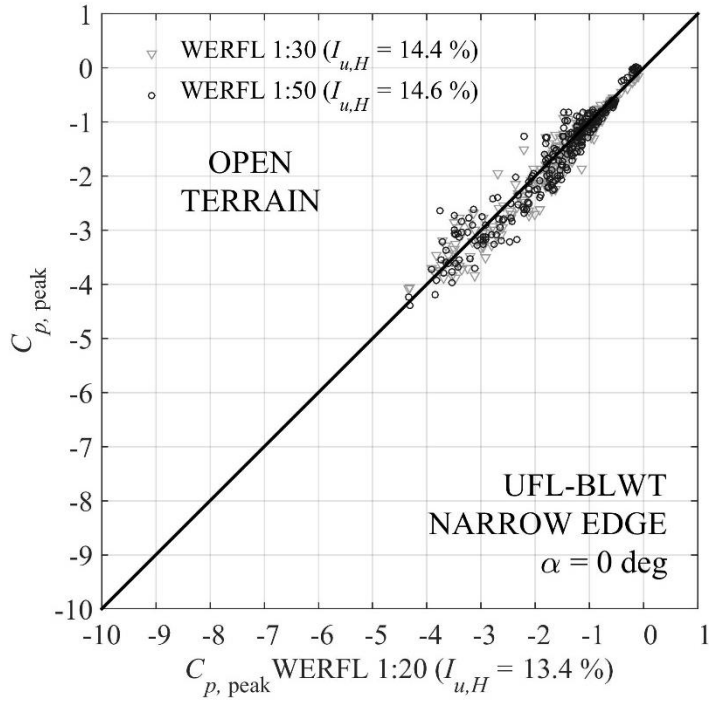
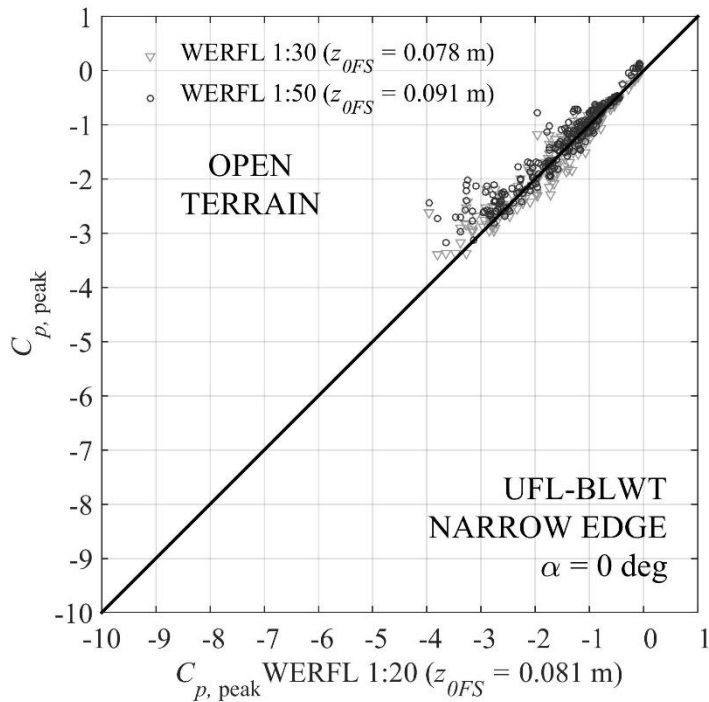


Figure 4-19. Distribution of peak pressures along a line of taps (parallel to the long building dimension) for the 1:50 WERFL model (Wide edge, $\alpha = 0^\circ$).

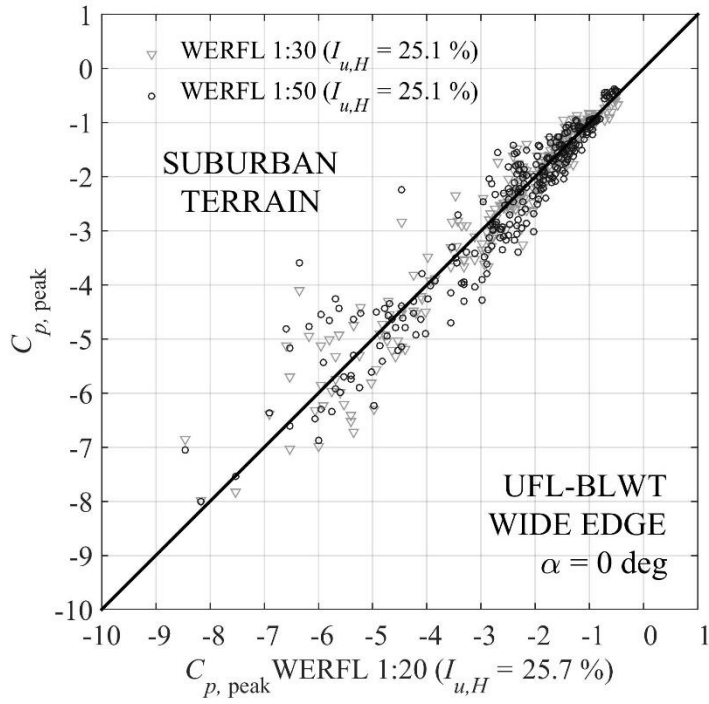


A

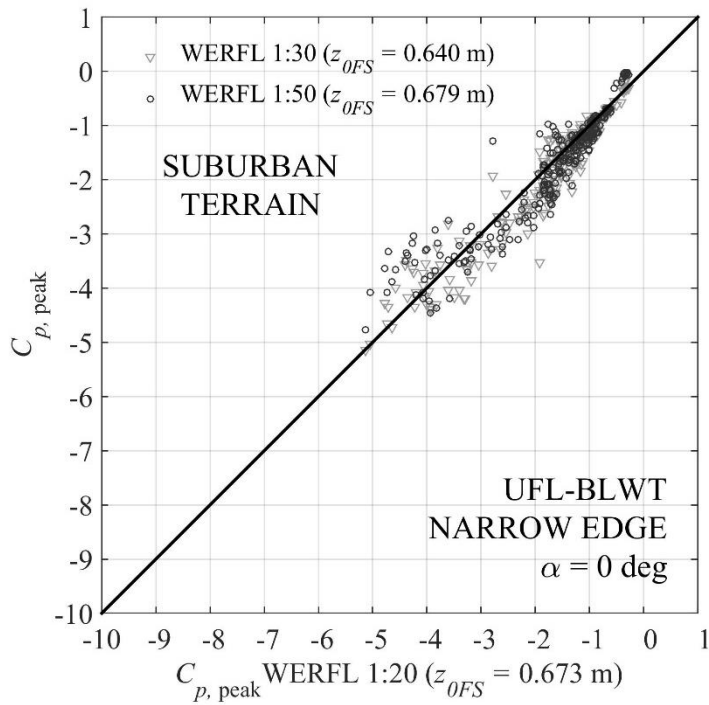


B

Figure 4-20. Peak pressures on all 266 taps for upwind terrains matching A) turbulence intensities (at eave height) and B) roughness lengths satisfying open country (0.01-0.15 m).

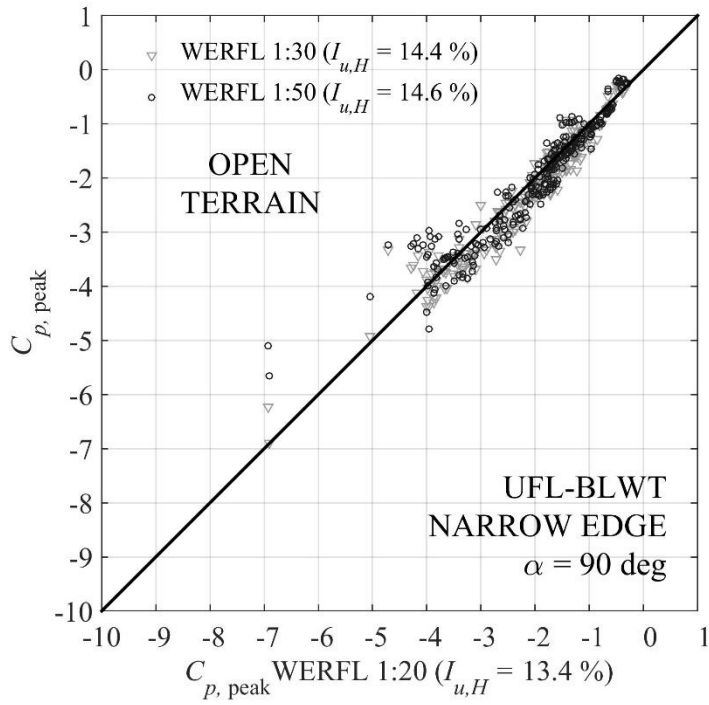


A

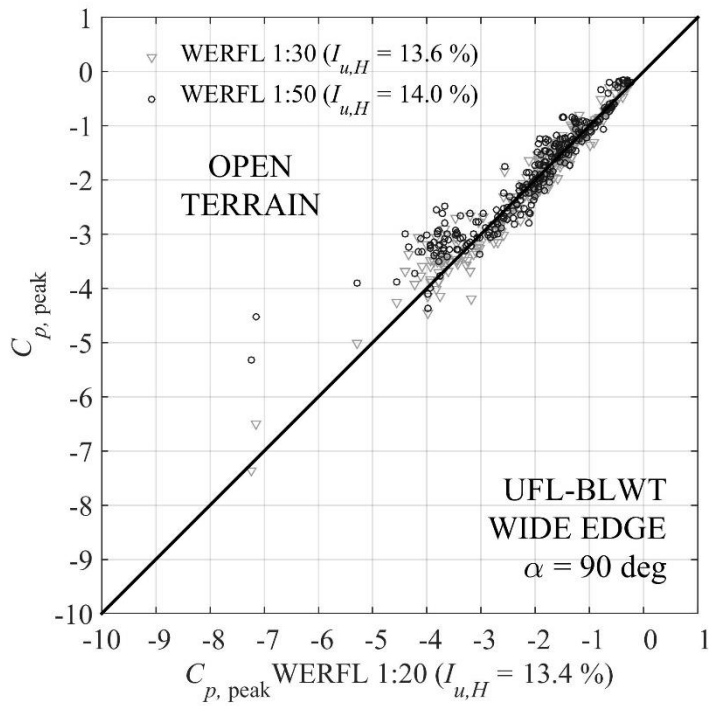


B

Figure 4-21. Peak pressures on all 266 taps for upwind terrains matching A) turbulence intensities (at eave height) and B) roughness lengths satisfying suburban exposure (0.01-0.15 m).



A



B

Figure 4-22. Peak pressures on all 266 taps for open country ($I_{u,H} \sim 14\%$) terrain simulation with A) narrow and B) wide edge windward element orientation.

CHAPTER 5 WIND LOAD DESIGN OPTIMIZATION OF STEEL FRAMES

This chapter presents an improved metaheuristic optimization method for large-scale frame structures that minimizes weight while satisfying strength and serviceability requirements. The proposed algorithm first *explores* then *exploits* (ETE) the search space, adjusting the influence of the local and global best designs on the selection of new candidate solutions. A discrete (stochastic) search scheme is activated in the late stages of the optimization procedure to exploit the (local) search space near the global optimum. The proposed method is successfully applied to two benchmark large steel frame structures: (1) a three-bay 24-story moment-resistant frame and (2) a seven-bay 60-story structure. ETE produced optimum weights for the 24-story frame that outperformed recently developed metaheuristic strategies. For the 60-story frame, optimum designs from 45 independent runs produced frame weights within 2% of results found through rigorously derived optimality criteria methods. The paper demonstrates how the proposed stochastic (local) search strategy performs minute alterations to the best design, while only permitting the creation of new designs capable of improving the (current) global best. ETE appears to significantly enhance the exploitation capabilities of Big-Bang-Big Crunch method, specifically for discrete sizing optimization of large steel frames with vast design domains.

Background

Automation of the structural design process of civil structures via high-level optimization strategies is expected to grow significantly in the upcoming decade, particularly for structural systems comprising hundreds to upwards of thousands of structural elements. Efficiently sizing these members to satisfy

code-based strength and serviceability requirements is a computationally demanding task, hence the need for new research to efficiently evaluate optimal solutions.

Deterministic optimization algorithms such as mathematical programming—e.g., sequential quadratic programming—and optimality criteria (OC) have been widely held methods for solving structural optimization problems (Haftka, 1985; Arora, 2004; Haftka, 2012; Fenton, 1974; Feury and Geradin, 1978). The OC algorithm is one of the most established methods for optimizing large-scale civil structures (Saka, 1984; Tabak and Wright, 1981; Khan, 1984; Sadek, 1992). For example, Chan and Grierson (1993) applied an efficient pseudo-discrete OC procedure for member sizing optimization of a 60-story planar steel framework subject to multiple deflection constraints. This resizing technique has been extensively applied to optimize the stiffness of tall buildings subject to multiple drift requirements (Chan et al., 2010; Zou and Chan, 2005; Huang et al., 2012; Spence and Gioffre, 2012; Spence and Kareem, 2013).

In practice, member sizing optimization of frames typically involves the selection of commercially available cross-sectional shapes from a list of standard steel sections that satisfy code-based serviceability and strength requirements while reducing the cost of material by minimizing the frame weight. Despite modifications to traditional deterministic optimization algorithms, such as OC, for discretizing sizing optimization problems (Arora, 2000), their practical application has been limited due to their complexity and inefficiency when applied to large-scale structures (Saka and Geem, 2013). Furthermore, large-scale problems are

highly susceptible to be trapped in subdomains (i.e., local optima) given the relatively vast search space.

The present study addresses these issues through a hybridized metaheuristic optimization algorithm designed to solve large-scale structural frame problems. Inspired from biological and physical processes found in nature, metaheuristic algorithms use high-level population-based strategies to guide stochastic search through the design domain of candidate solutions. Numerous studies (Camp et al., 2005; Li et al., 2009; Kaveh and Talatahari, 2009) have demonstrated their effectiveness in civil structure applications. For example, Li et al. (2009) created a heuristic particle swarm optimizer (HPSO) for pin-connected structures by hybridizing PSO and harmony search (HS) schemes. Camp (2007) implemented a big-bang big crunch (BB-BC) algorithm for continuous and discrete optimization of space trusses. Kaveh and Abbasgholiha (2011) applied BB-BC for weight minimization of steel sway frames subject to AISC-LRFD (2010) strength and serviceability requirements. However, only a few studies (e.g., Kicingner et al., 2005; Hasancebi et al., 2011; Azad and Hasancebi, 2015; Kaveh and Bolandgerami, 2017) have applied metaheuristic algorithms on large structural systems. Optimization of these systems—comprising thousands of design variables—require intelligent strategies capable of performing a global examination of the search space (i.e., exploration) and the restricted investigation around promising regions (i.e., exploitation) (e.g., Cuevas et al., 2014; Mitalili et al., 2014).

The proposed method is based on PSO and BB-BC for discrete sizing optimization of large-scale steel frames. A modification is introduced to allow a

steady transition from exploration during early stages of the optimization process to exploitation of the feasible domain at late stages, and a discrete (stochastic) search scheme is initiated in the late stages of the optimization procedure to exploit the designs near the global optimum. The proposed algorithm is successfully applied to two benchmark problems: (1) a 24 story three bay planar frame (2) and a 60-story seven-bay planar frame. Results obtained by the proposed algorithm for the 24-story frame compare to recently develop metaheuristic strategies. For the 60-story frame, optimum designs from 45 independent runs produced frame weights within 2% of results found through rigorously derived optimality criteria methods. The paper illustrates how the proposed stochastic search strategy performs small adjustments to the global best during late stages, while only permitting the generation of new candidate designs with the potential to overtake the (current) best design. This discrete stochastic scheme appears to enhance the exploitation capabilities of BB-BC (mostly influenced by a random distribution generator) for large-scale discrete sizing optimization problems.

Discrete Optimization of Multi-Story Frame Structures

Structural frame optimization selects the lightest combination of standard structural sections, resulting in minimum material cost while satisfying code-based serviceability and strength requirements. Here we analyze planar steel frames based on AISC-LRFD specifications (2010). Mathematically, the optimum design of multi-story steel frames can be formulated as follows:

find

$$\mathbf{X} = [X_{i=1}, X_2, \dots, X_{nd}] \quad (5-1)$$

to minimize

$$W(\mathbf{X}) = \sum_{i=1}^{nd} \rho_i A_i \sum_{j=1}^{nm} L_j \quad (5-2)$$

subject to

$$g_j^{LCR}(\mathbf{X}) = LCR_j - 1 \leq 0 \quad j = 1, \dots, nm \quad (5-3)$$

$$g_k^{ID}(\mathbf{X}) = ID_k - 1 \leq 0 \quad k = 1, \dots, ns \quad (5-4)$$

$$1 \leq X_i \leq Nsec_i \quad i = 1, \dots, nd \quad (5-1)$$

where each member of set \mathbf{X} is associated with a standard steel section for member group i ; nd is the total number of design variables (i.e., member groups). In Equation 5-2, $W(\mathbf{X})$ is the weight of the frame; ρ_i and A_i are the density and cross-sectional area of members in group i , respectively; L_j is the length of member j and nm is the total number of members; Equation 5-5 constrains the bounds of each design variable entry X_i ; $Nsec_i$ is the total number of standard steel sections in member group i . Equations 5-3 and 5-4 represent inequality constraints for strength (Equation 5-3) and serviceability (Equation 5-4) requirements based on AISC-LRFD specifications (2010). In Equation 5-3, LCR_j is the load-capacity ratio defined as:

$$LCR = \begin{cases} \frac{P_u}{\phi P_n} + \frac{8}{9} \left(\frac{M_{ux}}{\phi_b M_{nx}} + \frac{M_{uy}}{\phi_b M_{ny}} \right) & \text{if } \frac{P_u}{\phi P_n} \geq 0.2 \\ \frac{P_u}{2\phi P_n} + \left(\frac{M_{ux}}{\phi_b M_{nx}} + \frac{M_{uy}}{\phi_b M_{ny}} \right) & \text{if } \frac{P_u}{\phi P_n} < 0.2 \end{cases} \quad (5-6)$$

where P_u is the required axial strength (i.e., tension or compression), M_{ux} and M_{uy} are the required flexural strength for strong and weak axis bending, respectively ($M_{uy} = 0$ for planar frames); P_n is the available axial strength; M_{nx} and M_{ny} are the available flexural strength for strong and weak axis bending, respectively; ϕ_b is the resistance factor for bending equal to 0.90; ϕ is the axial resistance factor, which equals 0.90 and 0.90 for tension and compression members, respectively. Strength constraints presented herein—for steel frames using AISC-LRFD strength requirements—can readily be reformulated for optimum design of concrete (ACI 318, 2008) and wood framed structures (Wheat and Cramer, 2006).

Equation 5-4 shows the inequality constraint for inter-story drift requirement of multi-story buildings, where ID_k can be expressed as follows:

$$ID_k = \frac{\delta_k - \delta_{k-1}}{\delta_{allw}} \quad k = 1, \dots, ns \quad (5-7)$$

where $\delta_k - \delta_{k-1}$ is the relative lateral displacement of adjacent stories; δ_{allw} is the allowable interstory drift limit; ns is the total number of stories.

The following penalty function approach is applied to transform the constrained optimization problem presented in Equations 5-1 through 5-5 into an unconstrained one:

$$\psi(\mathbf{X}, p) = W(\mathbf{X})[1 + pC(\mathbf{X})] \quad (5-8)$$

where p is a penalty coefficient (typically 0.5-1.5), and $C(\mathbf{X})$ is the penalty function defined as

$$C(\mathbf{X}) = \sum_{j=1}^{nm} g_j^{LCR}(\mathbf{X}) + \sum_{j=1}^{ns} g_k^{ID}(\mathbf{X}) \quad (5-9)$$

Proposed ETE Algorithm

Particle Swarm Optimization (PSO)

PSO is a stochastic optimization technique (Eberhart and Kennedy, 1995) inspired from the social behavior of bird flocking and fish schooling. In PSO, a population (swarm) of individuals (particles) move through the search space of candidate solutions, periodically updating their positions and velocities based on both their own experience (particle best) and the experience of the swarm (global best). The updating rule in the original PSO is given by:

$$\mathbf{V}_i^{k+1} = \omega \mathbf{V}_i^k + c_1 r_1 (\mathbf{P}_i^k - \mathbf{X}_i^k) + c_2 r_2 (\mathbf{G}^k - \mathbf{X}_i^k) \quad i = 1, \dots, N \quad (5-10)$$

$$\mathbf{X}_i^{k+1} = \mathbf{X}_i^k + \mathbf{V}_i^{k+1} \quad i = 1, \dots, N \quad (5-11)$$

where \mathbf{X}_i^{k+1} and \mathbf{V}_i^{k+1} is the *position* (Equation 5-1) and *velocity* vectors of particle i at iteration $k + 1$, respectively; \mathbf{G}^k is the position of the best solution found among all candidates up to iteration k (global best); \mathbf{P}_i^k is the best position found by particle i up to iteration k (particle best); ω is the inertial weight parameter; N is the population size; c_1 and c_2 are called acceleration coefficients; r_1 and r_2 are uniformly distributed random numbers in the range of $[0,1]$.

PSO has proven effective in the global investigation (i.e., exploration) of the design domain. However, the algorithm has a tendency to easily be trapped in local optima (i.e., subdomains) during late stages of the optimization process

(Yang et al., 2007). Design problems with large search spaces—e.g., hundreds of design variables—are more susceptible to this phenomenon. Consequently, modifications to the original PSO scheme are abundant in literature (e.g., Li and Huang, 2007; Perez and Behdinana, 2007; Yang et al., 2007). This study attempts to address the limitations of PSO by precise control of the influence of \mathbf{G}^k on new particles, while preserving the exploratory capabilities of the original algorithm.

ETE Algorithm

The proposed ETE algorithm regulates the influence of \mathbf{G}^k at different stages of the optimization process via a single control parameter. In addition, a normal distribution operator adapted from the BB-BC algorithm (Erol and Eksin, 2006) is introduced to exploit promising regions within the search space at late iteration stages. The updating technique is formulated as follows:

$$\mathbf{X}_i^{k+1} = \text{round}[\theta_k \mathbf{G}^k + (1 - \theta_k) \mathbf{P}_i^k] + \mathbf{d}_i \quad i = 1, \dots, N \quad (5-12)$$

where θ_k is a control parameter that linearly increases over a user-specified number of generations to control the relative influence of \mathbf{P}_i^k and \mathbf{G}^k ; \mathbf{d}_i is a normal distribution operator from the BB-BC algorithm (Erol and Eksin, 2006). In this study, \mathbf{d}_i is defined as:

$$\mathbf{d}_i = \text{round} \left[\alpha \mathbf{r}_i^n \left(\frac{\mathbf{X}_{max} - \mathbf{X}_{min}}{k} \right) \right] \quad i = 1, \dots, N \quad (5-13)$$

in which \mathbf{r}_i is a random generated from a standard normal distribution; α is a parameter for controlling the size of the search space; n is an exponential parameter ($n = 3$ for this study); \mathbf{X}_{max} and \mathbf{X}_{min} are the position vectors of the

upper and lower bounds of each design variable, respectively. A comparable updating scheme to the one shown in Equation 5-12 can be found in Kaveh and Abbasgholiha (2010).

Figure 5-1 presents a flowchart of the proposed ETE algorithm. Similar to most metaheuristic methods, an initial population—i.e., swarm—is created via a uniform random number generator bounded by \mathbf{X}_{max} and \mathbf{X}_{min} . The penalized objective function is then evaluated for each candidate solution—i.e., particle. After assessing the fitness of each particle, \mathbf{P}_i^k and \mathbf{G}^k are determined. New candidate solutions emerge from Equation 5-12. In subsequent iterations, θ_k is recalculated using Equation 5-14. This process is repeated until the maximum number of iterations k_{max} is reached.

Linearly Varying Control Parameter

During each iteration, θ_k is adjusted to progressively intensify the influence of the global best solution (\mathbf{G}^k) on the swarm, thus effecting a gradual transition from exploration to exploitation of the search space. In Equation 5-12, θ_k is increased linearly after each iteration k following

$$\theta_k = \left(\frac{\theta_f - \theta_i}{\beta k_{max} - 1} \right) (k - 1) + \theta_i \quad (5-14)$$

where k_{max} is the maximum number of iterations; β is a parameter which defines the iteration when θ_k will transition from a linear variation to a final constant value; θ_i and θ_f are the initial and final values ($\theta_i = \theta_{k=1}$ and $\theta_f = \theta_{k=\beta k_{max}}$). The dynamic behavior of θ_k is represented graphically in Figure 5-2. At early iterations, it is desirable for new candidate solutions to be influenced by both the best solution found by the particle (\mathbf{P}_i^k) and swarm (\mathbf{G}^k). For example, if $\theta_i = 0.5$,

\mathbf{P}_i^k and \mathbf{G}^k will equally impact the new position \mathbf{X}_i^{k+1} . As the optimization carries on, new positions gradually become more attracted to the global best solution, searching more in the vicinity of \mathbf{G}^k . When iteration βk_{max} is reached, \mathbf{X}_i^{k+1} will be mostly—or completely, given $\theta_f = 1.0$ —influenced by \mathbf{G}^k , as portrayed by the exploitation phase. In this final stage, the algorithm performs a local search around \mathbf{G}^k —i.e., $\mathbf{X}_i^{k+1} = \mathbf{G}^k + \mathbf{d}_i$.

Discrete Stochastic (Exploitation) Scheme

In metaheuristics, design optimization of large steel frames typically requires a high number of iterations (Hasançebi et al., 2011). From Equation 5-13, it is evident that \mathbf{d}_i approaches 0 as k becomes large. If $\mathbf{d}_i = 0$ and $\theta_k = 1.0$, the new particle \mathbf{X}_i^{k+1} will remain in the same position as the global best \mathbf{G}^k , according to Equation 5-12. Additionally, if every entry in \mathbf{d}_i is equal to or greater than 0, \mathbf{X}_i^{k+1} is certain to produce a worst solution than \mathbf{G}^k . To address this, a conditional routine (Figure 5-3) is added to the proposed algorithm if either condition is satisfied.

First, a new \mathbf{d}_i is pre-allocated with a vector of zeros. Second, an entry j in vector \mathbf{d}_i is selected randomly and assigned a negative integer between $-a$ and 1. Finally, an integer between 0 and c is allocated to either entry $j - 1$ or $j + 1$ of \mathbf{d}_i . The rationale behind the routine is that nearby entries in \mathbf{d}_i typically implies neighboring members in the physical structure. A small increase in the cross-sectional area (i.e., size-up) of a group of members may allow a considerable size reduction (i.e., size-down) of a nearby member group.

Results

This section examines the efficiency and robustness of ETE for optimizing large planar steel frames. Two benchmark frame problems are considered: (1) a three-bay 24-story steel frame and (2) a seven bay 60-story steel structure, both subject to strength and inter-story drift requirements from AISC (2010).

The ETE was applied to each benchmark problem for three cases, namely $\beta = 0.25, 0.50,$ and 0.75 . In both problems, $N = 80, p = 0.5, \theta_i = 0.5, \theta_f = 1.0,$ and $\alpha = 0.6$. For the 24 story frame, 100 independent runs were performed for each β case—300 total runs. The algorithm was executed 15 times on the 60 story frame for each β case, for a total of 45 runs. The maximum number iterations (k_{max}) was set to 200 and 1000 for the 24 and 60 story frames, respectively.

Structural analysis (i.e., 1st order, elastic direct stiffness technique) and the ETE algorithm were coded in MATLAB. Runs were executed from a personal computer—8 Core Intel Xeon CPU E5440 @ 2.83 GHz with 24 GB RAM—using independent parallel processing.

24 Story Three-Bay frame

Figure 5-4 shows the topology, load condition, and member grouping for the subject three-bay twenty-four story planar frame. The frame has been studied by Kaveh and Talatahari (2010), applying an improved ant colony optimization (IACO), Togan (2012) via teaching-learning based optimization (TLBO) algorithm, Safari et al. (2013) utilizing a modified multiple-deme genetic algorithms (MMDGA), among others. The structure comprises 168 members arranged into 20 groups. Groups 1-4 and 5-20 correspond to beam and column

members, respectively. Beam sections are selected from all 267 W-Shapes and columns are chosen from a set of 37 W14 shapes. The magnitude of the loads displayed in Figure 5-4 are $W = 25.628$ kN, $w_1 = 4.378$ kN/m, $w_2 = 6.362$ kN/m, $w_3 = 6.917$ kN/m, $w_4 = 5.954$ kN/m. The modulus of elasticity and yield stress are $E = 205$ GPa and $F_y = 230.3$ MPa, respectively. Design for strength follows LRFD-AISC specifications (2010). Beams and columns are assumed unbraced along their length. The effective length factors of the members are computed as $K_x \geq 0$ for a sway permitted frame and the out-of-plane effective length factor is $K_y = 1.0$. Inter-story drift limit is set to $h/300$ for all stories.

Table 5-1 summarizes the statistics of final weights from 300 independent runs for the 24-story frame. The lightest design resulted in a final weight of 894.3 kN. For this run, $\beta = 0.25$ (Case 1). The worst (heaviest) design produced a final weight of 986.3 kN (Case 2). A slight reduction in the variability (standard deviation) of the final weight is observed as β increases. Additionally, a greater number of optimum designs (runs) are closer to the best design for each case, as shown in Table 5-2. This might be attributed to a more exhaustive (i.e., exploration) search with increasing β —the influence of \mathbf{P}_i^k is present for a longer period. For instance, runs with $\beta = 0.75$, 52 of 100 runs were within +1.0% of the best (case) solution (Table 5-2), while 91 of 100 were within +5.0%.

Figure 5-5 includes iteration histories of the mean weight from 100 runs for the 24 story frame. During iterations ($k = 20-100$), case 1 shows a faster (mean) weight improvement than Cases 2 and 3, suggesting a stronger influence of the global best (\mathbf{G}^k) for case 1 during early stages. For example, at $k = 50$, $\theta = 1.0$, 0.75, and 0.66 for cases 1, 2, and 3, respectively. However, at iterations

150-200, mean weights of case 3 surpasses cases 1 (at $k \sim 162$) and 2 (at $k \sim 165$).

Optimum weights and W-shape sections obtained by ETE are shown in Table 5-3, and compared to other recent metaheuristic techniques. The best design attained by ETE (894.3 kN) is 8.4%, 1.1%, and 0.43% lighter than IACO, TLBO, and MMDGA, respectively.

Figures 5-6 and 5-7 show the inter-story drift, load-capacity ratio, and member size distribution of the best run from Cases 1 and 3 for the 24 story frame, respectively. Member line thicknesses are proportional to the square-root of the area (i.e., $\sqrt{A_j}$). The best design obtained by ETE satisfies strength and serviceability requirements for all three cases of the 24 story frame.

60 Story Seven-Bay Frame

The sixty story seven bay trussed frame shown in Figure 5-8 was first optimized in Chan (1992) using the OC method. All seven bays span 6.096 m and all stories are 3.658 m in height. Beam to column joints are rigidly connected, while K-bracing members are assumed to be pinned at their ends. The eight joints at the base of the frame are modeled as fixed supports. Only wind loading is considered.

The frame consists of 1080 members (Table 5-4), which are convened into 240 groups. Beams located on the same story are grouped together (i.e., 60 beam groups). The same applies for diagonal bracings. Columns are grouped over two adjacent stories and symmetrical columns correspond to the same group. Steel sections for beam groups selected from a discrete set of 21 W24

sections, while column and bracing groups can chose from 36 W14 sections. The total number of combinations is approximately 10^{360} .

In this study, the frame is design for inter-story drift and strength requirements based on LRFD-AISC specifications (2010). Beams and columns are assumed to be unbraced along their length. The modulus of elasticity is $E = 200$ GPa. A yield stress of $F_y = 300$ MPa was selected to match the material properties used in Walls and Elvin (2010). Inter-story drift limit is $h/400$ for each of the 60 stories.

Statistics of final weights from 45 independent runs—15 runs per case—for the 60 story frame are shown in Table 5-5. As is the case for the 24 story frame, the worst run correspond to $\beta = 0.25$ (22.835 MN). The best run resulted in a final weight of 22.448 MN. The β parameter was set to 0.75 in this run. Mean (final) weights seem to decrease as β increases. Case 1 produced the highest variability in the final weight, with a standard deviation of 0.122 MN. Case 2 ($\beta = 0.25$) produced less spread in the final weight.

Table 5-6 includes a comparison of ETE with other optimization techniques for the 60 story frame. The best run of ETE is 1.2% lighter than the OC simple round-up solution, and 1.58% heavier than the pseudo round-up technique (Chan, 1992). However, neither of the two OC methods presented in Chan (1992) considered strength requirements. Wall and Elvin (2010) introduced strength requirements to the 60 story frame based on SANS (2005), and achieved an optimum weight of 22.436 MN using VWO. This design is 0.05% lighter than the best run of ETE (22.445 MN), which incorporated strength limit states from AISC-LRFD (2010). Distinctions in code specification hinders direct

comparison of the results of VWO and ETE. Nonetheless, it is evident that ETE can achieve comparable results to numerical methods (i.e., OC and VWO) for large-scale frames.

Mean iteration history curves for the 60 story frame are shown in Figure 5-9. Similar to the 24 story frame, case 1 shows a rapid reduction of the mean weight during early iterations ($k = 250-600$) compared to cases 2 and 3. However, the iteration curve for case 3 falls just below Case 2 from $k = 200-525$, contrary to what should be expected. This could be due to the limited number of runs for the 60 story problem—15 runs. Regardless, mean weights of case 3 better cases 1 and 2 at late stages of the optimization ($k = 750-1000$).

While absent in Figure 5-5, Figure 5-9 shows abrupt slope changes (“kinks”) in the iteration history curves (e.g., at $k = 500$ for case 2). These “kinks” mark points where the algorithm first reaches $\theta = 1.0$. A more rapid improvement—steeper slope—in the mean weight is observed past these points. At this stage of the optimization process, some particles are satisfying the conditional statement of Figure 5-3, allowing recalculation of \mathbf{d}_j . As a consequence, more particles have a chance to overtake \mathbf{G}^k .

Inter-story drift and member size distribution, and load-capacity ratios of the best run from Cases 2 and 3 for the 60 story frame are shown in Figures 5-10 and -211, respectively. As previously mentioned, member line thicknesses are scaled proportional to $\sqrt{A_j}$. It is apparent that inter-story drift constraints controls the optimum design.

Summary

This chapter presents an exploration-to-exploitation (ETE) algorithm for discrete optimization of large frame structures. The algorithm was tested on two benchmark steel frame problems. First, ETE was applied to a 24-story planar steel frame subject to AISC-LRFD strength and inter-story drift requirements. The best designs from ETE outperformed recently developed meta-heuristic algorithms (IACO, TLBO, and MMDGA). The second benchmark problem was a 60-story seven bay frame. Optimum designs obtained using ETE compared to results from CH92 and WE10. Differences in optimum weights can be ascribed to (1) the absence of strength constraints in the OC algorithm, and (2) distinctions in code specifications used to satisfy strength requirements—AISC-LRFD (2010) and SANS (2005).

This study demonstrated the capabilities of ETE to execute a comprehensive search of the vast design domain associated with large steel structures. Despite the random nature of the algorithm, optimum designs from ETE compared to rigorously-derived deterministic methods, without the use of domain knowledge—OC and VWO employ the principle of virtual work for identifying the most effective structural members.

Subsequent work will concentrate on significantly reducing the computational time—number of structural analysis—of ETE, which remains one of the main drawbacks of most metaheuristic algorithms for structural optimization.

Table 5-1. Summary of statistics for optimum design of 24 story three-bay frame (100 Runs).

Case		Case 1 $\beta = 0.25$	Case 2 $\beta = 0.5$	Case 3 $\beta = 0.75$
Final	Maximum (worst run)	966.9	986.3	967.7
Weight	Mean	913.4	912.6	910.7
(kN)	Minimum (best run)	894.3	895.8	896.5
	Standard Deviation (kN)	18.0	17.0	15.2
	Coefficient of variation (%)	1.97	1.87	1.67

Table 5-2. Percent difference relative to best run for 24 story three-bay frame (100 Runs).

% Greater than Best (Case) Run	No. of Independent Runs		
	Case 1 $\beta = 0.25$	Case 2 $\beta = 0.5$	Case 3 $\beta = 0.75$
$\leq +0.1$	0	1	3
$\leq +0.5$	14	22	28
$\leq +1.0$	31	42	52
$\leq +5.0$	84	89	91

Table 5-3. Comparison of best designs for 24 story three-bay frame.

Group No.	AISC W –Shapes					
	IACO (Kaveh et al., 2010)	TLBO (Togan, 2012)	MMDGA (Safari et al., 2013)	Present Study		
				Case 1 $\beta = 0.25$	Case 2 $\beta = 0.5$	Case 3 $\beta = 0.75$
1	W30X99	W30X90	W30X90	W30X90	W30X90	W30X90
2	W16X26	W8X18	W8X15	W6X15	W6X15	W6X15
3	W18X35	W24X62	W24X55	W24X55	W24X55	W24X55
4	W14X22	W6X9	W10X15	W6X8.5	W6X8.5	W6X8.5
5	W14X145	W14X132	W14X159	W14X159	W14X15 9	W14X14 5
6	W14X132	W14X120	W14X132	W14X132	W14X12 0	W14X13 2
7	W14X120	W14X99	W14X90	W14X109	W14X10 9	W14X12 0
8	W14X109	W14X82	W14X90	W14X74	W14X74	W14X74
9	W14X48	W14X74	W14X65	W14X61	W14X61	W14X68
10	W14X48	W14X53	W14X48	W14X38	W14X43	W14X38
11	W14X34	W14X34	W14X48	W14X38	W14X34	W14X30
12	W14X30	W14X22	W14X22	W14X22	W14X22	W14X22
13	W14X159	W14X109	W14X109	W14X90	W14X90	W14X99
14	W14X120	W14X99	W14X99	W14X99	W14X10 9	W14X99
15	W14X109	W14X99	W14X99	W14X90	W14X90	W14X90
16	W14X99	W14X90	W14X74	W14X90	W14X90	W14X90
17	W14X82	W14X68	W14X68	W14X74	W14X74	W14X68
18	W14X53	W14X53	W14X53	W14X61	W14X61	W14X61
19	W14X38	W14X34	W14X26	W14X30	W14X34	W14X38
20	W14X26	W14X22	W14X22	W14X22	W14X22	W14X22
Weight (kN)	969.25	903.88	898.19	894.32	895.83	896.54

Table 5-4. Location of structural members in the 60-story frame.

Members	Location in the structure
1-60	Exterior columns (C1)
61-120	1 st interior columns (C2)
121-180	2 nd interior columns (C3)
181-240	3 rd interior columns (C4)
241-300	3 rd Interior columns (C5)
301-360	2 nd interior columns (C6)
361-420	1 st interior columns (C7)
421-480	Exterior columns (C8)
481-540	Beams bay 1
541-600	Beams bay 2
601-660	Beams bay 3
841-900	Beams bay 4
901-960	Beams bay 5
661-720	Beams bay 6
721-780	Beams bay 7
781-840	Beams bay 8
961-1020	Bracings bay 4
1021-1080	Bracings bay 5

Table 5-5. Summary of statistics for optimum design of 60 story seven-bay frame (Independent Runs = 15).

Case		Case 1	Case 2	Case 3
		$\beta = 0.25$	$\beta = 0.5$	$\beta = 0.75$
Final	Maximum (worst run)	22.835	22.699	22.713
Weight	Mean	22.625	22.581	22.571
(kN)	Minimum (best run)	22.454	22.500	22.448
	Standard Deviation (kN)	0.122	0.053	0.071
	Coefficient of variation (%)	0.54	0.23	0.31

Table 5-6. Percent difference relative to best run for 60 story seven-bay frame (Independent Runs = 15).

% Greater Than Best (Case) Run	No. of Independent Runs		
	Case 1 $\beta = 0.25$	Case 2 $\beta = 0.5$	Case 3 $\beta = 0.75$
$\leq +0.1$	0	1	0
$\leq +0.5$	5	11	7
$\leq +1.0$	10	14	12
$\leq +5.0$	14	14	14

Table 5-7. Optimum design comparison for the 60 story planar frame.

Method	Weight (kN)	% Greater (Heavier) Than Best Run	Constraints	
OC simple round-up (Chan, 1992)	22.716	+1.20	Inter-story drift	
OC pseudo round-up (Chan, 1992)	22.093	-1.58	Inter-story drift	
VWO (Wall and Elvin, 2010)	22.436	-0.05	Inter-story drift and strength (SANS, 2005)	
Present Work	Worst Run	22.827	+1.70	Inter-story drift and strength (AISC-LRFD, 2010)
	Best Run	22.445	-	Inter-story drift and strength (AISC-LRFD, 2010)

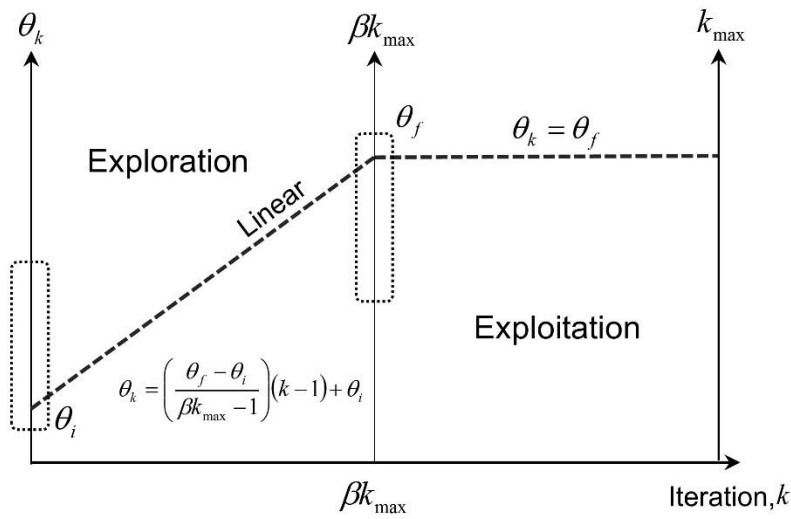


Figure 5-1. Linear variation of θ_k during the optimization process.

```

function  $\mathbf{d}_i = \text{recalcd}(\theta_k, \mathbf{d}_i)$ 
  if  $\theta_k = 1.0$  and  $\min(\mathbf{d}_i) \geq 0$  then
     $\mathbf{d}_i = \text{zeros}(1, nd)$ 
     $j = \text{randi} \rightarrow [1 \ nd]$ 
     $a = \text{round}(\sqrt[3]{N_{sec,j}})$ 
     $d_{i,j} = \text{randi} \rightarrow [-a \ -1]$     % Size-Down
    if  $j = nd$  then
       $b = \text{round}(\sqrt[3]{N_{sec,j-1}})$ 
       $d_{i,j-1} = \text{randi} \rightarrow [0 \ b]$     % Size-Up
    else
       $c = \text{round}(\sqrt[3]{N_{sec,j+1}})$ 
       $d_{i,j+1} = \text{randi} \rightarrow [0 \ c]$     % Size-Up
    end
  else
     $\mathbf{d}_i \rightarrow \text{Eq. 13}$ 
  end
end

```

Figure 5-2. Conditional subroutine for determining \mathbf{d}_i .

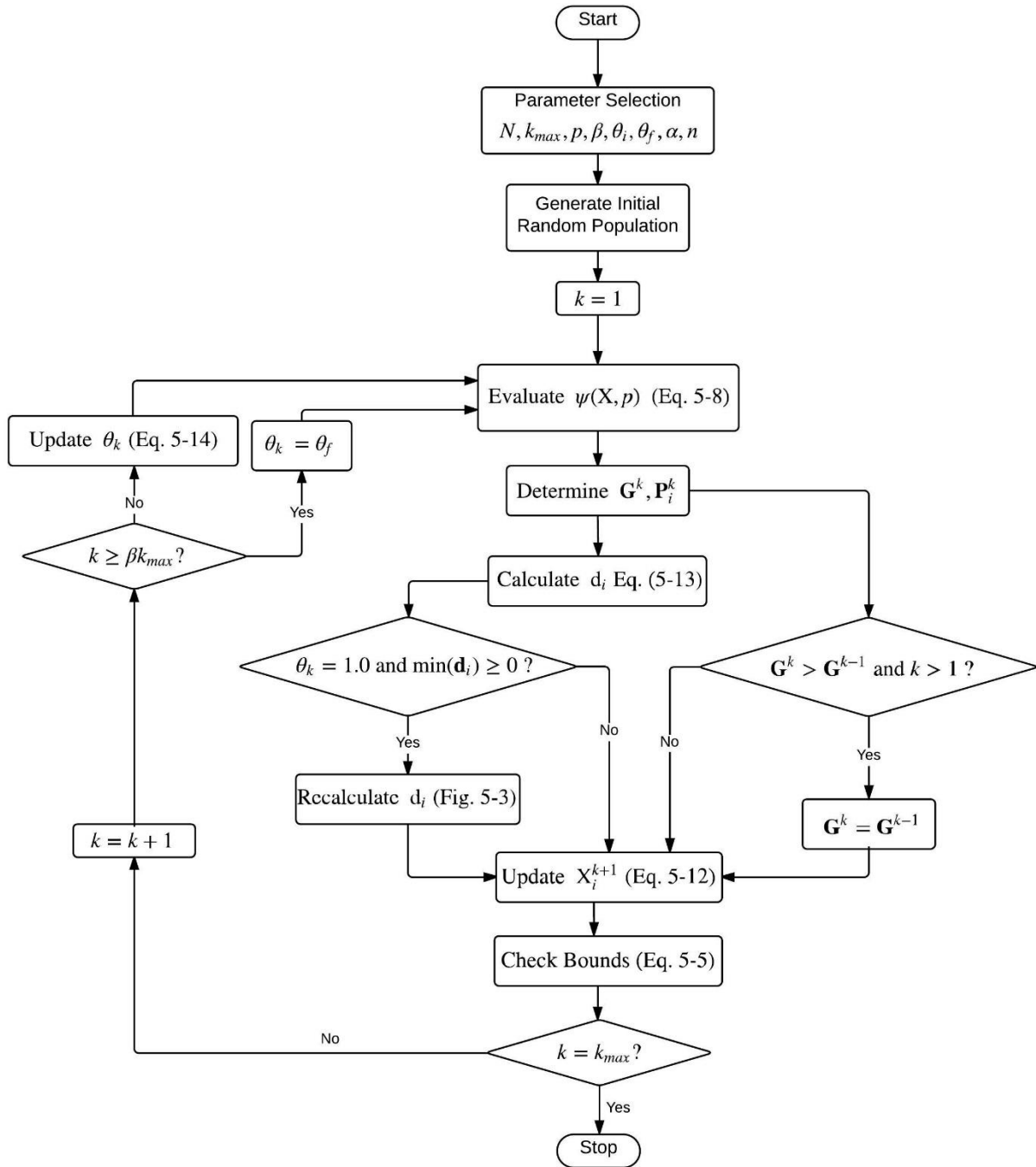


Figure 5-3. Flowchart of ETE for discrete sizing design optimization of framed structures.

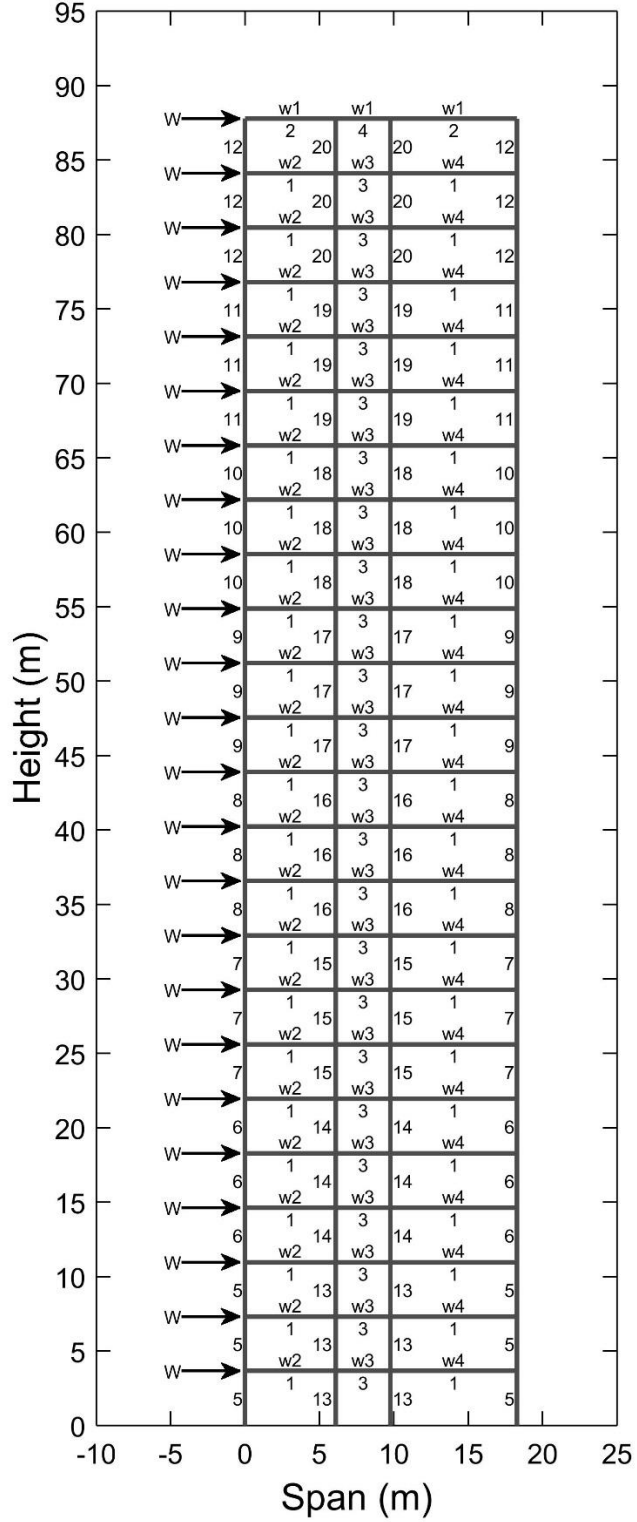


Figure 5-4. Topology and loading condition of 24 story three-bay planar frame.

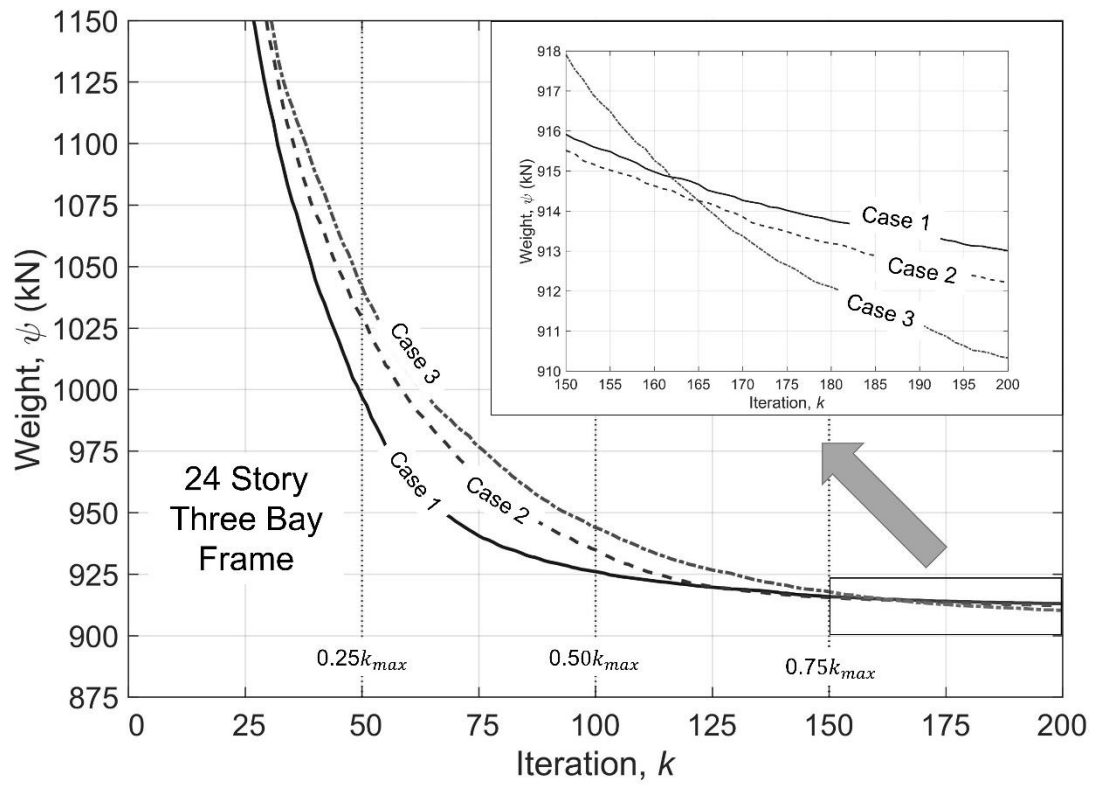


Figure 5-5. ETE mean optimization history (24 story three-bay frame).

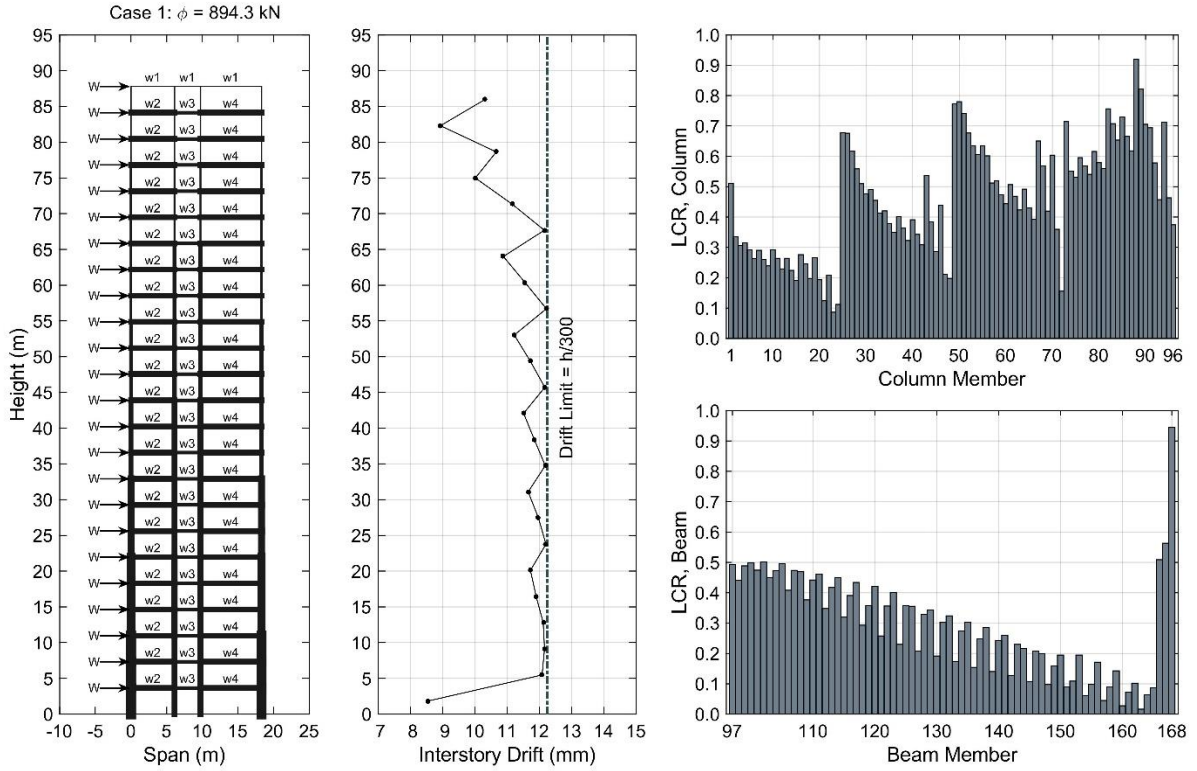


Figure 5-6. Member sizing, inter-story drift, and load-capacity ratios for the 24 story three-bay frame obtained using ETE (Case 1, $\beta = 0.25$).

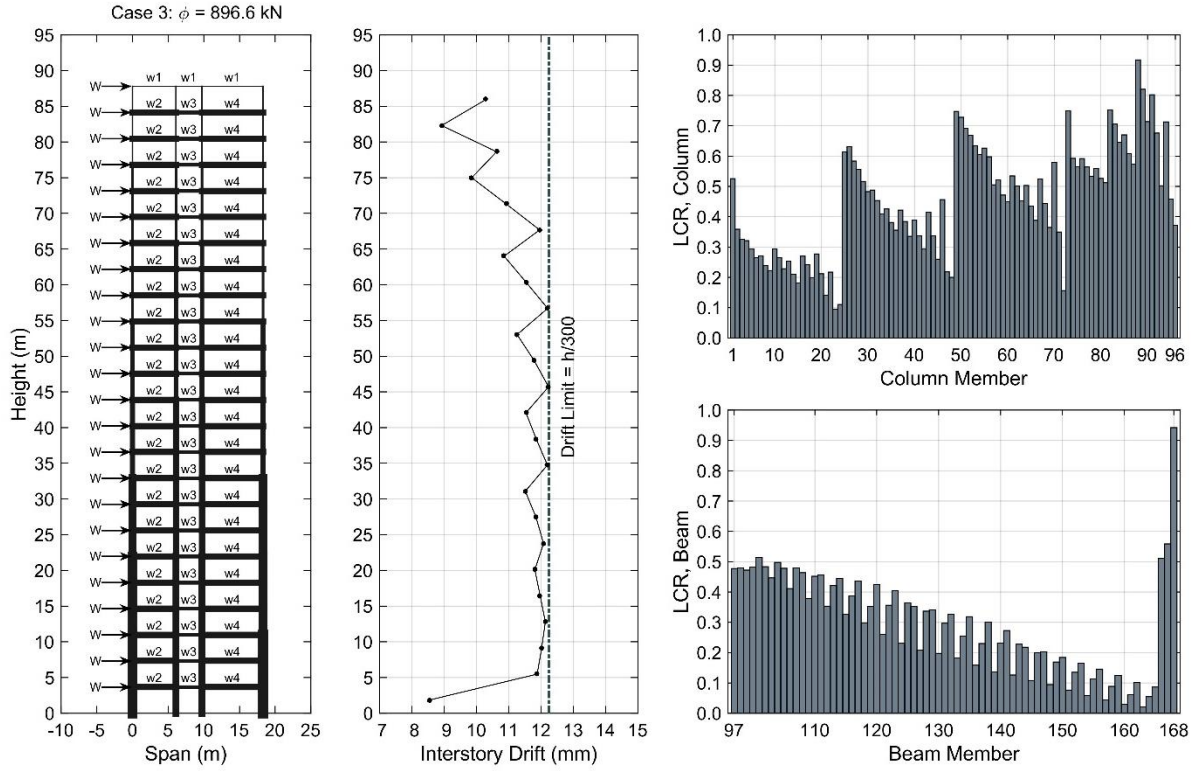


Figure 5-7. Member sizing, inter-story drift, and load-capacity ratios for the 24 story three-bay frame obtained using ETE (Case 3, $\beta = 0.75$).

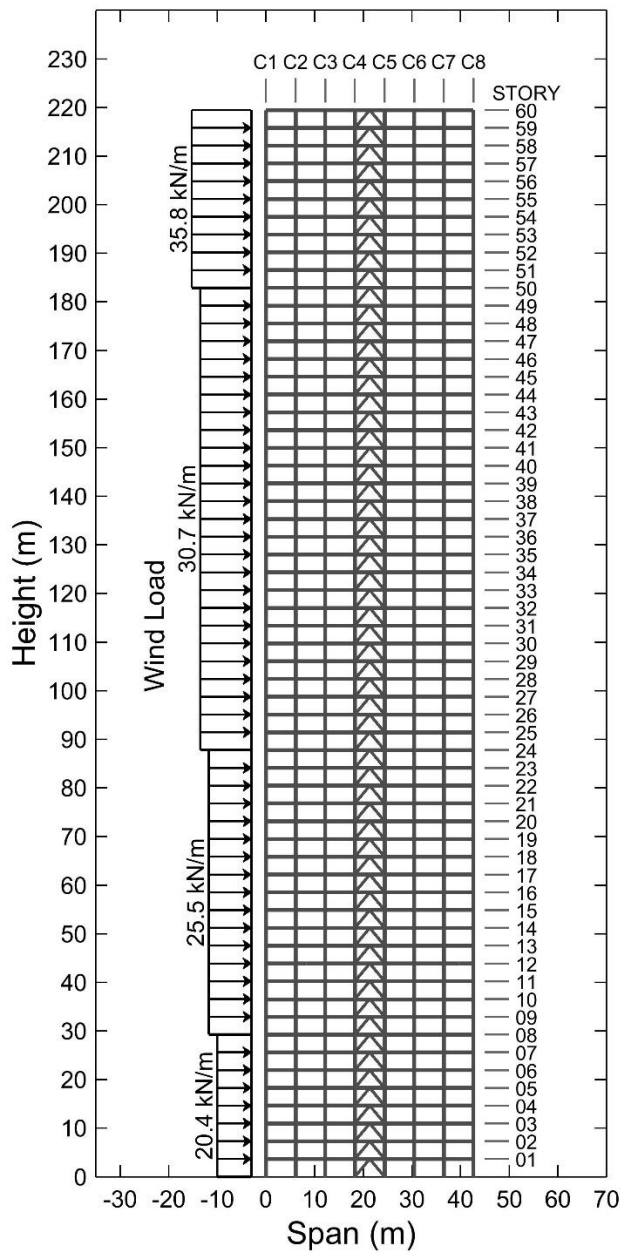


Figure 5-8. Topology and loading condition of 60 story seven-bay planar frame.

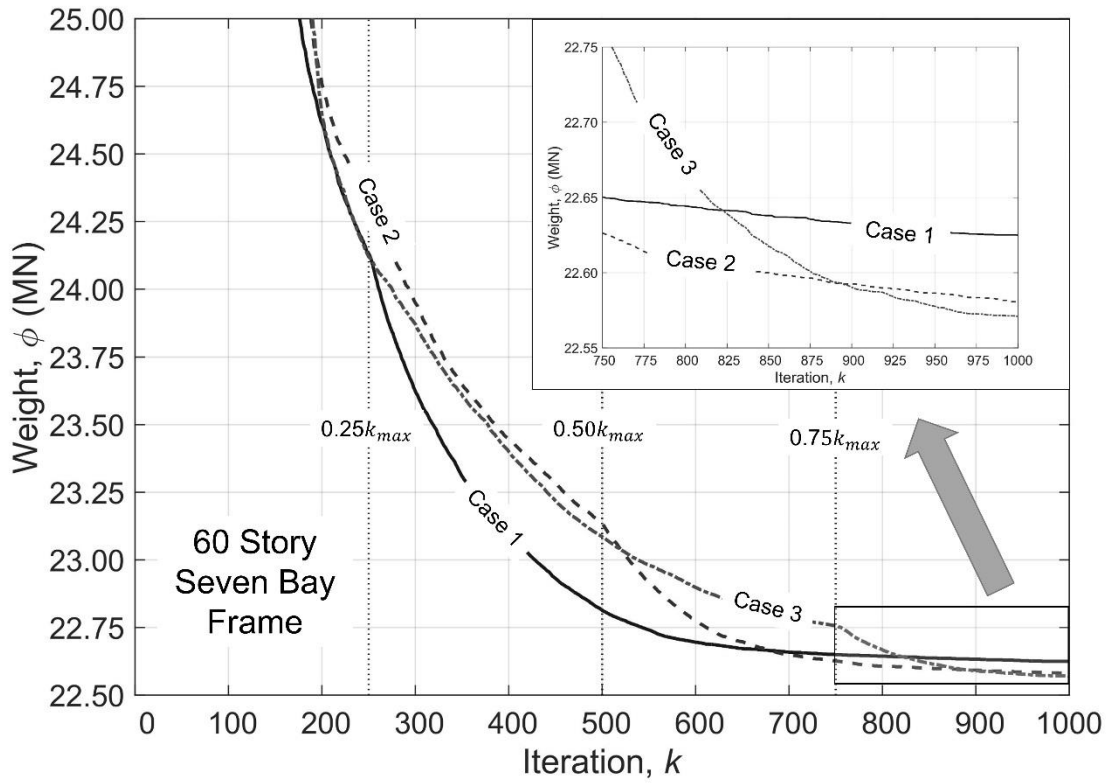


Figure 5-9. ETE mean optimization history (60-story seven-bay frame).

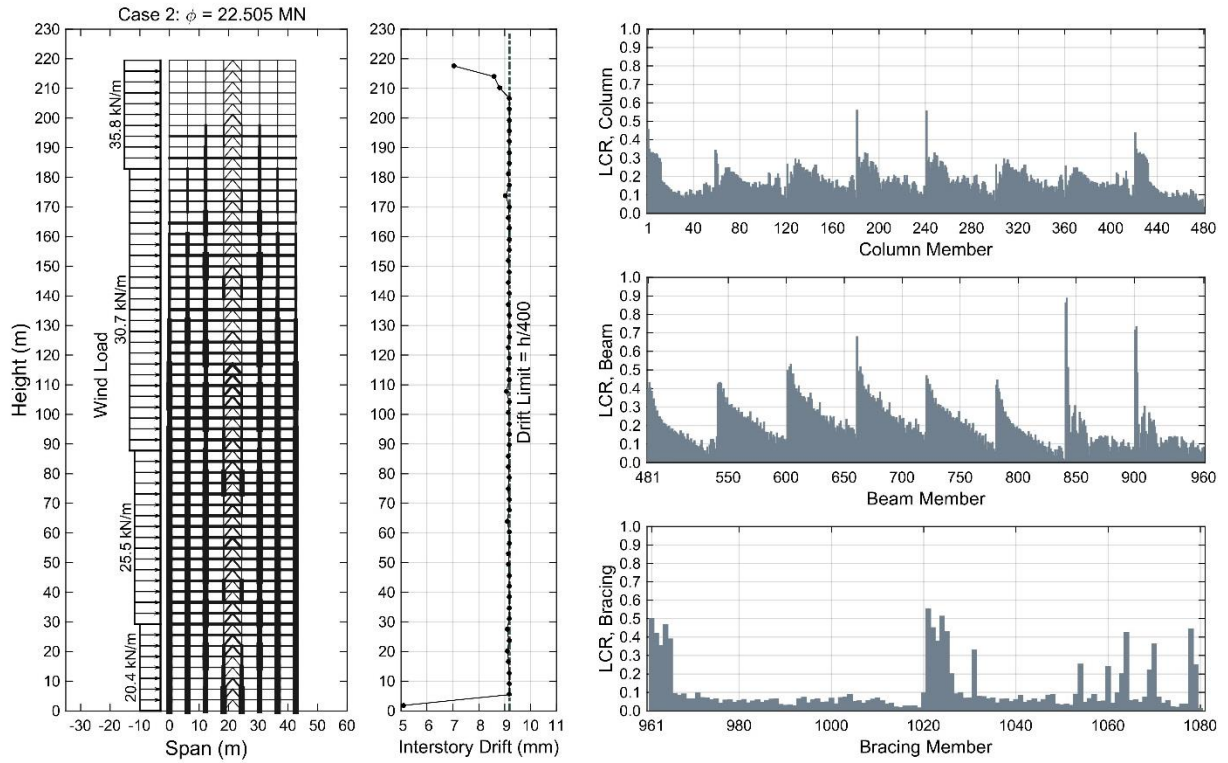


Figure 5-10. Member sizing, inter-story drift, and load-capacity ratios for the 60 story seven-bay frame obtained using ETE (Case 2, $\beta = 0.5$).

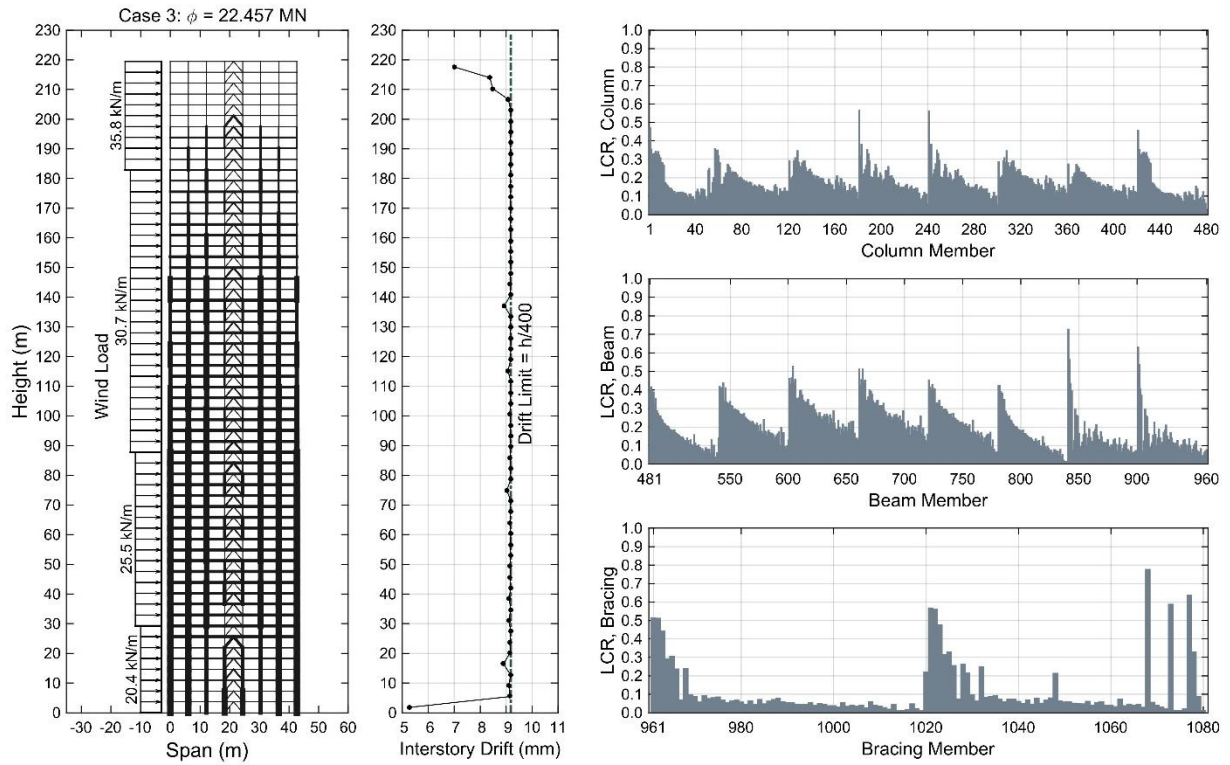


Figure 5-11. Member sizing, inter-story drift, and load-capacity ratios for the 60 story seven-bay frame obtained using ETE (Case 3, $\beta = 0.75$).

CHAPTER 6 CONCLUSIONS AND FUTURE WORK

Contributions, final remarks, and recommendations for future research resulting from this dissertation are outlined herein. The sections follow the order in which the topics were presented in the document.

Field Measurements of Hurricane Winds

As part of this dissertation, nine new field experiments (from Hurricanes Hermine and Matthew) collected during the 2016 Atlantic hurricane season were added to the FCMP database, which includes near-surface wind observations from 25 named storms since 1998. Recent field deployments have targeted suburban terrain exposures to investigate the turbulent structures in the roughness sublayer (RS) during strong wind events. Skewed distributions of the longitudinal velocity component were observed within the RS. Quadrant analysis of the Reynolds stress demonstrated the link of skewed distributions sweep dominance—downward transfers of momentum.

Future field experiments should continue to target suburban terrains, since most of the FCMP database consist of wind observations measured in open and marine exposures. Furthermore, the use of 15 m weather stations, equipped with ultrasonic anemometry along the height of the tower, provides valuable insight of how the statistical moments of the three velocity components (e.g., mean, variance, skewness, and kurtosis) vary with height in the RS.

Surface Pressures on Low-Rise Buildings

Most wind tunnel studies assessing extreme surface pressures on low buildings have been limited to two terrain conditions, namely open and suburban. Simulation of these two terrains is traditionally achieved by manual modification of the upwind terrain

through implementation of mixing devices—e.g., vortex generators, roughness grid, barriers—until aerodynamic parameters, such as roughness length, closely match predefined values from wind load provisions.

Preliminary results from a comprehensive series of experiments on low-rise buildings revealed that the peak (minimum) pressure coefficients are terrain dependent. Modern wind load provisioning such as ASCE 7 uses external pressure coefficients re-normalized to open exposure terrain, and do not, for example, prescribe pressure distributions on the building for terrain type. Furthermore, the increase was found to be more pronounced in regions of the largest negative pressure (e.g., roof corners). Root-mean square values of pressure coefficients appear to follow a nearly linearly proportional relation with increasing surface roughness.

Wind tunnel experiments presented in this dissertation could serve as a testbed for exploring more complex upwind terrains, such as heterogeneous roughness element fields, to simulate more realistic topographic conditions and the adverse wind-induced effects on low-rise buildings. Further, all data will be available in the Design Safe Cyberinfrastructure (CI) node at the University of Texas at Austin. Design Safe is a web-based research platform of the Natural Hazards Engineering Research Infrastructure (NHERI) Network. The website provides computational tools needed for managing, analyzing, and understanding critical data for natural hazards research.

Design Optimization of Large Civil Structures Subject to Wind Loads

Metaheuristic search techniques have the potential to become a common tool for design practitioners to enhance the performance of civil structures subject to wind. The simple yet versatile nature of these algorithms when compared to gradient based methods (e.g., optimality criteria) makes them a viable choice for practical design

problems, and could be incorporated to existing performance based design (PBD) frameworks for optimal design of wind exited tall buildings. Future research should focus on significantly reducing the computational time—number of structural analysis—of the algorithms for large problems. However, the ever growing abundance computational resources could naturally resolve this limitation.

APPENDIX A
UWO PRESSURE TAP LAYOUT AND TESTING PARAMETERS

This appendix contains pertinent information related to pressure tests conducted at the University of Western (UWO) on a 1:100 model of the WERFL experimental building. This study was part of a cooperative agreement between the National Institute of Standards and Technology (NIST) and Texas Tech University.

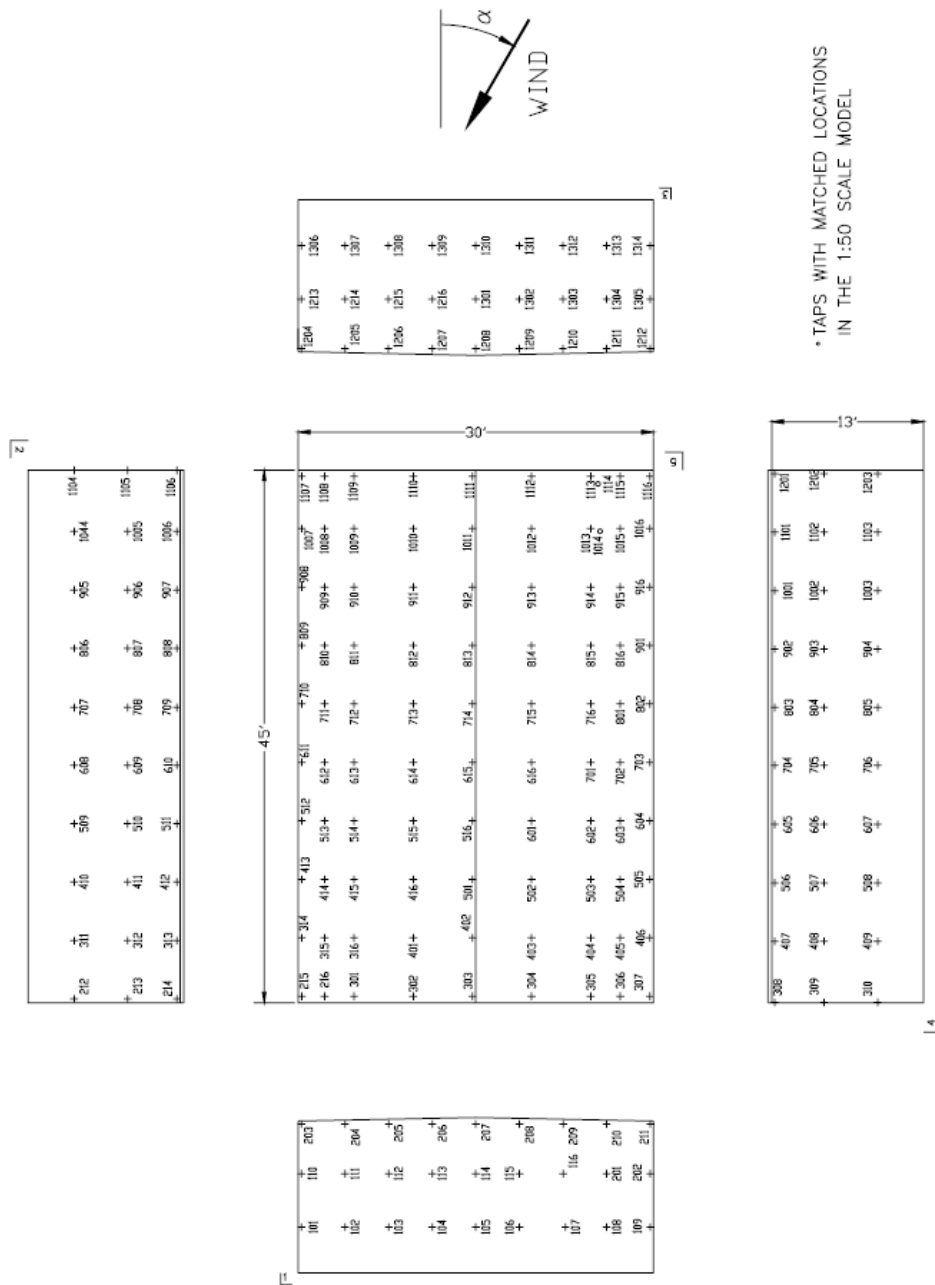


Figure A-1. UWO pressure tap layout for 1:100 WERFL model (Source: Ho et al., 2003).

SUMMARY DATA SHEET

TEST 7 – WERFL BUILDING – UWO 1:100 MODEL (45'x30'x13', ¼:12 ROOF SLOPE)

Building dimensions	45' x 30' x 13'; ¼:12 roof slope gable roof	
Model scale	1:100	
Number of pressure taps	206 external taps	
Sampling frequency	500 Hz	
Sampling period	100 seconds	
Reference wind tunnel speed	45 fps, nominal (see note 1)	
Test angles	22 angles – 0°, 10°, 15°, 20°, 25°, 30°, 35°, 40°, 45°, 50°, 55°, 60°, 65°, 70°, 75°, 80°, 90°, 135°, 180°, 225°, 270°, 315°	
Upstream exposure	1	2
Exposure description	WERFL site condition (10 th percentile)	WERFL site condition (90 th percentile)
Roughness length (m)	0.01	0.087
Ratio of roof to reference wind speed (see note 2)	0.658	0.500
Nominal roof height wind speed, V_{Hm} , in fps (see notes 1 and 2)	30	23
Full scale mean wind speed at roof height (fps)	V_H	
Equivalent full scale sampling frequency	$\frac{5 V_H}{V_{Hm}}$	
Equivalent full scale sampling duration (seconds)	$\frac{10000 V_{Hm}}{V_H}$	
Test file identifications:		
Basic tests	ST3___	ST4___
Additional tests: 20 repeat tests at 45° wind angle	STR___	

Notes:

1. Actual wind speeds are within 5% of 45 fps at reference level. Pressure coefficients have been normalized based on actual wind tunnel speeds. For the determination of time scaling, nominal wind speed of 45 fps has been used.
2. Best estimates of ratios of roof height to reference wind speeds.

Figure A-2. UWO test parameters for 1:100 WERFL model (Source: Ho et al., 2003).

APPENDIX B UFL WERFL MODELS

This appendix includes illustrative images of experimental configurations for pressure tests of a 1:20 model of the WERFL experimental building. The experiments were conducted at the University of Florida's boundary layer wind tunnel (BLWT).

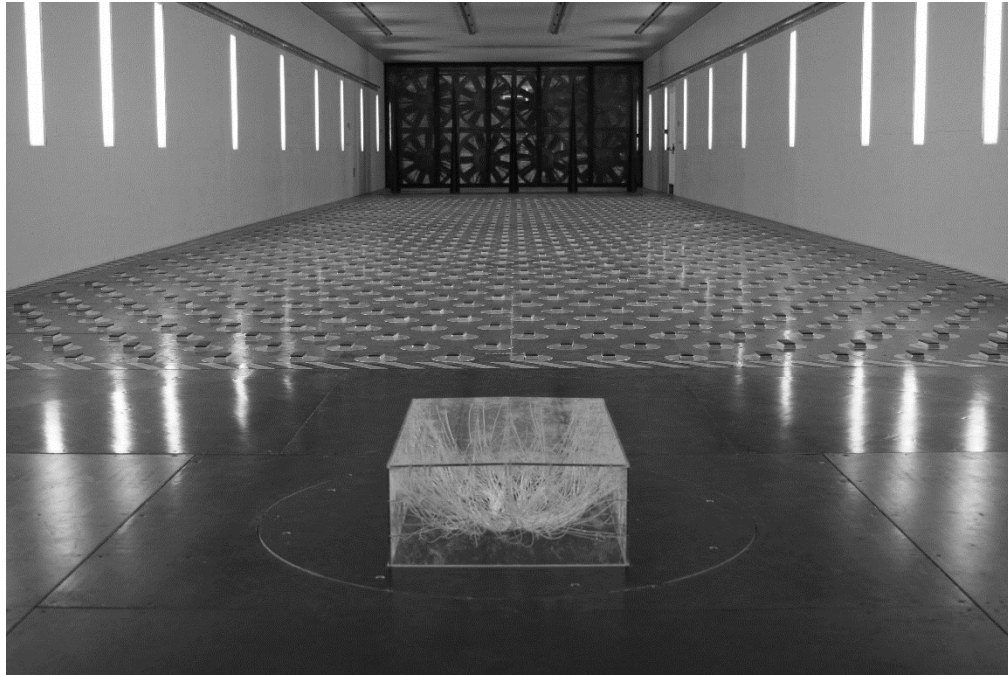


Figure B-1. 1:20 UFL-WERFL model (Narrow edge, $h = 20$ mm, $\alpha = 0^\circ$) (Photo courtesy of author).

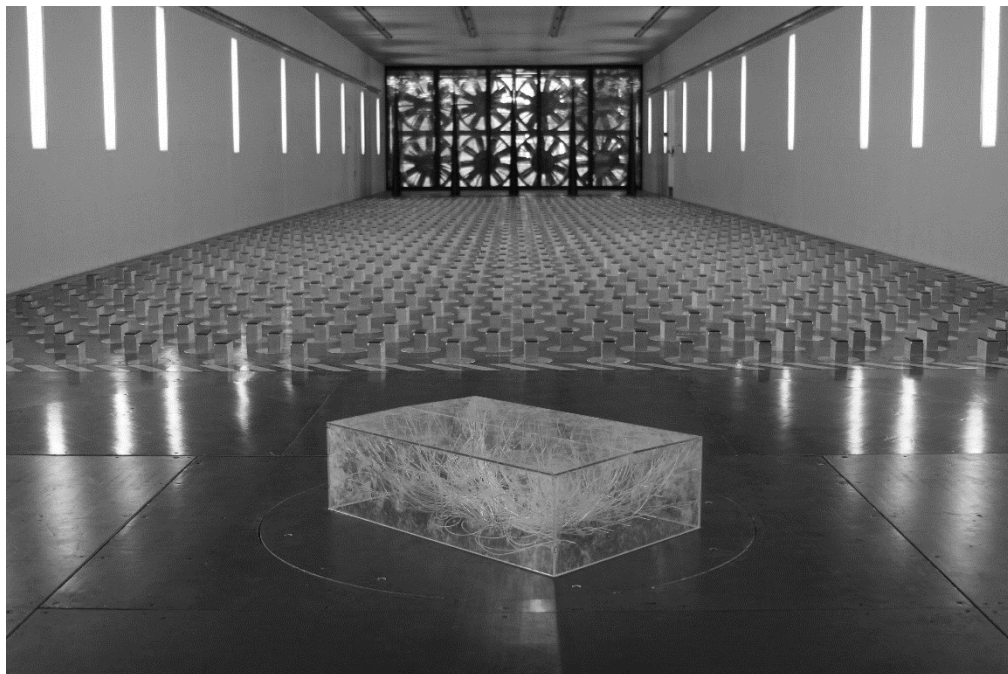


Figure B-2. 1:20 UFL-WERFL model (Narrow edge, $h = 80$ mm, $\alpha = 45^\circ$) (Photo courtesy of author).



Figure B-3. 1:20 UFL-WERFL model (Narrow edge, $h = 160$ mm, $\alpha = 90^\circ$) (Photo courtesy of author).

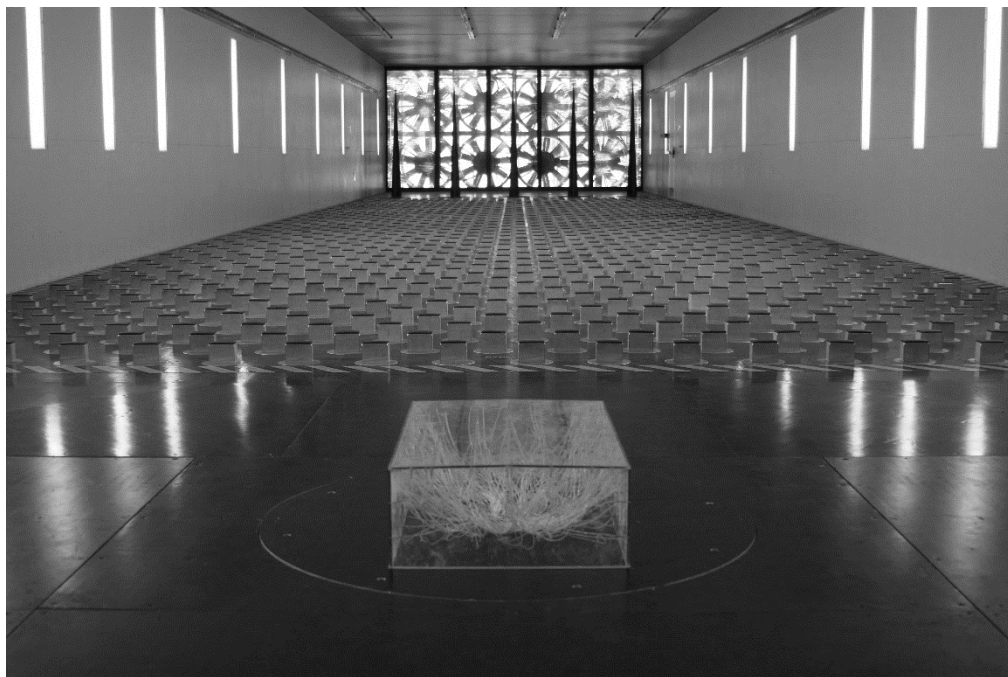


Figure B-4. 1:20 UFL-WERFL model (Wide edge, $h = 80$ mm, $\alpha = 0^\circ$) (Photo courtesy of author).

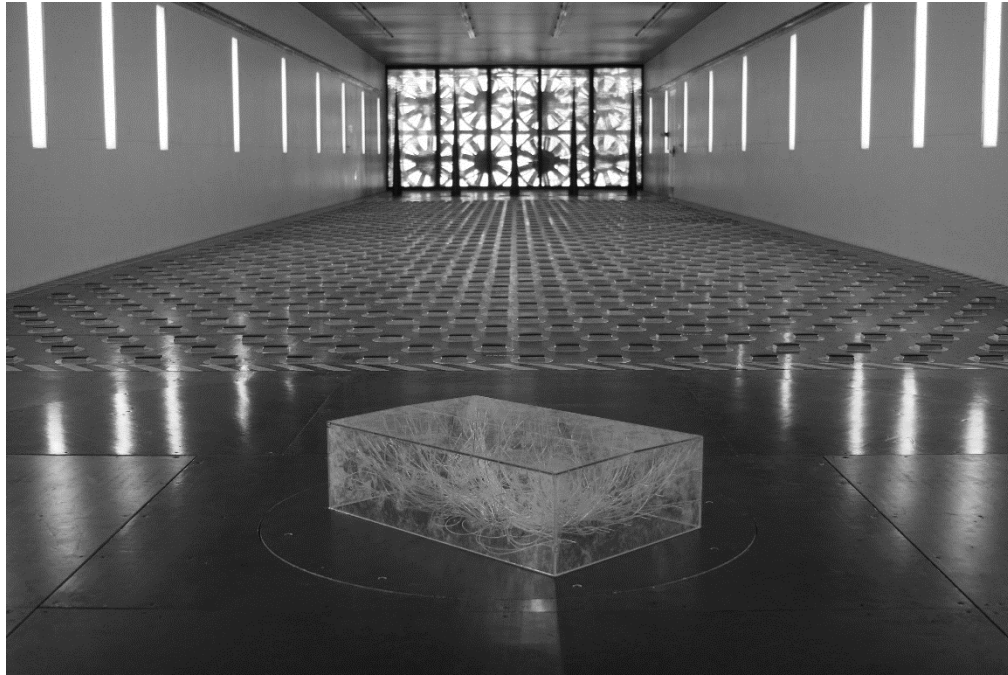


Figure B-5. 1:20 UFL-WERFL model (Wide edge, $h = 20$ mm, $\alpha = 45^\circ$) (Photo courtesy of author).



Figure B-6. 1:20 UFL-WERFL model (Wide edge, $h = 160$ mm, $\alpha = 90^\circ$) (Photo courtesy of author).

APPENDIX C GEOMETRY OF WERFL MODELS (UFL)

Vertices and pressure tap coordinates for the 1:20 WERFL model are tabulated in this appendix. Physical coordinates for the 1:30 and 1:50 models can be obtained by applying scaling factors to tabulated values. The scaling factors for the 1:30 and 1:50 are 0.67 and 0.4, respectively.

Table C-1. WERFL model tap coordinates (1:20)

Tap Index	Tap ID	X (mm)	Y (mm)	Z (mm)	Surface
1	101	3.8	0.0	52.9	1
2	102	60.0	0.0	59.1	1
3	103	148.0	0.0	59.1	1
4	104	172.4	0.0	59.1	1
5	105	235.0	0.0	59.1	1
6	106	284.8	0.0	59.1	1
7	107	300.4	0.0	59.1	1
8	108	397.2	0.0	59.1	1
9	109	453.4	0.0	52.9	1
10	110	3.8	0.0	120.7	1
11	111	60.0	0.0	126.9	1
12	112	148.0	0.0	126.9	1
13	113	172.4	0.0	126.9	1
14	114	235.0	0.0	126.9	1
15	115	284.8	0.0	126.9	1
16	116	300.4	0.0	126.9	1
17	201	397.2	0.0	126.9	1
18	202	453.4	0.0	120.7	1
19	203	3.8	0.0	191.7	1
20	204	60.0	0.0	198.0	1
21	205	148.0	0.0	198.0	1
22	206	172.4	0.0	198.0	1
23	207	235.0	0.0	198.0	1
24	208	284.8	0.0	198.0	1
25	209	300.4	0.0	198.0	1
26	210	397.2	0.0	198.0	1
27	211	453.4	0.0	191.7	1
28	212	0.0	4.7	59.1	2
29	213	0.0	4.7	128.0	2
30	214	0.0	4.7	192.6	2
31	215	4.4	8.2	198.2	6
32	216	33.7	8.2	198.8	6
33	301	71.8	8.2	199.6	6
34	302	148.0	8.2	201.2	6
35	303	224.2	8.2	202.8	6
36	304	300.4	8.2	201.4	5
37	305	376.6	8.2	199.8	5
38	306	414.7	8.2	199.0	5
39	307	452.8	8.2	198.2	5
40	308	457.2	5.0	192.6	4

Table C-1. Continued

Tap Index	Tap ID	X (mm)	Y (mm)	Z (mm)	Surface
41	309	457.2	3.2	128.0	4
42	310	457.2	3.2	59.1	4
43	311	0.0	80.0	59.1	2
44	312	0.0	80.0	128.0	2
45	313	0.0	88.2	192.6	2
46	314	4.4	83.5	198.2	6
47	315	33.7	83.5	198.8	6
48	316	71.8	83.5	199.6	6
49	401	148.0	83.5	201.2	6
50	402	224.2	83.5	202.8	6
51	403	300.4	83.5	201.4	5
52	404	376.6	83.5	199.8	5
53	405	414.7	83.5	199.0	5
54	406	452.8	83.5	198.2	5
55	407	457.2	91.4	192.6	4
56	408	457.2	79.1	128.0	4
57	409	457.2	79.1	59.1	4
58	410	0.0	155.3	59.1	2
59	411	0.0	155.3	128.0	2
60	412	0.0	162.5	192.6	2
61	413	4.4	158.8	198.2	6
62	414	33.7	158.8	198.8	6
63	415	71.8	158.8	199.6	6
64	416	148.0	158.8	201.2	6
65	501	224.2	158.8	202.8	6
66	502	300.4	158.8	201.4	5
67	503	376.6	158.8	199.8	5
68	504	414.7	158.8	199.0	5
69	505	452.8	158.8	198.2	5
70	506	457.2	165.8	192.6	4
71	507	457.2	154.2	128.0	4
72	508	457.2	154.2	59.1	4
73	509	0.0	234.1	59.1	2
74	510	0.0	234.1	128.0	2
75	511	0.0	234.1	192.6	2
76	512	4.4	234.1	198.2	6
77	513	33.7	234.1	198.8	6
78	514	71.8	234.1	199.6	6
79	515	148.0	234.1	201.2	6
80	516	224.2	234.1	202.8	6

Table C-1. Continued

Tap Index	Tap ID	X (mm)	Y (mm)	Z (mm)	Surface
81	601	300.4	234.1	201.4	5
82	602	376.6	234.1	199.8	5
83	603	414.7	234.1	199.0	5
84	604	452.8	234.1	198.2	5
85	605	457.2	234.1	192.6	4
86	606	457.2	234.1	128.0	4
87	607	457.2	234.1	59.1	4
88	608	0.0	305.7	59.1	2
89	609	0.0	305.7	128.0	2
90	610	0.0	312.9	192.6	2
91	611	4.4	309.4	198.2	6
92	612	33.7	309.4	198.8	6
93	613	71.8	309.4	199.6	6
94	614	148.0	309.4	201.2	6
95	615	224.2	309.4	202.8	6
96	616	300.4	309.4	201.4	5
97	701	376.6	309.4	199.8	5
98	702	414.7	309.4	199.0	5
99	703	452.8	309.4	198.2	5
100	704	457.2	317.1	192.6	4
101	705	457.2	305.7	128.0	4
102	706	457.2	305.7	59.1	4
103	707	0.0	380.1	59.1	2
104	708	0.0	380.1	128.0	2
105	709	0.0	368.7	192.6	2
106	710	4.4	384.7	198.2	6
107	711	33.7	384.7	198.8	6
108	712	71.8	384.7	199.6	6
109	713	148.0	384.7	201.2	6
110	714	224.2	384.7	202.8	6
111	715	300.4	384.7	201.4	5
112	716	376.6	384.7	199.8	5
113	801	414.7	384.7	199.0	5
114	802	452.8	384.7	198.2	5
115	803	457.2	372.9	192.6	4
116	804	457.2	380.1	128.0	4
117	805	457.2	380.1	59.1	4
118	806	0.0	459.9	59.1	2
119	807	0.0	459.9	128.0	2
120	808	0.0	459.9	192.6	2

Table C-1. Continued

Tap Index	Tap ID	X (mm)	Y (mm)	Z (mm)	Surface
121	809	4.4	459.9	198.2	6
122	810	33.7	459.9	198.8	6
123	811	71.8	459.9	199.6	6
124	812	148.0	459.9	201.2	6
125	813	224.2	459.9	202.8	6
126	814	300.4	459.9	201.4	5
127	815	376.6	459.9	199.8	5
128	816	414.7	459.9	199.0	5
129	901	452.8	459.9	198.2	5
130	902	457.2	459.9	192.6	4
131	903	457.2	459.9	128.0	4
132	904	457.2	459.9	59.1	4
133	905	0.0	531.6	59.1	2
134	906	0.0	531.6	128.0	2
135	907	0.0	520.0	192.6	2
136	908	4.4	535.2	198.2	6
137	909	33.7	535.2	198.8	6
138	910	71.8	535.2	199.6	6
139	911	148.0	535.2	201.2	6
140	912	224.2	535.2	202.8	6
141	913	300.4	535.2	201.4	5
142	914	376.6	535.2	199.8	5
143	915	414.7	535.2	199.0	5
144	916	452.8	535.2	198.2	5
145	1001	457.2	523.3	192.6	4
146	1002	457.2	530.5	128.0	4
147	1003	457.2	530.5	59.1	4
148	1004	0.0	606.7	59.1	2
149	1005	0.0	606.7	128.0	2
150	1006	0.0	594.4	192.6	2
151	1007	4.4	610.5	198.2	6
152	1008	33.7	610.5	198.8	6
153	1009	71.8	610.5	199.6	6
154	1010	148.0	610.5	201.2	6
155	1011	224.2	610.5	202.8	6
156	1012	300.4	610.5	201.4	5
157	1013	376.6	610.5	199.8	5
158	1014	388.6	614.0	199.5	5
159	1015	414.7	610.5	199.0	5
160	1016	452.8	610.5	198.2	5

Table C-1. Continued

Tap Index	Tap ID	X (mm)	Y (mm)	Z (mm)	Surface
161	1101	457.2	597.6	192.6	4
162	1102	457.2	605.8	128.0	4
163	1103	457.2	605.8	59.1	4
164	1104	0.0	682.6	59.1	2
165	1105	0.0	682.6	128.0	2
166	1106	0.0	680.8	192.6	2
167	1107	4.4	677.6	198.2	6
168	1108	33.7	677.6	198.8	6
169	1109	71.8	677.6	199.6	6
170	1110	148.0	677.6	201.2	6
171	1111	224.2	677.6	202.8	6
172	1112	300.4	677.6	201.4	5
173	1113	376.6	681.1	199.8	5
174	1114	386.0	671.5	199.6	5
175	1115	414.7	677.6	199.0	5
176	1116	452.8	677.6	198.2	5
177	1201	457.2	681.1	192.6	4
178	1202	457.2	681.1	128.0	4
179	1203	457.2	681.1	59.1	4
180	1204	3.8	685.8	52.9	3
181	1205	60.0	685.8	52.9	3
182	1206	148.0	685.8	52.9	3
183	1207	172.4	685.8	52.9	3
184	1208	235.0	685.8	52.9	3
185	1209	284.8	685.8	52.9	3
186	1210	300.4	685.8	52.9	3
187	1211	397.2	685.8	52.9	3
188	1212	453.4	685.8	52.9	3
189	1213	3.8	685.8	120.7	3
190	1214	60.0	685.8	120.7	3
191	1215	148.0	685.8	120.7	3
192	1216	172.4	685.8	120.7	3
193	1301	235.0	685.8	120.7	3
194	1302	284.8	685.8	120.7	3
195	1303	300.4	685.8	120.7	3
196	1304	397.2	685.8	120.7	3
197	1305	453.4	685.8	120.7	3
198	1306	3.8	685.8	191.7	3
199	1307	60.0	685.8	191.7	3
200	1308	148.0	685.8	191.7	3

Table C-1. Continued

Tap Index	Tap ID	X (mm)	Y (mm)	Z (mm)	Surface
201	1309	172.4	685.8	191.7	3
202	1310	235.0	685.8	191.7	3
203	1311	284.8	685.8	191.7	3
204	1312	300.4	685.8	191.7	3
205	1313	397.2	685.8	191.7	3
206	1314	453.4	685.8	191.7	3
207	1315	233.0	8.2	202.8	5
208	1316	233.0	83.5	202.8	5
209	1317	233.0	158.8	202.8	5
210	1318	233.0	234.1	202.8	5
211	1319	233.0	309.4	202.8	5
212	1320	233.0	384.7	202.8	5
213	1321	233.0	459.9	202.8	5
214	1322	233.0	535.2	202.8	5
215	1323	233.0	610.5	202.8	5
216	1324	233.0	677.6	202.8	5
217	1325	148.0	45.9	201.2	6
218	1326	148.0	121.2	201.2	6
219	1327	148.0	196.4	201.2	6
220	1328	148.0	271.7	201.2	6
221	1329	148.0	347.0	201.2	6
222	1330	148.0	422.3	201.2	6
223	1331	148.0	497.6	201.2	6
224	1332	148.0	572.9	201.2	6
225	1333	148.0	644.0	201.2	6
226	1334	300.4	45.9	201.4	5
227	1335	300.4	121.2	201.4	5
228	1336	300.4	196.4	201.4	5
229	1337	300.4	271.7	201.4	5
230	1338	300.4	347.0	201.4	5
231	1339	300.4	422.3	201.4	5
232	1340	300.4	497.6	201.4	5
233	1341	300.4	572.9	201.4	5
234	1342	300.4	644.0	201.4	5
235	1343	19.1	234.1	198.5	6
236	1344	52.7	234.1	199.2	6
237	1345	109.9	234.1	200.4	6
238	1346	186.1	234.1	202.0	6
239	1347	266.7	234.1	202.1	5
240	1348	338.5	234.1	200.6	5

Table C-1. Continued

Tap Index	Tap ID	X (mm)	Y (mm)	Z (mm)	Surface
241	1349	395.6	234.1	199.4	5
242	1350	433.7	234.1	198.6	5
243	1351	266.7	459.9	202.1	5
244	1352	338.5	459.9	200.6	5
245	1353	395.6	459.9	199.4	5
246	1354	433.7	459.9	198.6	5
247	1355	19.1	459.9	198.5	6
248	1356	52.7	459.9	199.2	6
249	1357	109.9	459.9	200.4	6
250	1358	186.1	459.9	202.0	6
251	1359	4.4	45.9	198.2	6
252	1360	33.7	45.9	198.8	6
253	1361	71.8	45.9	199.6	6
254	1362	224.2	45.9	202.8	6
255	1363	233.0	45.9	202.8	5
256	1365	376.6	45.9	199.8	5
257	1366	414.7	45.9	199.0	5
258	1367	452.8	45.9	198.2	5
259	1368	4.4	644.0	198.2	6
260	1369	33.7	644.0	198.8	6
261	1370	71.8	644.0	199.6	6
262	1371	224.2	644.0	202.8	6
263	1372	233.0	644.0	202.8	5
264	1373	376.6	645.8	199.8	5
265	1374	414.7	644.0	199.0	5
266	1375	452.8	644.0	198.2	5

Table C-2. Vertices of WERFL building model (1:20)

Surface	X (mm)	Y (mm)	Z (mm)	Building Feature
	0.0	0.0	0.0	
	457.2	0.0	0.0	
1	457.2	0.0	198.1	Wall
	228.6	0.0	202.9	
	0.0	0.0	198.1	
	0.0	0.0	0.0	
2	0.0	0.0	198.1	Wall
	0.0	685.8	198.1	
	0.0	685.8	0.0	
	0.0	685.8	198.1	
3	228.6	685.8	202.9	Wall
	457.2	685.8	198.1	
	457.2	685.8	0.0	
	0.0	685.8	0.0	
	0.0	685.8	198.1	
4	228.6	685.8	202.9	Wall
	457.2	685.8	198.1	
	457.2	685.8	0.0	
	0.0	685.8	0.0	
	228.6	685.8	202.9	
5	457.2	685.8	198.1	Roof
	457.2	0.0	198.1	
	228.6	0.0	202.9	
	0.0	685.8	198.1	
6	228.6	685.8	202.9	Roof
	228.6	0.0	202.9	
	0.0	0.0	198.1	

LIST OF REFERENCES

- ASCE 7-10 (2010). Minimum Design Loads for Buildings and Other Structures, American Society of Civil Engineers, Reston, VA.
- ACI Committee, American Concrete Institute, & International Organization for Standardization. (2008). Building code requirements for structural concrete (ACI 318-08) and commentary. American Concrete Institute.
- Akon, A. F., & Kopp, G. A. (2016). Mean pressure distributions and reattachment lengths for roof-separation bubbles on low-rise buildings. *Journal of Wind Engineering and Industrial Aerodynamics*, 155, 115-125.
- Antonia, R. A., & Atkinson, J.D. (1973). High-order moments of Reynolds shear stress fluctuations in a turbulent boundary layer. *Journal of Fluid Mechanics*, 58(03), 581-593.
- Arora, J. (2004). Introduction to optimum design. Academic Press.
- Arora, J. S. (2000). Methods for discrete variable structural optimization. In *Advanced Technology in Structural Engineering* (pp. 1-8).
- Azad, S. K., & Hasançebi, O. (2015). Computationally efficient discrete sizing of steel frames via guided stochastic search heuristic. *Computers & Structures*, 156, 12-28.
- Balderrama, J. A., Masters, F. J., Gurley, K. R., Prevatt, D.O., Aponte-Bermúdez, L. D., Reinhold, T. A., et al. (2011). The Florida Coastal Monitoring Program (FCMP): A Review. *Journal of Wind Engineering and Industrial Aerodynamics*, 99(9), 979-995.
- Balderrama, J. A., Masters, F. J., & Gurley, K. R. (2012). Peak factor estimation in hurricane surface winds. *Journal of Wind Engineering and Industrial Aerodynamics*, 102, 1-13.
- Baldocchi, D. D., & Hutchison, B. A. (1987). Turbulence in an almond orchard: vertical variations in turbulent statistics. *Boundary-Layer Meteorology*, 40(1-2), 127-146.
- Baldocchi, D. D., & Meyers, T. P. (1988). Turbulence structure in a deciduous forest. *Boundary-Layer Meteorology*, 43(4), 345-364.
- Bendat, J. S., & Piersol, A. G. (2000). Random data analysis and measurement procedures.
- Blocken, B. (2014). 50 years of computational wind engineering: past, present and future. *Journal of Wind Engineering and Industrial Aerodynamics*, 129, 69-102.

- Böhm, M., Finnigan, J. J., Raupach, M. R., & Hughes, D. (2013). Turbulence structure within and above a canopy of bluff elements. *Boundary-layer meteorology*, 1-27.
- Camp, C. V., Bichon, B. J., & Stovall, S. P. (2005). Design of steel frames using ant colony optimization. *Journal of Structural Engineering*, 131(3), 369-379.
- Camp, C. V. (2007). Design of space trusses using Big Bang–Big Crunch optimization. *Journal of Structural Engineering*, 133(7), 999-1008.
- Chan, C. M., & Grierson, D. E. (1993). An efficient resizing technique for the design of tall steel buildings subject to multiple drift constraints. *The Structural Design of Tall and Special Buildings*, 2(1), 17-32.
- Chan, C. M., Grierson, D. E., & Sherbourne, A. N. (1995). Automatic optimal design of tall steel building frameworks. *Journal of Structural Engineering*, 121(5), 838-847.
- Chan, C. M., Huang, M. F., & Kwok, K. C. S. (2010). Integrated wind load analysis and stiffness optimization of tall buildings with 3D modes. *Engineering structures*, 32(5), 1252-1261.
- Chen, F. (1990). Turbulent characteristics over a rough natural surface part I: turbulent structures. *Boundary-Layer Meteorology*, 52(1-2), 151-175.
- Counehan, J. (1971). Wind tunnel determination of the roughness length as a function of the fetch and the roughness density of three-dimensional roughness elements. *Atmospheric Environment (1967)*, 5(8), 637-642.
- Cuevas, E., Echavarría, A., & Ramírez-Ortegón, M. A. (2014). An optimization algorithm inspired by the States of Matter that improves the balance between exploration and exploitation. *Applied intelligence*, 40(2), 256-272.
- Davenport, A. G. (1964, June). Note on the distribution of the largest value of a random function with application to gust loading. In *ICE Proceedings (Vol. 28, No. 2, pp. 187-196)*. Thomas Telford.
- Davenport, A. G. (1977). *Wind Loads on Low Rise Buildings: Final Report of Phases I and II. Part I: Text and Figures*.
- Davenport, A. G. (2007). *Wind tunnel testing: a general outline*. The University of Western Ontario, Faculty of Engineering Science London, Ontario, Canada.
- Eberhart, R. C., & Kennedy, J. (1995, October). A new optimizer using particle swarm theory. In *Proceedings of the sixth international symposium on micro machine and human science (Vol. 1, pp. 39-43)*.
- Erol, O. K., & Eksin, I. (2006). A new optimization method: big bang–big crunch. *Advances in Engineering Software*, 37(2), 106-111.

- ESDU (1974). Characteristics of atmospheric turbulence near the ground. Part I: definitions and general information, Engineering Sciences Data Unit, Itm. No. 74030, 74031, London, UK.
- ESDU (1983). Strong winds in the atmospheric boundary layer, Part 2: Discrete gust speeds, Engineering Sciences Data Unit, Itm. No. 83045, London, UK.
- Fenton, R. G. (1974). A comparison of numerical optimization methods for engineering design. *CONSTRAINTS*, 5(5), 5.
- Feury, C., & Geradin, M. (1978). Optimality criteria and mathematical programming in structural weight optimization. *Computers & Structures*, 8(1), 7-17.
- Finnigan, J. (2000). Turbulence in plant canopies. *Annual review of fluid mechanics*, 32(1), 519-571.
- Foken, T., & Nappo, C. J. (2008). *Micrometeorology*. Springer Science & Business Media.
- Gartshore, I. S. (1984). Some effects of upstream turbulence on the unsteady lift forces imposed on prismatic two dimensional bodies. *J. Fluids Eng*, 106(4), 418-424.
- Haftka, R. T. (1985). Simultaneous analysis and design. *AIAA journal*, 23(7), 1099-1103.
- Haftka, R. T., & Gürdal, Z. (2012). *Elements of structural optimization (Vol. 11)*. Springer Science & Business Media.
- Harris, R. I., & Deaves, D. M. (1980, November). The structure of strong winds. In *Proceedings of the CIRIA conference held on* (pp. 12-13).
- Hasançebi, O., Bahçecioğlu, T., Kurç, Ö., & Saka, M. P. (2011). Optimum design of high-rise steel buildings using an evolution strategy integrated parallel algorithm. *Computers & Structures*, 89(21), 2037-2051.
- Hillier, R., & Cherry, N. J. (1981). The effects of stream turbulence on separation bubbles. *Journal of wind engineering and industrial aerodynamics*, 8(1-2), 49-58.
- Ho, T. C. E., Surry, D., & Morrish, D. P. (2003). *NIST/TTU cooperative agreement—windstorm mitigation initiative: Wind tunnel experiments on generic low buildings*. The Boundary Layer Wind Tunnel Laboratory, The University of Western Ontario, London, Ontario, Canada.
- Holmes, J. D. (1981). Non-Gaussian characteristics of wind pressure fluctuations. *Journal of Wind Engineering and Industrial Aerodynamics*, 7(1), 103-108.
- Holmes, J. D. (1983). *Wind loads on low-rise buildings: A review*. Commonwealth Scientific and Industrial Research Organization, Division of Building Research.

- Holmes, J. D., & Cochran, L. S. (2003). Probability distributions of extreme pressure coefficients. *Journal of Wind Engineering and Industrial Aerodynamics*, 91(7), 893-901.
- Huang, M. F., Chan, C. M., & Lou, W. J. (2012). Optimal performance-based design of wind sensitive tall buildings considering uncertainties. *Computers & Structures*, 98, 7-16.
- Hunt, A. (1982). Wind-tunnel measurements of surface pressures on cubic building models at several scales. *Journal of Wind Engineering and Industrial Aerodynamics*, 10(2), 137-163.
- Haftka, R. T., & Gürdal, Z. (2012). *Elements of structural optimization (Vol. 11)*. Springer Science & Business Media.
- Irwin, P. A. (2006). Exposure categories and transitions for design wind loads. *Journal of Structural Engineering*, 132(11), 1755-1763.
- Jackson, P. S. (1981). On the displacement height in the logarithmic velocity profile. *Journal of Fluid Mechanics*, 111, 15-25.
- Jensen, M. (1958). The model-law for phenomena in natural wind. *Ingenioren*, 2(4), 121-128.
- Jensen, M., & Franck, N. (1963). *Model-scale tests in turbulent wind*. Danish Technical Press.
- Kareem, A., & Zhao, J. (1994). Analysis of non-Gaussian surge response of tension leg platforms under wind loads. *Journal of Offshore Mechanics and Arctic Engineering*, 116(3), 137-144.
- Karimpour, A., Kaye, N. B., & Baratian-Ghorghi, Z. (2012). Modeling the neutrally stable atmospheric boundary layer for laboratory scale studies of the built environment. *Building and Environment*, 49, 203-211.
- Kaveh, A., & Talatahari, S. (2009). Particle swarm optimizer, ant colony strategy and harmony search scheme hybridized for optimization of truss structures. *Computers & Structures*, 87(5), 267-283.
- Kaveh, A., & Talatahari, S. (2010). A discrete big bang-big crunch algorithm for optimal design of skeletal structures. *Asian Journal of Civil Engineering*, 11(1), 103-122.
- Kaveh, A., & Abbasgholiha, H. (2011). Optimum design of steel sway frames using Big Bang-Big Crunch algorithm. *Asian J Civ Eng*, 12(3), 293-317.
- Kicinger, R., Arciszewski, T., & DeJong, K. (2005). Evolutionary design of steel structures in tall buildings. *Journal of Computing in Civil Engineering*, 19(3), 223-238.

- Khan, M. R. (1984). Optimality criterion techniques applied to frames having general cross-sectional relationships. *AIAA journal*, 22(5), 669-676.
- Krishna, P. (1995). Wind loads on low-rise buildings—A review. *Journal of wind engineering and industrial aerodynamics*, 54, 383-396.
- Lettau, H. (1969). Note on aerodynamic roughness-parameter estimation on the basis of roughness-element description. *Journal of applied meteorology*, 8(5), 828-832.
- Li, L. J., Huang, Z. B., & Liu, F. (2009). A heuristic particle swarm optimization method for truss structures with discrete variables. *Computers & Structures*, 87(7), 435-443.
- Lieblein, J. (1974). Efficient Methods of Extreme-Value Methodology. Technical Report NBSIR 74-602, National Bureau of Standards, Washington, D.C.
- Lin, J. X., Surry, D., & Tieleman, H. W. (1995). The distribution of pressure near roof corners of flat roof low buildings. *Journal of wind engineering and industrial aerodynamics*, 56(2-3), 235-265.
- LRFD, A. (2010). Manual of steel construction, load and resistance factor design. Chicago: American Institute of Steel Construction.
- Lu, S. S., & Willmarth, W. W. (1973). Measurements of the structure of the Reynolds stress in a turbulent boundary layer. *Journal of Fluid Mechanics*, 60(03), 481-511.
- Macdonald, R. W., Griffiths, R. F., & Hall, D. J. (1998). An improved method for the estimation of surface roughness of obstacle arrays. *Atmospheric environment*, 32(11), 1857-1864.
- Maitani, T., & Shaw, R. H. (1990). Joint probability analysis of momentum and heat fluxes at a deciduous forest. *Boundary-Layer Meteorology*, 52(3), 283-300.
- Marshall, R. D. (1975). A study of wind pressures on a single-family dwelling in model and full scale. *Journal of Wind Engineering and Industrial Aerodynamics*, 1, 177-199.
- Meecham, D., Surry, D., & Davenport, A. G. (1991). The magnitude and distribution of wind-induced pressures on hip and gable roofs. *Journal of Wind Engineering and Industrial Aerodynamics*, 38(2-3), 257-272.
- Mirjalili, S., Mirjalili, S. M., & Lewis, A. (2014). Grey wolf optimizer. *Advances in Engineering Software*, 69, 46-61.
- Nakagawa, H., & Nezu, I. (1977). Prediction of the contributions to the Reynolds stress from bursting events in open-channel flows. *Journal of fluid mechanics*, 80(01), 99-128.

- NRCC (National Research Council Canada, 1995), National Building Code of Canada 1995 (NBCC (1995)); Includes User's Guide—NBC 1995 Structural Commentaries (Part 4), NRCC, Ottawa, Canada.
- Oikawa, S., & Meng, Y. (1995). Turbulence characteristics and organized motion in a suburban roughness sublayer. *Boundary-Layer Meteorology*, 74(3), 289-312.
- Perez, R. E., & Behdinan, K. (2007). Particle swarm approach for structural design optimization. *Computers & Structures*, 85(19), 1579-1588.
- Pierre, L. S., Kopp, G. A., Surry, D., & Ho, T. C. E. (2005). The UWO contribution to the NIST aerodynamic database for wind loads on low buildings: Part 2. Comparison of data with wind load provisions. *Journal of Wind Engineering and Industrial Aerodynamics*, 93(1), 31-59.
- Raupach, M. R. (1981). Conditional statistics of Reynolds stress in rough-wall and smooth-wall turbulent boundary layers. *Journal of Fluid Mechanics*, 108, 363-382.
- Raupach, M., Finnigan, J. J., & Brunei, Y. (1996). Coherent eddies and turbulence in vegetation canopies: the mixing-layer analogy. *Boundary-Layer Meteorology*, 78(3-4), 351-382.
- Rotach, M. W. (1993). Turbulence close to a rough urban surface part I: Reynolds stress. *Boundary-Layer Meteorology*, 65(1-2), 1-28.
- Rotach, M. W. (1999). On the influence of the urban roughness sublayer on turbulence and dispersion. *Atmospheric Environment*, 33(24), 4001-4008.
- Rotach, M. W., Vogt, R., Bernhofer, C., Batchvarova, E., Christen, A., Clappier, A., ... & Mitev, V. (2005). BUBBLE—an urban boundary layer meteorology project. *Theoretical and Applied Climatology*, 81(3-4), 231-261.
- Safari, D., Maheri, M. R., & Maheri, A. (2013). On the performance of a modified multiple-deme genetic algorithm in LRFD design of steel frames. *Iranian Journal of Science and Technology. Transactions of Civil Engineering*, 37(C2), 169.
- Saka, M. P. (1984). Optimum design of space trusses with buckling constraints. In *Third International Conference on Space Structures*, Elsevier Applied Science Publ., London (pp. 656-660).
- Shaw, R. H., Tavangar, J., & Ward, D. P. (1983). Structure of the Reynolds stress in a canopy layer. *Journal of Climate and Applied Meteorology*, 22(11), 1922-1931.
- Spence, S. M., & Giofrè, M. (2012). Large scale reliability-based design optimization of wind excited tall buildings. *Probabilistic Engineering Mechanics*, 28, 206-215.

- Spence, S. M., & Kareem, A. (2013). Data-enabled design and optimization (DEDOpt): tall steel building frameworks. *Computers & Structures*, 129, 134-147.
- Stathopoulos, T (1979). Turbulent wind action on low-rise buildings, Ph.D. Thesis, The University of Western Ontario, London, Ontario, Canada.
- Stathopoulos, T. (1980). PDF of wind pressures on low-rise buildings. *Journal of the structural Division*, 106(5), 973-990.
- Stathopoulos, T., & Surry, D. (1983). Scale effects in wind tunnel testing of low buildings. *Journal of Wind Engineering and Industrial Aerodynamics*, 13(1-3), 313-326.
- Stathopoulos, T. (1984). Adverse wind loads on low buildings due to buffeting. *Journal of Structural Engineering*, 110(10), 2374-2392. doi:10.1061/(ASCE)0733-9445(1984)110:10(2374)
- Stathopoulos, T. (2003). Wind loads on low buildings: in the wake of Alan Davenport's contributions. *Journal of wind engineering and industrial aerodynamics*, 91(12), 1565-1585.
- Tabak, E. I., & Wright, P. M. (1981). Optimality criteria method for building frames. *Journal of the Structural Division*, 107(7), 1327-1342.
- Tieleman, H. W., Reinhold, T. A., & Marshall, R. D. (1978). On the wind-tunnel simulation of the atmospheric surface layer for the study of wind loads on low-rise buildings. *Journal of Wind Engineering and Industrial Aerodynamics*, 3(1), 21-38.
- Tieleman, H. W. (1992). Problems associated with flow modelling procedures for low-rise structures. *Journal of Wind Engineering and Industrial Aerodynamics*, 42(1), 923-934.
- Tieleman, H. W., Surry, D., & Mehta, K. C. (1996). Full/model-scale comparison of surface pressures on the Texas Tech experimental building. *Journal of Wind Engineering and Industrial Aerodynamics*, 61(1), 1-23.
- Tieleman, H. W., Reinhold, T. A., & Hajj, M. R. (1997). Importance of turbulence for the prediction of surface pressures on low-rise structures. *Journal of wind engineering and industrial aerodynamics*, 69, 519-528.
- Toğan, V. (2012). Design of planar steel frames using teaching–learning based optimization. *Engineering Structures*, 34, 225-232.
- Troldborg, N., Sørensen, J. N., Mikkelsen, R., & Sørensen, N. N. (2014). A simple atmospheric boundary layer model applied to large eddy simulations of wind turbine wakes. *Wind Energy*, 17(4), 657-669.

- Uematsu, Y., & Isyumov, N. (1999). Wind pressures acting on low-rise buildings. AMSTERDAM: Elsevier Ltd. doi: 10.1016/S0167-6105(99)00036-7
- Vickery, P. J., & Skerlj, P. F. (2005). Hurricane gust factors revisited. *Journal of Structural Engineering*.
- Von Karman, T. (1948). Progress in the statistical theory of turbulence. *Proceedings of the National Academy of Sciences*, 34(11), 530-539.
- Walls, R., & Elvin, A. (2010). Optimizing structures subject to multiple deflection constraints and load cases using the principle of virtual work. *Journal of structural engineering*, 136(11), 1444-1452.
- Weber, R. O. (1999). Remarks on the definition and estimation of friction velocity. *Boundary-Layer Meteorology*, 93(2), 197-209.
- Yang, X., Yuan, J., Yuan, J., & Mao, H. (2007). A modified particle swarm optimizer with dynamic adaptation. *Applied Mathematics and Computation*, 189(2), 1205-1213.
- Wind tunnel testing for buildings and other structures (2012). Portland: Ringgold Inc.
- Walls, R., & Elvin, A. (2010). Optimizing structures subject to multiple deflection constraints and load cases using the principle of virtual work. *Journal of structural engineering*, 136(11), 1444-1452.
- Wheat, D. L., & Cramer, S. M. (2006). *Wood Design Package: National design specification for wood construction with commentary and supplement (Vol. 1)*. American Forest & Paper Association.
- Zhu, W., van Hout, R., & Katz, J. (2007). On the flow structure and turbulence during sweep and ejection events in a wind-tunnel model canopy. *Boundary-layer meteorology*, 124(2), 205-233.
- Zou, X. K., & Chan, C. M. (2005). An optimal resizing technique for seismic drift design of concrete buildings subjected to response spectrum and time history loadings. *Computers & Structures*, 83(19), 1689-1704.

BIOGRAPHICAL SKETCH

Pedro Luis Fernández Cabán was born in San Juan, Puerto Rico in 1987. He graduated with a Bachelor of Science in civil engineering from the University of Puerto Rico at Mayagüez in May 2013. During his time at Mayagüez, Fernández worked alongside Dr. Luis Aponte in the validation of local wind models. Fernández moved to Gainesville, Florida in the fall of 2013 to join Dr. Masters' research team and pursue a Ph.D. in civil engineering at the University of Florida. In May 2017, he received a Masters of Engineering in civil engineering (structural). Fernández secured a post-doctorate fellowship at the University of Maryland at College Park that will effectively combine the works presented in this dissertation to coordinate the first cyber-physical (CPS) modeling in a boundary layer wind tunnel.